GEORG-AUGUST-UNIVERSITÄT
GÖTTINGEN

Fakultät für
Physik

Master's Thesis

Messung des $Z \to \tau\tau$ Wirkungsquerschnitts im Lepton-Hadron Kanal für Proton-Proton Kollisionen am ATLAS Experiment

Measurement of the $Z \to \tau\tau$ cross section in the lepton-hadron channel in proton-proton collisions using the ATLAS detector

prepared by

Simon Schulte

from Hildesheim

at the II. Physikalischen Institut

Thesis number:	II.Physik-UniGö-MSc-2014/10
Thesis period:	26th May 2014 until 21st November 2014
First referee:	Prof. Dr. Arnulf Quadt
Second referee:	Prof. Dr. Ariane Frey

Abstract

In this thesis, the $Z \to \tau\tau$ cross section measurement of the lepton-hadron channel is presented. The results are based on the data set of an integrated luminosity of $\int \mathcal{L}\,\mathrm{d}t = 20.3\,\mathrm{fb}^{-1}$ recorded in a proton-proton collider at a center-of-mass energy of $\sqrt{s} = 8\,\mathrm{TeV}$ with the ATLAS detector at the LHC.

The differential cross sections in dependence of the lepton transverse momentum, the tau transverse momentum, the visible mass, and the invariant Z mass are calculated for the electron and muon channel respectively. Furthermore, a fiducial cross section and the total cross section are determined to allow a comparison to the theoretical expectations. The total inclusive $Z \to \tau\tau$ cross section with an invariant Z mass of $60\,\mathrm{GeV} < M < 2000\,\mathrm{GeV}$ is $1151.7 \pm 4.2\,(\mathrm{stat})\,^{+57.4}_{-50.9}\,(\mathrm{syst}) \pm 30.4\,(\mathrm{lumi})\,\mathrm{pb}$ for the muon-hadron channel and $1159.79 \pm 7.1\,(\mathrm{stat})\,^{+102.8}_{-98.9}\,(\mathrm{syst}) \pm 32.4\,(\mathrm{lumi})\,\mathrm{pb}$ for the electron-hadron channel and both are consistent with the theoretical calculations within their uncertainties.

Zusammenfassung

Im Rahmen dieser Masterarbeit werden die Ergebnisse der $Z \to \tau\tau$ Wirkungsquerschnittsmessungen des Lepton-Hadron Kanals präsentiert. Die verwendeten Daten der integrierten Luminosität von $\int \mathcal{L}\,\mathrm{d}t = 20.3\,\mathrm{fb}^{-1}$ wurden bei Proton-Proton Kollisionen bei einer Schwerpunktsenergie von $\sqrt{s} = 8\,\mathrm{TeV}$ mit dem ATLAS Detektor am LHC aufgenommen.

Es werden jeweils für den Elektron und Muon Kanal die differentiellen Wirkungsquerschnitte in Abhängigkeit des Lepton-Transversalimpuls, des Tau-Transversalimpuls, der sichtbaren Masse und der invarianten Z Masse berechnet. Darüberhinaus werden die integrierten Wirkungsquerschnitte der Signalregion und die totalen Wirkungsquerschnitte der inklusiven $Z \to \tau\tau$ Produktion in Abhängigkeit der beiden Kanäle bestimmt. Im Fall des Muon-Kanals ergibt sich $1151.7 \pm 4.2\,(\mathrm{stat})\,^{+57.4}_{-50.9}\,(\mathrm{syst}) \pm 30.4\,(\mathrm{lumi})\,\mathrm{pb}$ für den totalen Wirkungsquerschnitt von $Z \to \tau\tau$ bei einer invarianten Z Masse von $60\,\mathrm{GeV} < M < 2000\,\mathrm{GeV}$. Das Ergebnis des Elektron-Kanal ist $1159.79 \pm 7.1\,(\mathrm{stat})\,^{+102.8}_{-98.9}\,(\mathrm{syst}) \pm 32.4\,(\mathrm{lumi})\,\mathrm{pb}$. Die Ergebnisse stehen mit den theoretischen Ergebnissen innerhalb der systematischen Unsicherheiten in Übereinstimmung.

Contents

1. Introduction **1**

2. Physics **3**

2.1. Overview of the Standard Model 3

2.2. Formulation of a theory 4

2.3. The Standard Model 5

2.4. Quantum Chromodynamics 6

2.5. Electroweak unification 8

2.5.1. The GWS-model 8

2.5.2. Spontaneous symmetry breaking 10

2.5.3. Yukawa coupling 13

2.5.4. Precision measurements 14

3. Experimental Setup **15**

3.1. The LHC 15

3.1.1. Beam energy & luminosity 16

3.2. Physics at the LHC 18

3.2.1. Parton Distribution Functions 18

3.2.2. Particle production at the LHC 19

3.3. ATLAS 20

3.3.1. The Inner detector 21

3.3.2. Calorimeter 23

3.3.3. Muon system 24

3.3.4. Trigger systems 25

3.4. Event simulation 26

4. Phenomenology **29**

4.1. Electroweak precision measurements 29

4.2. The Higgs particle 29

4.2.1. Higgs production at the LHC 31

4.2.2. The decay of the Higgs boson . . . 31
4.2.3. Further Higgs studies . . . 33
4.3. The Z boson . . . 34
4.3.1. Prediction & observation of the Z boson . . . 34
4.3.2. Production & decay of the Z boson . . . 34
4.4. The τ-lepton . . . 37
4.4.1. Discovery of the tau lepton . . . 38

5. Analysis **39**
5.1. Selection of $Z \to \tau_{\text{lep}}\tau_{\text{had}}$ events . . . 39
5.1.1. Object definitions . . . 39
5.1.2. Background . . . 43
5.1.3. Event selection . . . 44
5.1.4. The cutflow . . . 52
5.1.5. Distributions of the signal region . . . 55
5.2. The template method . . . 58
5.2.1. Concept . . . 58
5.2.2. Studies of the assumptions . . . 59
5.2.3. Findings . . . 66
5.3. Cross section . . . 69
5.3.1. Systematics . . . 69
5.3.2. Fiducial cross section . . . 74

6. Conclusion **83**
6.1. Summary . . . 83
6.2. Outlook . . . 84

A. MC samples **86**

B. Event selection **89**

C. Template Method **91**

D. Cross section **95**

Nomenclature

Variable	Meaning	Unit[1]
$\not{E}_T$	Missing transverse energy	GeV
$\mathcal{L}$	Luminosity	$\mathrm{pb}^{-1}\mathrm{s}^{-1}$
$\int \mathcal{L}\,\mathrm{d}t$	Integrated luminosity	pb^{-1}
m	Mass	GeV
p_T	Transverse momentum	GeV
ΔR	Distance in η-ϕ plane	1
$\sqrt{s}$	Center-of-mass energy	TeV
Γ	Decay width	s^{-1}
η	Pseudo-rapidity	1
σ	Cross section	pb
ϕ	Angle around the axis of rotational symmetry of the ATLAS detector	rad

[1] In this thesis, natural units are used: $\hbar = c = 1$, where $\hbar$ is the reduced Planck constant and c is the speed of light.

Acronym	Meaning
ATLAS	A Toroidal LHC ApparatuS
BDT	Boosted decision tree
CERN	European Organization of Nuclear Research (French: Conseil Européen pour la Recherche Nucléaire)
CL	Confidence level
CMS	Compact Muon Solenoid
D3PD	Derived physics data
ECAL	Electromagnetic calorimeter
EF	Event filter
ElEnRes	Electron energy resolution

Acronym	**Meaning**
ElES	Electron energy scale
ggF	Gluon-gluon fusion
GWS-model	Glashow, Weinberg and Salam model
HCAL	Hadronic calorimeter
ID	Inner detector
JER	Jet energy resolution
JES	Jet energy scale
JVF	Jet vertex fraction
LAr	Liquid-argon detector
LEP	Large Electron Positron Collider
LHC	Large Hadron Collider
LTT	Lepton tau trigger
LO	Leading order
MC	Monte Carlo
NLO	Next-to-leading order
NNLO	Next-to-next-to-leading order
OS/SS	Opposite sign/same sign
PDF	Parton distribution function
PU	Pile-up
ROI	Regions of interest
QCD	Quantum chromodynamics
SCT	Semiconductor tracker
SLT	Single lepton trigger
SPS	Super Proton Synchrotron
SSB	Spontaneous symmetry breaking
TES	Tau energy scale
TRT	Transition radiation tracker
VBF	Vector boson fusion
VEV	Vacuum expectation value
VH	Vector boson associated Higgs production

1. Introduction

The Higgs particle is found. Is the Standard Model complete?

On the 4th of July 2012, the ATLAS and CMS experiments announced the discovery of a new particle with a mass around 126 GeV [1, 2]. This particle is assumed to be the predicted Higgs boson, but in order to ensure that it indeed is, further studies are needed to probe its nature and properties. Recently, the evidence for the fermionic Higgs coupling $H \to \tau\tau$ was confirmed by both collaborations [3, 4]. Furthermore, the precision of the measurement of the bosonic Higgs coupling was improved. Above all, spin studies comparing $J^P = 0^+$ and $J^P = 2^+$ exclude the latter spin configuration with a confidence level above 99.9 % [5, 6]. These results support that the found particle is indeed the Standard Model Higgs.

Given the observation of the Higgs, all predicted particles of the Standard Model have been discovered. While many of the predicted properties of the Higgs have been investigated, there are several further predictions which yet have to be verified [7–13]. Apart from first observations of couplings, the Standard Model offers more possibilities to check. It predicts precisely the strength of the couplings, leading to an enduring challenge to the experimental measurements and compare them to their theoretical expectations.

As previously indicated, the SM lacks answers to certain questions. Up to now, it does not provide any candidate for the dark matter [14]. Also gravitation cannot be included into this theory [15]. Hence, very precise results are desireable as even minor deviations of theoretical predictions and experimental measurements could points towards extensions of the SM.

In conclusion, particle physics and in particular Higgs physics is at an advanced stage, but it is far from being complete. In the scope of my thesis, an attempt to measure the cross section of $Z \to \tau_{lep}\tau_{had}$ at a center-of-mass energy of 8 TeV is made. This result is an important ingredient for the fermionic Higgs analysis $H \to \tau_{lep}\tau_{had}$, since this Z decay is an irreducible background for this particular Higgs decay channel. In addition, the measurement of a known process at unprecedented energies serves as a further cross check of the Standard Model.

2. Physics

2.1. Overview of the Standard Model

What is the world made of? The Standard Model of particle physics tries to answer this fundamental question. This model proposes a classification of all known particles and their interactions. First of all, this section gives a short and general overview of the different particle types, as well as their interactions. It will be followed by a bit more detailed description, which provides the theoretical background for this thesis.

Particles

All fundamental particles can be divided into the following two classes of particles: The fermions and the bosons. The former are particles with half-integer spin and form the matter. The electrons e^-, muons μ^-, and taus τ^- carry electric charge and thus they interact via the electromagnetic force. Each of these charged leptons ℓ is accompanied by an uncharged neutrino ν_ℓ and together, they form three lepton families. There are six flavours of electric and coloured charged quarks which interact via the electromagnetic and the strong interaction. All these particles are sensitive to the weak interaction as well. For each fermion, there is an anti-partner which has the opposite quantum numbers based on the CPT-theorem. Therefore, one can assign to every fermion ℓ^-, ν_ℓ, and q a corresponding anti-particle $\ell^+, \bar{\nu}_\ell, \bar{q}$.

All fermions have a non-zero mass, nevertheless the neutrino masses are supposed to be zero within the Standard Model. Indeed the observed neutrino oscillations [16–18] show that at least two of the neutrinos have non-zero masses since the oscillation is based on mass-difference of the particles. However, the integration of the masses into the Standard Model needs the information whether neutrinos are Dirac- or Majorana-particles which is still an unanswered question [19].

Finally all known bound states from molecules to baryons can be explained by a composite of these 12 fermions and their corresponding antiparticles. To be more specific, the world that we know is just made of up-/down-quarks and electrons, since all the other particles cannot form stable bound states in nature.

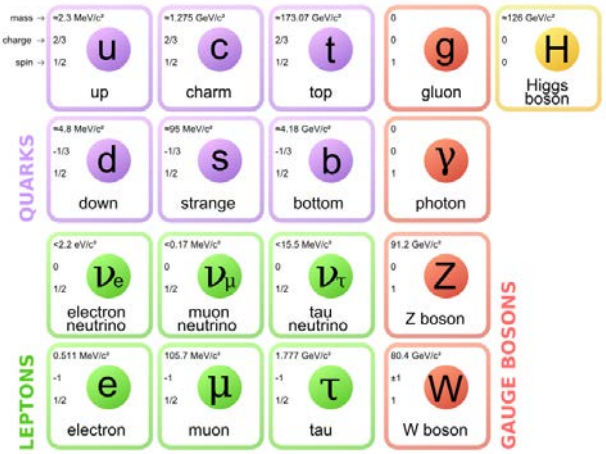

Figure 2.1.: List of all fundamental particles of the Standard Model [20].

The intermediate particles of these three interactions are spin-1 particles, the photons γ for the electromagnetic force, and $W^{\pm}$ and Z for the weak interaction, and gluons g for the strong force. In contrast to the $W^{\pm}$ and Z bosons, photons and gluons are massless.

In addition to that, there is one spin-0 (scalar) particle, the Higgs boson, which is the manifestation of the excitation of the Higgs field in the electroweak symmetry breaking mechanism. It is introduced to the Standard Model in order to give rise the masses of the gauge bosons.

A complete overview of all particles of the Standard Model is given in Figure 2.1 and a summary of the matter particles in Table 2.1.

2.2. Formulation of a theory

A very successful way to describe particles and their interactions is the formulation of quantum field theories. Analog to classical mechanics, the system can be described by a Lagrange function. Since a field ϕ is not a localized entity, it is a function of space time $\phi(\vec{r}, t)$. Therefore, it is appropriate to describe a system by a Lagrange density $\mathcal{L}$ or short Lagrangian, which depends on the fields ϕ_i and their derivatives $\partial_\mu \phi_i$. The index $\mu = 0..3$ indicates the four dimensions of the space-time. From a given Lagrange density $\mathcal{L}$, the equations of motion for all fields ϕ_i can be derived with the Euler-Lagrange equations

$$\partial_\mu \left(\frac{\mathcal{L}}{\partial(\partial_\mu \phi_i)} \right) = \frac{\partial L}{\partial \phi_i}. \tag{2.1}$$

In quantum field theories, the Lagrange density is the starting point of a theory which cannot be derived. Nevertheless, the formulation can be restricted by some postulates which one wants to be fulfilled. These restrictions are commonly formulated by the invariance of the Lagrangian under certain symmetry transformations, such as the claim for a relativistic theory which is expressed by the Lorentz invariance. According to the Noether theorem, imposed symmetries of the Lagrangian become manifest in conservation laws [21]. Hence, the Lorentz invariance implies the four-momentum conservation. More generally, one asks for invariance under the proper Poincare group, which additionally leads to the momentum and angular momentum conservation.

The derivation of the Lagrangian just from symmetry requirements is a common objective of theoretical physicists. A successful way to describe the fundamental particles and their interactions is to require the Lagrangian to be symmetric under local gauge transformations. This approach introduces a group G and particles are grouped into multiplets which form the representation of that group. By requiring the Lagrangian to be invariant under a local group transformation, massless gauge fields have to be introduced, which form the mediator of the interaction. These local gauge symmetries imply new conserved quantities, which can be identified as the charge of the interaction.

A major advantage of local gauge theories is, that one gets renormalizable theories. The renormalization is the procedure to avoid divergences. One redefines some parameters by subtracting an infinite but explicitly defined value. If a finite number of renormalized parameters is sufficient to cancel all divergences, a theory is renormalizable and the perturbative approach to calculate probabilities of processes is accredited.

2.3. The Standard Model

All today's interactions can be reduced to four fundamental forces. In order of magnitude, these are the gravitational force, the weak interaction, the electromagnetic interaction and the strong interaction. The gravitational force is the only one which still is described by a classical field theory instead of a quantum field theory due to the still challenging task of unifying general relativity with quantum mechanics. Therefore, the classical approach to describe gravity simply is a low energy approximation which will presumably fail at the Planck-scale at a distance of $\mathcal{O}(10^{-35})\,\mathrm{m}$ as soon as the quantum characteristics will become dominant [22]. Since gravity is negligible in the accessible energy scale of today's particle physics experiments, it has not yet been necessary to include this interaction into the field-tested Standard Model of particle physics.

Thus, the Standard Model describes the remaining three fundamental interactions by

a quantum field theory. These interactions are modeled by local gauge theories [15]. The symmetry-group of the Standard Model is

$$SU(3)_C \times SU(2)_L \times U(1)_Y. \tag{2.2}$$

The first factor describes the strong interaction, namely the quantum chromodynamics, the colour charge, and the coupling strength g_s. It is followed by the group product $SU(2)_L \times U(1)$ for the electroweak interaction, the unification of the electromagnetic and the weak interaction. The gauge bosons of the electroweak interaction cannot directly be identified with the vector bosons since this gauge symmetry is spontaneously broken and the physical states are linear combinations of these gauge bosons. This leads to the intermediate gauge bosons $W^{\pm}$, Z of the weak interaction, and the photon γ of the electromagnetic interaction.

2.4. Quantum Chromodynamics

The theoretical description of the strong interaction is quantum chromodynamics (QCD). This interaction is a non-Abelian gauge theory based on a non-chiral and unbroken local $SU(3)_C$ symmetry-group. It implies that there are eight gauge bosons, the gluons which couple to colour-charged particles. These are the six flavours of quarks, u, d, c, s, t, and b. The additional charge can assume three values, namely red, green, blue, and the corresponding anti-colours. It represents the quantum number according to the triplet representation of the gauge group.

The Lagrangian of QCD is

$$\mathcal{L} = \sum_q \bar{\Psi}_{q,a}(i\gamma^\mu \partial_\mu \delta_{ab} - g_s \gamma^\mu t^C_{ab} \mathcal{A}^C_\mu - m_q \delta_{ab})\Psi_{q,b} - \frac{1}{4} F^A_{\mu\nu} F^{A\mu\nu}, \tag{2.3}$$

where γ^μ are the Dirac matrices, $\Psi_{q,a}$ are the quark-field spinors for a quark of the flavour q and mass m_q with a colour index a, which runs from $a = 1$ to 3. $\mathcal{A}^C_\mu$ represent the $C = 1..8$ gluon fields with the generators t^C_{ab}. The last term is the field tensor $F^A_{\mu\nu}$ defined by

$$F^A_{\mu\nu} = \partial_\mu \mathcal{A}^A_\nu - \partial_\nu \mathcal{A}^A_\mu - g_s f_{ABC} \mathcal{A}^B_\mu \mathcal{A}^C_\nu, \tag{2.4}$$

with the structure constants f_{ABC} of the $SU(3)$ group defined by [23]

$$[t^A, t^B] = i f_{ABC} t^C. \tag{2.5}$$

The theory is non-Abelian which results in coloured gluons. Therefore, gluons couple not only to quarks but also to gluons. This has a critical impact on the coupling constant of the strong interaction. Higher-order vacuum polarization can be parameterized in an effective running coupling constant $g_s(\mu^2)$ depending on the renormalization scale μ. The $q\bar{q}$ loops shield the charge of the gluon, such that the effective coupling decreases for long distances (see Figure 2.2). In contrast to that, the gluon self-coupling allows for gluon-loops which lead to the opposite and furthermore dominant effect. Finally, the coupling strength of the strong interaction becomes weaker on short distances and stronger on long distances.

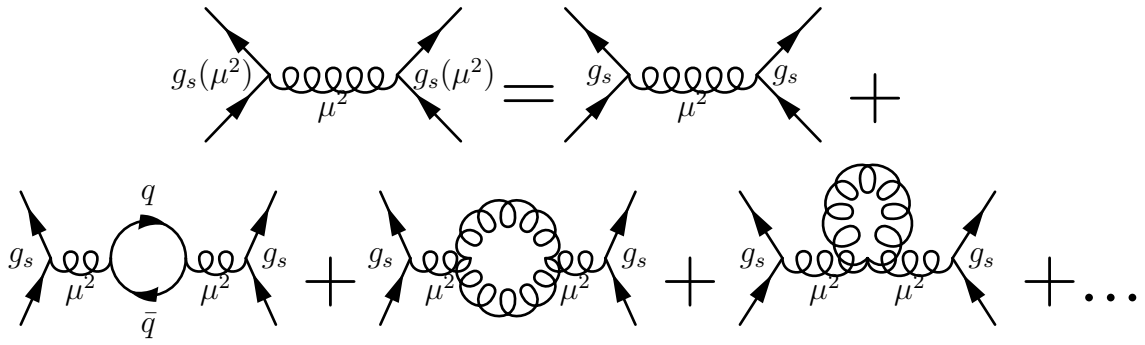

Figure 2.2.: Effective propagator of a gluon: The first diagram with the quark-loop leads to a decrease of the effective coupling constant $g_s(\mu^2)$ and the diagrams with gluon loops have the opposite but dominant effect.

At long distances $|Q| \approx 1\,\mathrm{GeV}$ quarks interact strongly $g_s = \mathcal{O}(1)$ such that free quarks form immediately uncoloured bound states. Bound $q\bar{q}$ states, *mesons*, with the colour-configuration $r\bar{r}$, $g\bar{g}$ or $b\bar{b}$ and bound states of three quarks, the *baryons*, with the colour-configuration rgb or $\bar{r}\bar{g}\bar{b}$ form colour-neutral hadrons. The assumption that there is no observation of free quarks is referred to as *colour confinement*.

In contrast, at short distances and accordingly high energy regions $Q \gg 1\,\mathrm{GeV}$ respectively the strong coupling is weak $g_s \ll 1$. This so-called *asymptotic freedom* allows treating bound quarks of hadrons as free point-like particles whose interaction can be described by perturbative QCD. For example the theoretical description of an electron in deep inelastic scattering ($e^- p \to e^- + X$) reduces to a scattering of point-like particles [24, 25]. The following processes of the remaining hadron and the scattered quark's hadronisation are in turn a non-perturbative QCD series which can be treated independently of the initial scattering process by hadronisation models.

2.5. Electroweak unification

The weak interaction was initially introduced to describe the nuclear β decay which was first discovered at the end of the 19th century [26, 27]. In 1933, Enrico Fermi made the first attempt to describe the decay $n \to pe^-\bar{\nu}$ by direct coupling of these four fermions proportional to the Fermi coupling constant G_F [28, 29]. The original theory could be adapted successfully to several new observations such as the parity violation [30]. Nevertheless, the weak spot of the theory is the non-renormalizability of the theory, due to the 4-point interaction, which becomes manifest in divergencies. Therefore, Glashow, Weinberg, and Salam (GWS) proposed the electroweak unification in the late 1960s, which offers a common description of the electromagnetic and weak force [31–33].

2.5.1. The GWS-model

The GWS-model is a gauge theory based on the symmetry-group $SU(2)_L \times U(1)_Y$ postulating a gauge boson triplet $W^i, i \in 1, 2, 3$ represented by the three generators of the $SU(2)$ group with the coupling strength g and furthermore a gauge boson B belonging to the symmetry group $U(1)$ with the coupling constant g'. The first subscript indicates that the triplet of bosons couples only to the left-handed particles. Mathematically, the coupling rotates the particles in a 2-dimensional vector-space of this weak isospin. The gauge boson B of $U(1)_Y$ couples to left- and right-handed particles, but the coupling depends on the differing weak hypercharge Y_W.

Within this description, the left-handed particles form weak isospin doublets with $T_3 = \pm\frac{1}{2}$ and the right-handed singlets with $T_3 = 0$. The weak isospin, the colour charge, and the weak hypercharge

$$Y_W = Q - T_3, \tag{2.6}$$

give an ensemble of quantum numbers which predicts the possible interactions. The left-handed fermions can be combined in doublets

$$Q_k = \begin{pmatrix} u_k \\ d'_k \end{pmatrix}_L, \quad L_k = \begin{pmatrix} \nu_k \\ \ell'_k \end{pmatrix}_L \tag{2.7}$$

where the $k = 1, 2, 3$ indicates the family and the prime emphasizes that the particles are the weak eigenstates which in general do not coincide with observed mass eigenstates,

such as quarks. The right-handed particles form singlets

$$u_m = (u_k)_R, \quad d_m = (d'_k)_R, \quad \ell_k = (\ell_k)_R \tag{2.8}$$

Obviously, all these particles carry weak hypercharge. A possible right-handed neutrino has neither a non-zero weak isospin nor a non-zero hypercharge. Since the colour charge is zero as well, a right-handed neutrino would not interact within the description of the Standard Model.

Table 2.1.: Quantum numbers of the matter-particles.

Particle	**Colour**	**El. charge** Q	**Weak isospin** T_3	**Weak hypercharge** Y_W
ν_L^e, ν_L^μ, ν_L^τ	0	0	$\frac{1}{2}$	$-\frac{1}{2}$
e_L^-, μ_L^-, τ_L^-	0	-1	$-\frac{1}{2}$	$-\frac{1}{2}$
e_R^-, μ_R^-, τ_R^-	0	-1	0	-1
u_L, c_L, t_L	r/g/b	$\frac{2}{3}$	$\frac{1}{2}$	$\frac{1}{6}$
d_L, s_L, b_L	r/g/b	$-\frac{1}{3}$	$-\frac{1}{2}$	$\frac{1}{6}$
u_R, c_R, t_R	r/g/b	$\frac{2}{3}$	0	$\frac{4}{3}$
d_R, s_R, b_R	r/g/b	$-\frac{1}{3}$	0	$-\frac{2}{3}$

The final Lagrangian density of the elaborated electroweak theory is

$$\mathcal{L} = \mathcal{L}_{gauge} + \mathcal{L}_f + \mathcal{L}_\phi + \mathcal{L}_{Yuk}, \tag{2.9}$$

devided in the gauge, fermion, Higgs, and Yukawa terms of the theory. The first term in Equation 2.9 describes the gauge-fields with the self-interaction of the SU(2)-group since it is a non-Abelian group

$$\mathcal{L}_{gauge} = -\frac{1}{4} W^i_{\mu\nu} W^{\mu\nu i} - \frac{1}{4} B_{\mu\nu} B^{\mu\nu}, \tag{2.10}$$

with the field tensors for the SU(2) and U(1) groups

$$W^i_{\mu\nu} = \partial_\mu W^i_\nu - \partial_\nu G^i_\mu - g\epsilon_{ijk} W^j_\mu W^k_\nu \qquad i,j,k = 1,2,3 \tag{2.11}$$

$$B_{\mu\nu} = \partial_\mu B_\nu - \partial_\nu B_\mu. \tag{2.12}$$

The second term $\mathcal{L}_f$ is the fermionic sector of the Lagrangian which describes actually the weak interaction of the fermions. Thus, this part of the Lagrangian describes the mentioned coupling of the fermions and the gauge bosons.

$$\mathcal{L}_f = \sum_{k=1}^{3} (\bar{Q}_k \not{D} Q_k + \bar{L}_k \not{D} L_k + \bar{u}_k i \not{D} u_k + \bar{d}'_k i \not{D} d'_k + \ell'_k i \not{D} \ell'_k), \tag{2.13}$$

$\not{D} = \gamma^\mu D_\mu$ is the covariant derivative applied to weak-isospin doublets and singlets

$$D_\mu L_k = \left(\partial_\mu I_2 + \frac{ig}{2}\vec{\tau}\cdot\vec{W}_\mu + ig'YI_2B_\mu\right) L_k \tag{2.14}$$

$$D_\mu \ell_k = \left(\partial_\mu + ig'YB_\mu\right) \ell_k, \tag{2.15}$$

where I_2 is the unitary Matrix of $\mathbb{R}^2$ and $\sigma_i, i = 1, 2, 3$ are the Pauli matrices.

2.5.2. Spontaneous symmetry breaking

Since the gauge symmetry of the electroweak interactions forbids mass terms for the gauge bosons and fermions, the symmetry has to be broken [34–36]. This process, named spontenous symmetry breaking (SSB), can be achieved by the additional Higgs term $\mathcal{L}_\phi$ in the Lagrangian in Equation 2.9. Therefore, one has to add a new field with a potential of a non-zero vacuum expectation value (VEV), which couples to the experimentally massive gauge bosons. The minimalistic extension of the unbroken model to generate the gauge boson masses and preserve a $U(1)_Q$ symmetry is one weak isospin doublet of complex scalars

$$\phi = \begin{pmatrix}\phi^+ \\ \phi^0\end{pmatrix} = \begin{pmatrix}\frac{1}{\sqrt{2}}(\phi_1 + i\phi_2) \\ \frac{1}{\sqrt{2}}(\phi_3 + i\phi_4)\end{pmatrix}. \tag{2.16}$$

Thus the contribution of this new field to the Lagrangian is generally

$$\mathcal{L}_\phi = (D^\mu\phi)^\dagger(D_\mu\phi) - V(\phi). \tag{2.17}$$

The $SU(2)_L \times U(1)_Y$ symmetry, the requirement of a non-zero VEV, and the renormalizability of the theory restricts the Higgs potential $V(\phi)$ to

$$V(\phi) = +\mu^2\phi^\dagger\phi + \lambda(\phi^\dagger\phi)^2. \tag{2.18}$$

If $\mu^2 < 0$, the ground state of this potential is

$$\nu = \sqrt{\frac{-\mu^2}{\lambda}},\ \nu \in \mathbb{R} \tag{2.19}$$

In order to maintain vacuum stability, $\lambda > 0$ has to be fullfilled [30]. Figure 2.3 shows the potential reduced to two degrees of freedom instead of four. One can observe a general rotation symmetry of this mexican-hat potential around zero, which can be read off the Lagrangian of Equation 2.17.

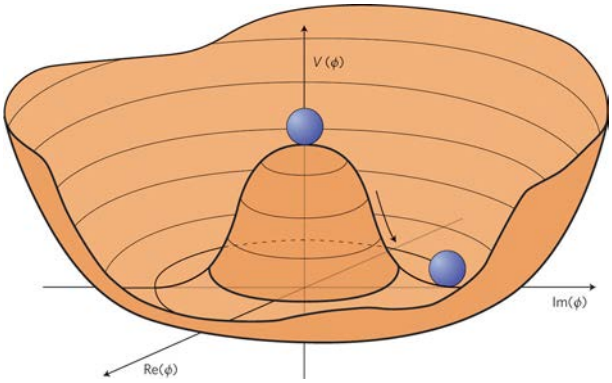

Figure 2.3.: The Higgs potential reduced to two dimensions by using the gauge freedom to set $\Phi^+ = 0$ [37].

If the neutral component of the Higgs doublet ϕ^0 has a non-zero VEV ν, the Higgs doublet can be chosen in a Hermitian basis such that the non-zero ground state ϕ_{min} with the VEV v of Equation 2.19 is

$$\phi_{min} \equiv \langle 0|\phi|0\rangle = \frac{1}{\sqrt{2}}\begin{pmatrix}0\\ v\end{pmatrix}. \tag{2.20}$$

To see the particle content directly from the Lagrangian, it is useful to make an expansion of it around this taken ground state. Since an arbitrary gauge can be chosen, a particular choice is possible such that three components vanish.

$$\phi = \frac{1}{\sqrt{2}}\begin{pmatrix}\phi_1 + i\phi_2\\ \nu + H + i\eta\end{pmatrix} \xrightarrow{gauge freedom} \phi' = \frac{1}{\sqrt{2}}\begin{pmatrix}0\\ \nu + H\end{pmatrix}, \tag{2.21}$$

where H is the real Higgs field which describes the remaining degree of freedom. The expansion of the Lagrangian of the Higgs part $\mathcal{L}_\phi$ in Equation 2.17 results in

$$\begin{aligned}\mathcal{L}_{\phi'} = &\underbrace{\frac{g^2\nu^2}{4}}_{m_W^2} W^{\mu+}W_\mu^- \left(1+\frac{H}{\nu}\right)^2 + \frac{1}{2}\underbrace{(g^2+g'^2)\frac{\nu^2}{4}}_{m_Z^2}\underbrace{\left[\frac{-g'B_\mu + gW_\mu^3}{\sqrt{g^2+g'^2}}\right]}_{Z^\mu Z_\mu}\left(1+\frac{H}{\nu}\right)^2\\ &+\frac{1}{2}(\partial H)^2 - V(\phi')\end{aligned} \tag{2.22}$$

with the expanded Higgs potential

$$V(\phi') = -\frac{\mu^4}{4\lambda} - \mu^2 H^2 + \lambda\nu H^3 + \frac{\lambda}{4}H^4. \tag{2.23}$$

The Lagrangian in Equation 2.22 describes the same physics as before. Nevertheless, this representation offers a more intuitive access to the perturbative calculation of possible processes. The expanded Lagrangian does not preserve three gauge symmetries, since they are used to fix the representation of Equation 2.21.

Defining the Weinberg angle θ_W

$$\tan\theta_W = \frac{g'}{g} \tag{2.24}$$

the physical fields Z from the weak neutral current and A from the electromagnetic interaction occur as rotations of the fields W^3 and B

$$Z_\mu = \frac{-g'B_\mu + gW_\mu^3}{\sqrt{g^2+g'^2}} = -\sin\theta_W B_\mu + \cos\theta_W W_\mu^3 \tag{2.25}$$

$$A_\mu = \cos\theta_W B_\mu + \sin\theta_W W_\mu^3. \tag{2.26}$$

Finally, this expansion of the Lagrangian shows that the spontaneous symmetry breaking leads to massive gauge bosons $W^\pm$ and Z with the masses at leading order of

$$m_Z = \frac{1}{2}\sqrt{g^2+g'^2}\,\nu = \frac{m_W}{\cos\theta_W} \tag{2.27}$$

$$m_W = \frac{1}{2}g\nu \tag{2.28}$$

which can be interpreted in this scope as interactions of the bosons with the Higgs vacuum. The photon indeed remains massless due to the unbroken symmetry. The coupling constant of the electromagnetic interaction can be specified in terms of the electroweak theory by

$$e = g\sin\theta_W. \tag{2.29}$$

As well as one can describe the Fermi-Coupling constant in these terms, which results in

$$G_F = \frac{\sqrt{2}}{8}\frac{g^2}{m_W^2} = \frac{\nu^2}{2}. \tag{2.30}$$

The Equations 2.27-2.30 offer an overconstrained system of equations of the three parameters g, g', and ν, such that one could predict the Z mass, which was unknown up to the publication of this theory. The later observation of the Z boson was the first great success of the GWS-model [38].

The Higgs doublet added four degrees of freedom to the theory. Three of them manifest

as the longitudinal components of the gauge bosons. The last one shows up, as one can see in Equation 2.23, in form of a massive scalar particle of the mass

$$m_H = \sqrt{-2\mu^2} = \sqrt{2\lambda}\nu\,. \tag{2.31}$$

At leading order, the parameter λ does not occur in Equation 2.27-2.30, thus a prediction of the Higgs mass is not precisely possible. For the first time, the direct observation and the mass reconstruction of the Higgs boson, with the mass of $m_H = (126.0 \pm 0.4\,(stat) \pm 0.4\,(sys))$ GeV according to the observation by the ATLAS collaboration, allowed to infer the missing parameter of the Standard Model [1, 2].

2.5.3. Yukawa coupling

The last term in the electroweak Lagrangian in Equation 2.9 is the Yukawa term which inserts the fermion masses into the model via the Yukawa coupling.

$$\mathcal{L}_{Yuk} = -\sum_{k,n=1}^{3} \left(\Gamma^u_{kn}\bar{Q}_k\widetilde{\phi}u_n + \Gamma^d_{kn}\bar{Q}_k\phi d_n + \Gamma^e_{kn}\bar{L}_k\phi\ell_n\right) + h.c. \tag{2.32}$$

where

$$\widetilde{\phi} = i\tau^2\phi^\dagger\,. \tag{2.33}$$

The terms Γ^l_{kn} parametrizes the mixing and the masses of leptons which leads to the breaking of almost all symmetries of the fermions. Since there is no known more fundamental theory which could deliver these parameters, they have to be extracted from experimental results. Just a few empirical conservation laws as the lepton-number conservation remain.

Analogue to the expansion of the Lagrangian $\mathcal{L}_\phi$ around the VEV of the Higgs field, this procedure would show the mass terms of the fermions.

If the mass eigenstates and the weak eigenstates are not the same, the fermions will be mixed. This occurs when a fermion of weak-isospin $T_3 = +\frac{1}{2}$ couples via the weak interaction to fermions of $T_3 = -\frac{1}{2}$ of another family as well. In the quark sector this is a known and well measured phenomenon. It is common to write the transition from weak to mass eigenstates with the Cabibbo-Kobayashi-Maskawa-Matrix V_{CKM} as a rotation of

the down-type in a mass eigenstates $\binom{u}{d}$ to the weak eigenstates doublet $\binom{u}{d'}$ by

$$V_{CKM} \begin{pmatrix} d_L \\ s_L \\ b_L \end{pmatrix} = \begin{pmatrix} d'_L \\ s'_L \\ b'_L \end{pmatrix} \tag{2.34}$$

with the CKM-Matrix V_{CKM} [39]

$$V_{CKM} = \begin{pmatrix} V_{ud} & V_{us} & V_{ub} \\ V_{cd} & V_{cs} & V_{cb} \\ V_{td} & V_{ts} & V_{tb} \end{pmatrix} \tag{2.35}$$

$$= \begin{pmatrix} 0.97427 \pm 0.00015 & 0.22534 \pm 0.00065 & 0.00351^{+0.00015}_{-0.00014} \\ 0.22520 \pm 0.00065 & 0.97344 \pm 0.00016 & 0.0412^{+0.0011}_{-0.0005} \\ 0.00867^{+0.00029}_{-0.00031} & 0.0404^{+0.0011}_{-0.0005} & 0.999146^{+0.000021}_{-0.000046} \end{pmatrix} . \tag{2.36}$$

2.5.4. Precision measurements

The parameters for the particle masses and couplings, which can directly be read from the Lagrangian, represent just the tree-level approximation. These values arise only if the leading order contribution is considered in the perturbative approach. Naturally the measured values imply all elements of a series expansion. Since the correction of higher order elements are supposed to be small, one parametrizes the correction between the tree-level value and the effective value commonly in correction factors.

Instead of the four parameters g, g', λ, and μ^2, one cites these values rather in terms, which are directly measurable in experiments. These are usually the Fermi constant G_F, the fine structure constant α, the W and Z mass, and the Weinberg angle $\sin^2\theta_W$. The relation of Equation 2.27 only holds at tree-level. Considering loop corrections, the deviation can be parameterized by

$$\rho = \frac{1}{1 - \sin^2\theta_W} \left(\frac{m_W}{m_Z}\right)^2 . \tag{2.37}$$

The expansion of the correction factor yields at leading order corrections proportional to m_t^2 and $\ln m_H$

$$\rho = 1 + \mathcal{O}(m_t^2) + \mathcal{O}(\ln m_H) \tag{2.38}$$

3. Experimental Setup

3.1. The LHC

The Large Hadron Collider (LHC) [40] is the world's most powerful particle accelerator. It is a synchrotron and corresponds to the final step of an acceleration chain of several machines located at the European Organization of Nuclear Research (CERN) designed to accelerate hadrons up to energies of 7 TeV (see Figure 3.1). The whole complex consists of different accelerators, which are used successively to reach the final energy, and several particle detectors specialized for different fields.

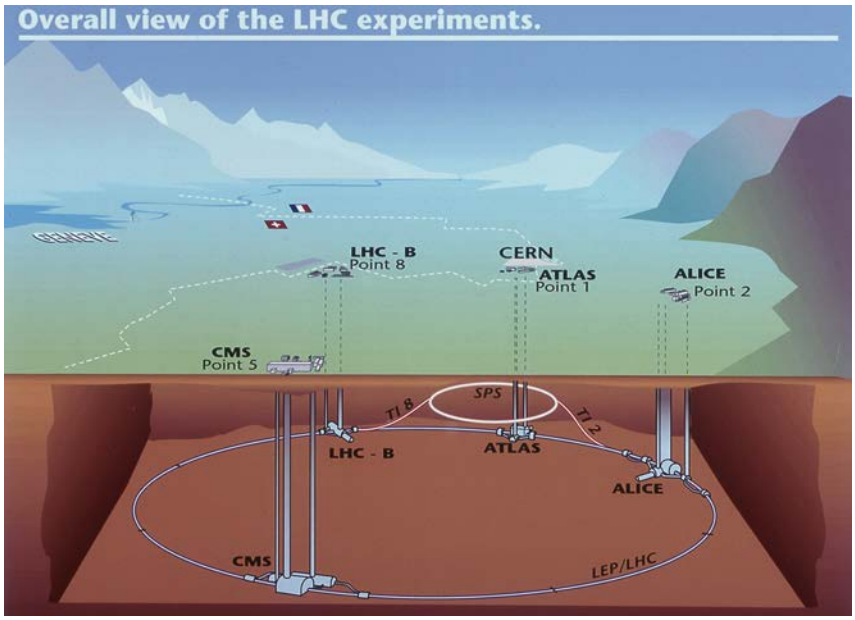

Figure 3.1.: An overview of the LHC experiments [41].

The LHC itself contains two vacuum pipes to circulate two proton beams in opposite directions. They are installed in a roughly 27 km long tunnel which was previously built for the preceeding Large-Electron-Positron Collider (LEP) [42] between 1984 and 2000. To hold the beams on the circular path, to focus the beam and finally to accelerate the hadrons, superconducting dipole- and quadrupole-magnets and cavities are used. The

operating temperature of such superconducting magnets is 1.8 K, such that the whole system has to be cooled down, which is realized by using superfluid helium [43].

The two beam pipes have four crossing points where the beam collisions are produced. There, the experiments CMS [44], ALICE [45], LHCB [46], and ATLAS [47] are situated. CMS and ATLAS are both general-purpose particle detectors, as opposed to LHCB and ALICE which are specialized in b-physics and heavy ion physics.

3.1.1. Beam energy & luminosity

The main characteristics of a particle accelerator in the scope of data analysis are the beam energy and the luminosity. During the launch of the LHC in 2008 there was a quench, the unexpected loss of the superconductivity of the magnets leading to heating and electric arcs, which resulted in a major mechanical damage of the magnets and the beam pipe likewise in a loss of a great amount of helium [48]. One consequence was that the LHC started after the repairs with lower energy of 3.5 TeV per beam in 2011, increasing to 4 TeV in 2012. In the beginning of 2013, the LHC was shut down to prepare the increase of the beam energy to 7 TeV per beam of Run II.

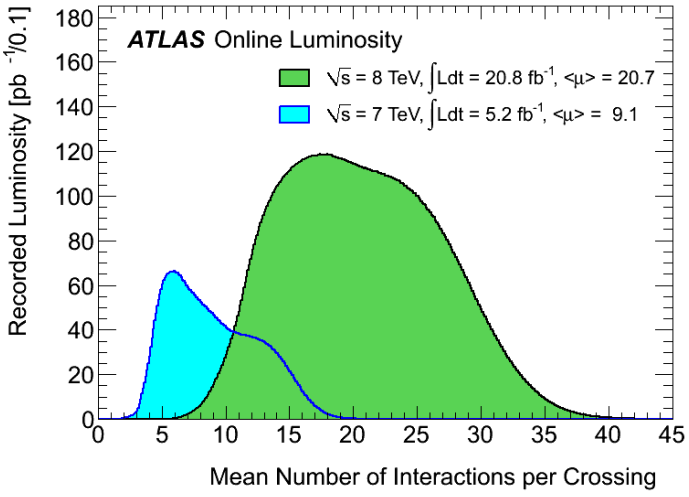

Figure 3.2.: Luminosity-weighted distribution of the mean number of interactions per crossing for the 2011 and 2012 data [49].

Besides the energy of the particles the instantaneous luminosity $\mathcal{L}$, a measure of the beam intensity,

$$\mathcal{L} = \frac{f n_b N^2}{4\pi\sigma_x\sigma_y}, \tag{3.1}$$

is a crucial quantity, where f is the frequency, n_b is the number of bunches, and N the number of protons per bunch. Due to the production chain of several accelerators, the beam consists - in contrast to a continuous beam of several bunches of protons. Depending on the focus of the packages and number of hadrons, several proton-proton collisions per bunch crossing are expected. Figure 3.2 shows that the mean number of interactions per crossing was around 9 at a center-of-mass energy of $\sqrt{s} = 7\,\text{TeV}$ and 21 at $\sqrt{s} = 8\,\text{TeV}$. This pile-up has to be taken in account, since the overlay of different scattering processes can imitate signal processes.

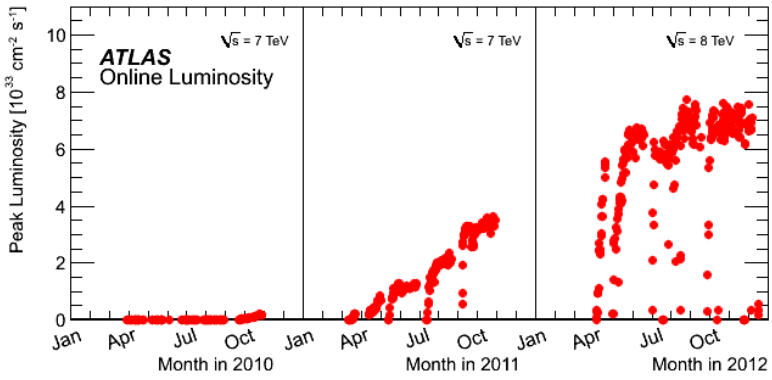

Figure 3.3.: The peak instantaneous luminosity delivered to ATLAS per day versus time during the proton-proton runs of 2010, 2011, and 2012 [49].

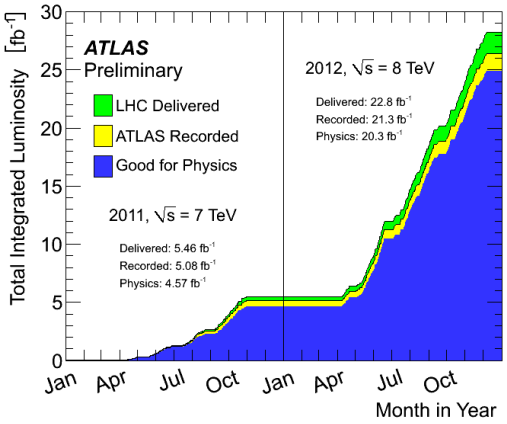

Figure 3.4.: Cumulative integrated luminosity versus time delivered to (green), recorded by ATLAS (yellow), and certified to be good quality data (blue) during stable beams and for pp collisions at $\sqrt{s} = 7\,\text{TeV}$ and 8 TeV in 2011 and 2012 [49].

The instantaneous luminosity describes the beam intensity, such that the expected event

rate of a process $\frac{\partial N}{\partial t}$ can be calculated by

$$\frac{\partial N}{\partial t} = \sigma \mathcal{L}, \tag{3.2}$$

where σ is the cross section of the explored process. The instantaneous luminosity is strongly time-dependent, as one can see in Figure 3.3, and has to be well known, since it enters all measured cross sections. The integrated luminosity $\int \mathcal{L}\,\mathrm{d}t$ serves as measure to quantify the amount of recorded data.

Figure 3.4 shows that $\int \mathcal{L}\,\mathrm{d}t = 5.08\,\mathrm{fb}^{-1}$ were recorded at energies of $\sqrt{s} = 7\,\mathrm{TeV}$ and $\int \mathcal{L}\,\mathrm{d}t = 21.3\,\mathrm{fb}^{-1}$ for $\sqrt{s} = 8\,\mathrm{TeV}$ by the ATLAS experiment.

3.2. Physics at the LHC

3.2.1. Parton Distribution Functions

The particles in the interaction, the constituents of the protons, carry only a fraction of the proton's momentum which is unknown for a single process. But one can give a statement about the probability that a parton carries a certain fraction of the energy. This knowledge is summarized in Parton Distribution Functions (PDFs) which return the probability $f_i(x, Q)$ that a parton of flavour i (quark or gluon) carries the momentum fraction x probed at a 4-momentum transfer square Q^2. The PDFs cannot be predicted from perturbative QCD, such that they are inferred from experimental results of deep inelastic scattering. There exist different approaches to extract the PDFs, depending on the choice of a factorization scheme, an order of perturbation theory (Leading order (LO), Next-to-Leading Order (NLO), NNLO, ...) and the starting scale of perturbative QCD. As an example, the results from Martin, Stirling, Thorne and Watt for energies of the LHC are shown in Figure 3.5.

The ignorance of the longitudinal momentum carried by the scattered partons leads to a crucial experimental drawback. Just the missing transverse momentum allows to infer the appearance of such a particle. In contrast to lepton colliders, the longitudinal momentum of the scattering particles is unknown in hadron colliders. Thus, one can just use the transverse constraint

$$\sum_i \vec{p}_T^{\,(i)} = 0 \tag{3.3}$$

to draw conclusions from. This motivates the definition of the missing transverse momen-

tum

$$\vec{\not{p}}_T = -\sum_{\text{measured } i} \vec{p}_T^{\,(i)}, \tag{3.4}$$

where the sum only runs over the measured momenta. Moreover, the center-of-mass energy of the parton-parton collision can not be deduced, since the proton remnants are typically lost in the beam pipe.

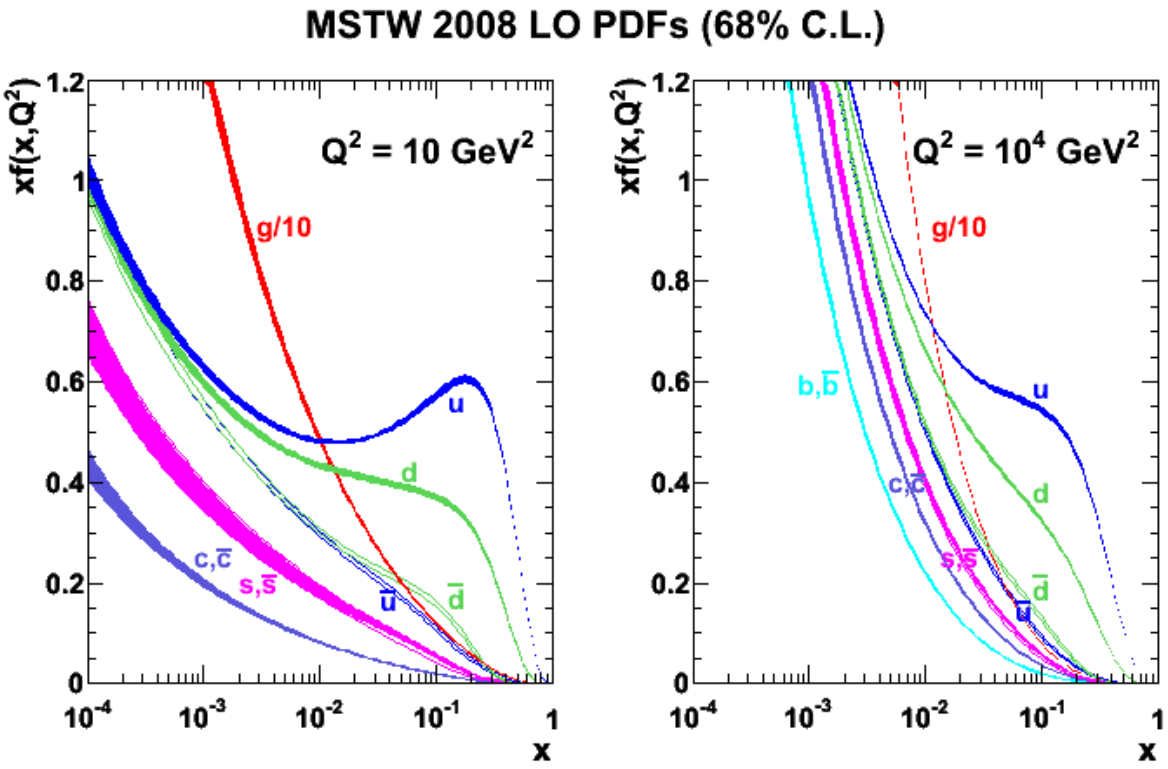

Figure 3.5.: Parton Distribution Functions [50].

3.2.2. Particle production at the LHC

Proton-proton collisions offer a wide spectrum of produced particles. Figure 3.6 provides an insight into the cross sections of the different processes depending on the center-of-mass energy $\sqrt{s}$. Visibly, the production of QCD multijet events is the main contribution to the total cross section and it is a general challenge to discard such events in order to study electroweak processes. In the scope of Higgs searches one has to sort through about 10^{10} events to find on average one event containing a Higgs boson.

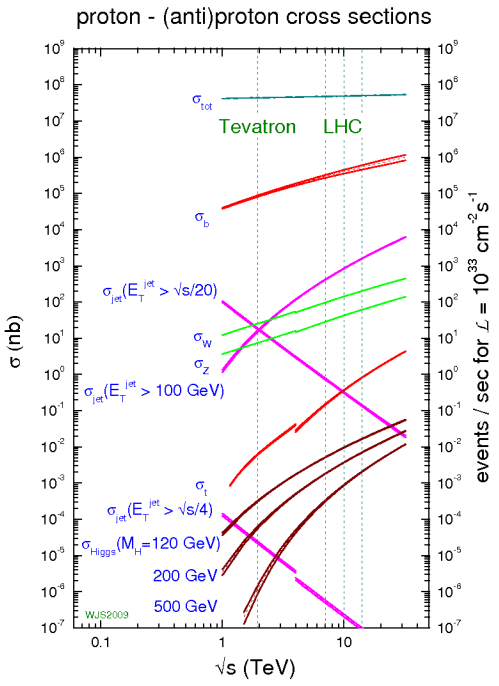

Figure 3.6.: Production cross sections with proton (anti)-proton collisions [50].

3.3. ATLAS

Two general purpose detectors are installed at the interaction points of the LHC. These are the *Compact Muon Solenoid* (CMS) and *A Toroidal LHC ApparatuS* (ATLAS)[51, 52]. The physics program of ATLAS is very wide. It comprises high precision tests of QCD and electroweak interactions, flavour physics and the search for supersymmetric particles. Nevertheless, the benchmark of the technical design is the Higgs search. At the detector's design time, the mass of the Higgs particle was unknown, such that it was not clear, which decay channel would be predestined to observe the Higgs particle. Beyond the discovery of the Higgs particle, it was intended to measure its couplings, too. These expectations lead to multifaceted but still precise detection faculties to implement. At the same time the detector has to handle a peak luminosity of $10^{34}\,\mathrm{cm}^{-1}\mathrm{s}^{-1}$, which in addition requires a radiation hard detector and great computing power to manage the data [53].

It is useful to mention some conventions to describe particles detected by the ATLAS detector. In general, the interaction point of the hadrons is set as the origin of the coordinate system. The z-axis is in the direction of the beam and the x-y-plane is transverse to it. The positive x-axis points to the center of the LHC ring and the positive y-axis points

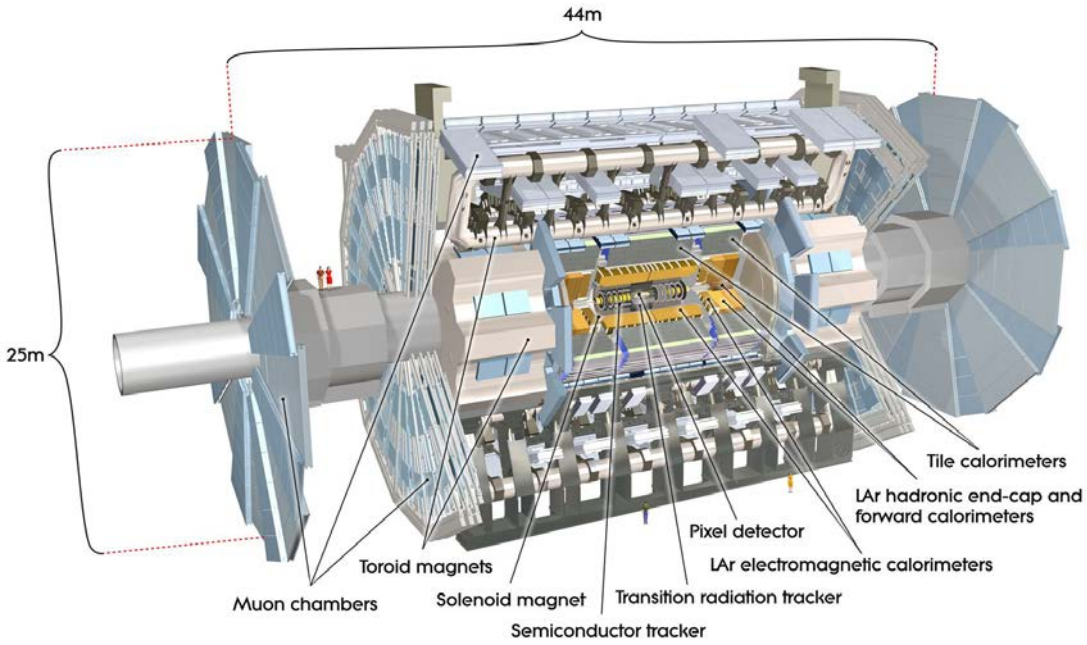

Figure 3.7.: The full ATLAS detector.

upwards. As usual, the azimuth angle ϕ is defined around the beam axis and the polar angle θ is the angle relative to the beam. The pseudo-rapidity η is defined by

$$\eta = -\ln \tan \frac{\theta}{2} \tag{3.5}$$

and the distance ΔR in the η-ϕ plane is given by

$$\Delta R = \sqrt{\Delta\eta^2 + \Delta\phi^2}. \tag{3.6}$$

ATLAS is a forward-backward symmetric detector due to the symmetric beam pipes. It consists of three detection systems. Starting from the center, these are the inner detector surrounded by a superconducting solenoid, the calorimeters surrounded by three superconducting toroids and the muon system.

3.3.1. The Inner detector

The Inner Detector (ID) is composed of three tracking systems surrounded by a solenoid with magnetic field of 2 T. The ID offers the capacity to measure with high precision particle momenta and to determine primary and secondary vertices. It is divided into three independent subsystems, namely the Pixel detector, the Semiconductor Tracker

(SCT), and the Transition Radiation Tracker (TRT). The pixel detector is the innermost lying detector and it consists of three layers of silicon modules. The first layer is located at a distance of 5.05 cm from the intersection point and the last one at 12.25 cm. The pixels have a size of $50 \times 400\,\mu m^2$ (or $50 \times 600\,\mu m^2$ on the edge).

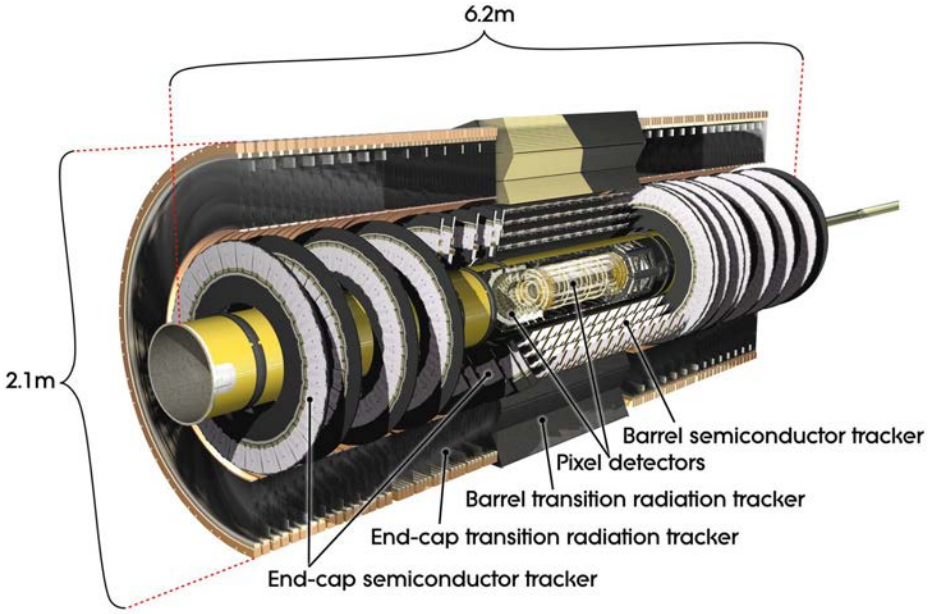

Figure 3.8.: The ATLAS Inner Detector.

Around the pixel detectors, the SCT is built. The silicon microstrips are located in the barrel region from 25.5 cm to 54.9 cm in four layers and 9 layers from 25.1 cm to 61.0 cm in the end-caps. This gives at least four high precision space-point measurements of passing charged particles. The in plane-lateral resolution is 17 µm and the plane-longitudinal resolution is 580 µm.

The final subsystem of the ID is the TRT covering the range of $|\eta| < 2.5$. The TRT consists of a straw tube detector of 73 layers interleaved with fibres in the barrel region and 160 layers with foils in the end-caps. The straws are filled with a Xenon/CO_2/O_2 gas mixture and they are used as drift chambers. Charged particles with $p_T > 0.5\,\text{GeV}$ and $|\eta| < 2.0$ will traverse at least 36 straws, except for the barrel-end-cap region ($0.8 < |\eta| < 1.0$), where such particles will pass through 22 straws. One expects seven to ten hits for electrons above energies of 2 GeV. This detector is designed to offer resolutions of 130 µm. Though the resolution is not comparable to the first layers, the great number of hits allows to measure particle momenta very precisely in a wide range [54].

3.3.2. Calorimeter

The calorimeter is composed, on the one hand, of the electromagnetic calorimeter (ECAL) to detect electrons and photons and, on the other hand, of a hadronic calorimeter (HCAL). The ECAL is composed of the barrel part, which covers $|\eta| < 1.475$, and the two end-caps, which cover the range $1.375 < |\eta| < 3.2$. This detector is a lead and high granularity liquid-argon (LAr) detector, arranged in accordion-shape around the beam axis, to cover the full azimuthal range ϕ. The incoming electron and photons shower in the lead plates and are measured with the LAr detectors. The cell-granularity varies in the range of $\Delta\eta \times \Delta\phi = 0.0031 \times 0.1$ and 0.1×0.1. Energy loss in the region $|\eta| < 1.8$ due to the ID is determined by a presampler, an active LAr layer.

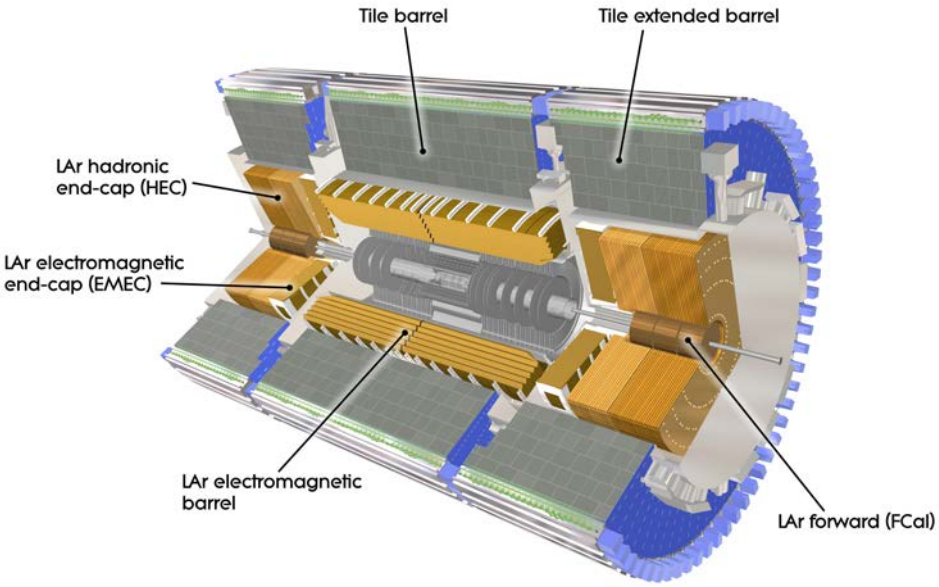

Figure 3.9.: The ATLAS calorimeter.

The HCAL uses two different techniques to absorb the hadrons. The tile calorimeter of the HCAL is a sampling calorimeter using steel as an absorber and scintillating tiles as the active material. It is placed directly behind the ECAL. The barrel region covers $|\eta| < 1.0$ and the extended barrels cover $0.8 < |\eta| < 1.7$. The hadronic end-cap calorimeter consists of two wheels and is situated behind the end-caps of the ECAL, sharing the same LAr cryostat. To avoid the drop of material density in the transition regions of the different detector subsystems, this end-cap calorimeter overlaps with the tile calorimeter and the forward calorimeter through the covering range of $1.5 < |\eta| < 3.2$. The wheels are made of copper plates with interleaved LAr gaps.

The forward calorimeter is integrated in the end-caps cryostat and is made of three modules. The first one is built of copper intended for the electromagnetic interacting particles followed by two modules made of tungsten, intended to provoke hadron showering. The active medium is LAr, too.

3.3.3. Muon system

Muons are the only charged particles which are not absorbed by the calorimeter. The muon spectrometer bends the tracks of muons with large superconducting aire-core toroid magnets. One can deduce the muon momentum from their measured deflection. Monitored drift tubes are installed for high precision measurements. Near the beam pipe, the radiation background would be too high for such detectors. Therefore, cathode strip chambers are used. Additional to this, resistive plate chambers in the barrel region and thin gap chambers in the end-caps are plugged. These detector types offer a lower precision for track reconstruction, but they have a fast readout, which predestine these detectors to be used as trigger-systems.

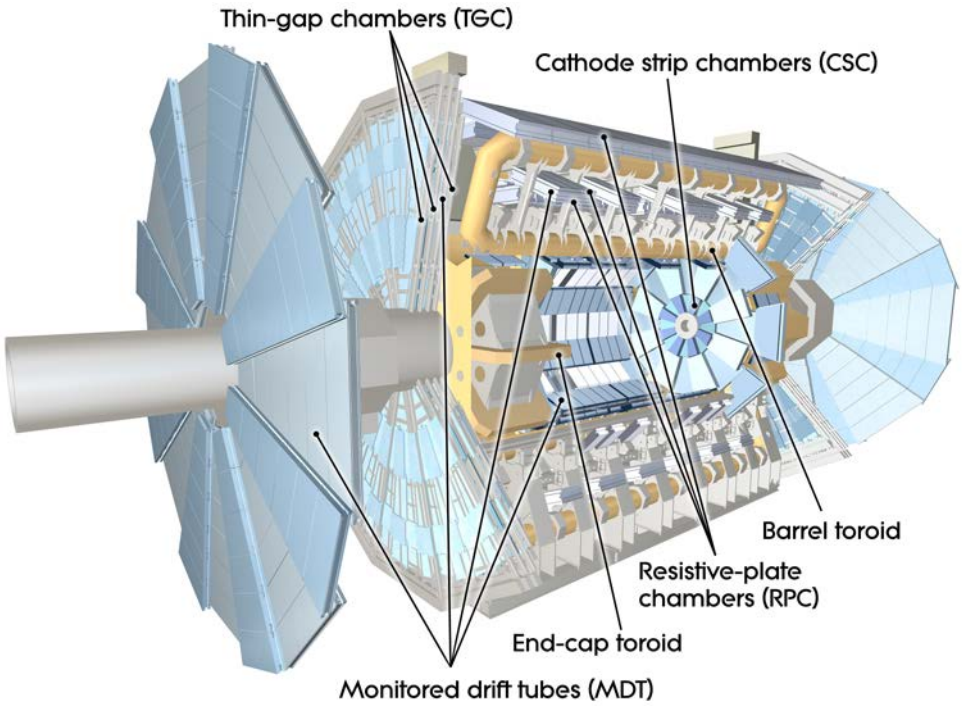

Figure 3.10.: The muon detection subsystem.

3.3.4. Trigger systems

As mentioned before, a major challenge is the distinction between interesting events, such as high-energy electrons or jets, and the vast background of soft QCD-interactions. It is impossible to retain all the information of the colliding proton beams, since the bunch spacing is 25 ns which corresponds to a collision rate of 40 MHz. The capacities of final storage is just up to trigger rates of $200 - 300$ Hz which leads to the need to reduce significantly the event rate. Therefore, a three-level trigger facility is accommodated by the ATLAS data acquisition system which filters interesting events increasing purity and decreasing rate.

- *Level 1*
  The first trigger level is a hardware-based trigger using reduced granularity information of the calorimeter and the muon system. It defines regions of interest (ROI) leading to detect potential muons, electrons/photons, hadrons or jets with high transverse momentum, p_T, or events of large missing transverse energy, $\not{E}_T$. At this stage, the trigger takes up to 2 µs to reach its decision and reduces the event rate down to ~100 kHz.

- *Level 2*
  In contrast to the level-1 trigger, the level-2 trigger works just with the ROIs defined at level-1 but with full-granularity information provided by all detectors including the inner detector. This trigger system uses processor farms and has an average latency up to 10 ms. The level-2 trigger reduces the event rate down to 1 kHz.

- *Level 3*
  The last trigger before the final storage is the Event Filter (EF) trigger. It collects the fragments of each passed event and applies offline selection criteria on the full-event data to discard the uninteresting events. The overall time consumed by the EF trigger selection executed by processor farms is approximately 1 s per event on a 1000 MIPS (Million Instructions Per Second) processor.

Between the different trigger-levels, the data has to be stored by buffer systems until the trigger can process the event. Only the events, which pass all three trigger-levels, are saved for later analysis [55, 56].

3.4. Event simulation

Monte Carlo (MC) methods are computational methods that use random numbers to model stochastic processes or to model deterministic processes which can be approximated by stochastic ones. These methods are used to describe problems of many coupled degrees and stochastic phenomena. Therefore, they are widely used in particle physics to create simulated events based on the known physics. Such produced events serve as basis of a comparison between data and theory.

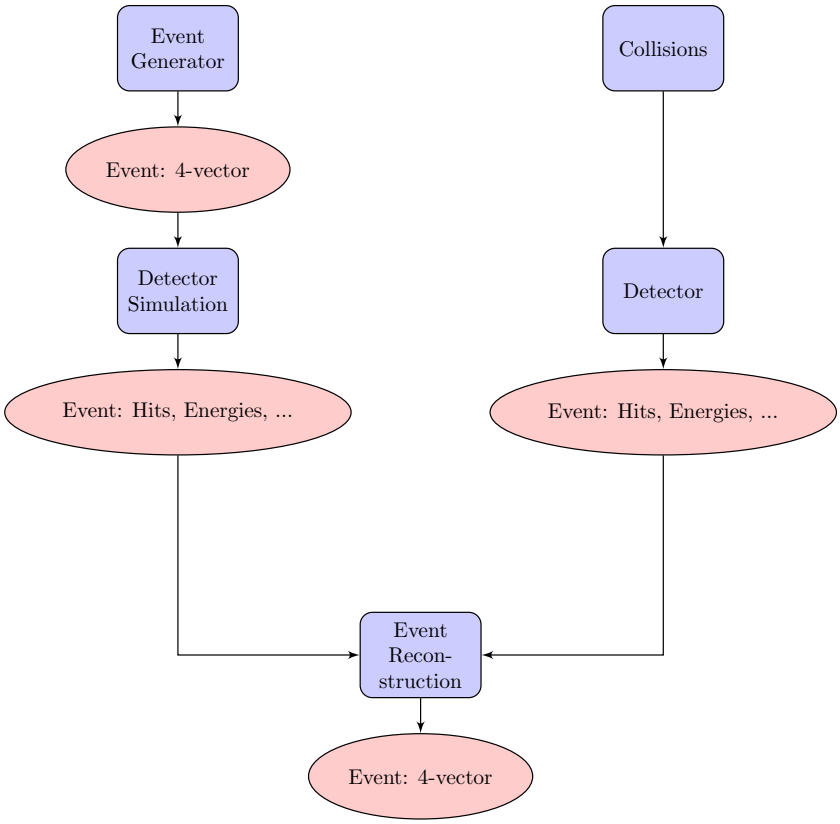

Figure 3.11.: Basic steps in simulation and data analysis.

The generation of such simulated events consists of several steps. As one can see in Figure 3.11, an event generator calculates the scattering process and it produces the four-vectors of their products, without considering the interaction of the produced particle with the environment. The detector response of the simulated events can be calculated by GEANT [57]. Afterwards, the same reconstruction algorithms as for the recorded events are used.

The generation, by the event generator, has to calculate different sequenced physical

processes. These are initial-state radiations, the hard scattering process, the decay of the particle, final state radiation and hadronisation and further decay. In this thesis, Pythia+Alpgen is mainly used.

Alpgen

Alpgen [58] is a tree-level matrix element calculator which produces events with a fixed number of partons in the final state for hadronic collisions. It describes the multi-partonic final states up to four partons without loop corrections, based on the exact evaluation of the leading-order QCD and electroweak Feynman diagrams. Alpgen does not provide any calculations of the hadronisation process, such that a further generator has to be used.

Pythia

Pythia [59] is a general-purpose event generator. It contains a list of hardcoded subprocesses, that can be switched on seperately. The generator simulates events at leading-order for up to three legs. Additionally, it can use the four-vectors generated by Alpgen. Beside the hard processes, Pythia simulates soft processes, initial and final state radiation, parton showering, multi parton interaction, beam remnants, and hadronisation processes [60].

4. Phenomenology

This chapter provides a basic description of the theoretical aspects which are mostly relevant to the subject of this study. These include the production and decay of the Higgs boson in the Standard Model and the Z gauge boson. Information about the tau lepton is also provided.

4.1. Electroweak precision measurements

The measurements of Higgs boson and Z boson masses and their production cross section are very important since they determine crucial parameters of the Standard model. All these measurements probe the consistency of the parameters as provided by the electroweak theory. As mentioned above, the presented gauge couplings in (2.27) - (2.30) between the quantities, which can be experimentally measured, are just valid at tree-level. Feynman calculations of higher order diagrams lead to a correction to these parameters, which end up in the effective parameters.

The described electroweak theory is probed in detail by the results of many collider experiments. A major contribution was provided by two e^+e^- colliders in the late eighties, the Stanford Linear Collider at SLAC in California and the circular Large Electron Positron collider at CERN in Geneva. These were the first colliders to reach the energy of the Z boson mass, which allowed precision measurements at the Z-production peak. Various measurements of asymmetries led to the extraction of the effective parameter of the electroweak model. Figure 4.1 shows the fit results to the data taken at LEP as a function of the Higgs mass assuming the Standard Model to be correct.

4.2. The Higgs particle

The Higgs mass was the only missing parameter to complete the electroweak theory as of the year 2012. High precision measurements of the effective parameters can give an estimation of the Higgs mass due to the dependency at higher order diagrams. This approach gives results with high uncertainties, since the corrections of the effective parameters de-

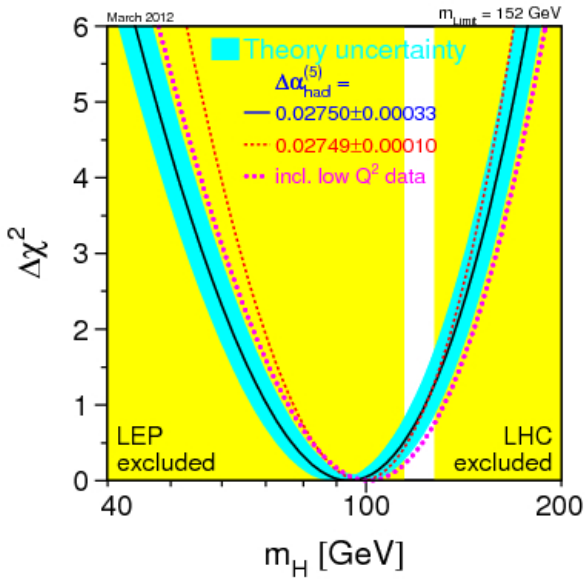

Figure 4.1.: Fit results of electroweak precision measurements performed at at LEP and by SLD, CDF, and DØ, as a function of the Higgs-boson mass [61].

pend only logarithmically on the Higgs mass. Apart from that, theoretical conditions do constrain the Higgs mass. The claim of perturbative unitarity [62, 63] and the triviality bound [64] give respectively upper bounds of the Higgs mass, as follows

$$\text{unitarity}: \; m_H \leq 870\,\text{GeV} \tag{4.1}$$

$$\text{trivality bound}: \; m_H \leq 640\,\text{GeV}. \tag{4.2}$$

On the other hand, the vacuum stability gives a lower bound on the Higgs mass. In the case of a cutoff value of $\Lambda_C \propto 10^3(10^{16})$ it leads to a lower bound of

$$m_H \geq 70(130)\,\text{GeV} \tag{4.3}$$

In addition to the measurements, direct Higgs searches have been performed by the experiments at the TEVATRON at FERMILAB. These searches resulted in the exclusion of Higgs with masses below 170 GeV (95 % CL) [65].

The combined results of the Higgs searches including the results of SLC, the TEVATRON, and LEP, suggests $m_H = 89^{+22}_{-18}\,\text{GeV}$ or $m_H < 127\,\text{GeV}$ at 90 % confidence level [66]. The combination of LEP data, taken near the Z resonance and at center-of-mass energies up to 209 GeV, resulted at a 95 % CL in a lower bound of 114.4 GeV [67].

4.2.1. Higgs production at the LHC

The Higgs particle couples to all massive particles, which lead to a broad spectrum of production and decay processes. The main production processes at proton-proton colliders are the gluon-gluon fusion (ggF), the vector boson fusion (VBF), the W and Z associated production (WH, ZH), and the $t\bar{t}$ associated production ($t\bar{t}H$) (Figure 4.2). The cross section summarized for a Higgs mass of $m_H = 125\,\text{GeV}$ in Table 4.1, depends in general on the mass of the Higgs boson and the center-of-mass energy of the collider. Nevertheless, the gluon-gluon fusion is all across the mass spectrum the dominant process. This leads at the same time to high theoretical uncertainties due to significant QCD corrections [68].

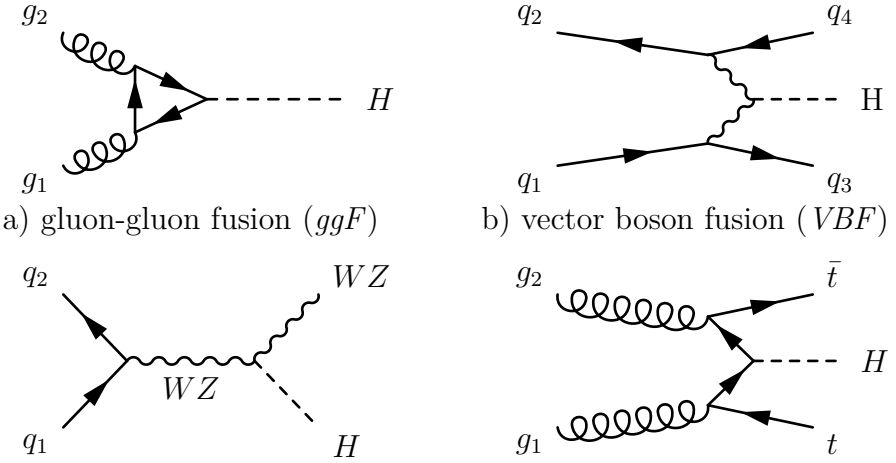

a) gluon-gluon fusion (ggF) b) vector boson fusion (VBF)

c) W and Z associated production (VH) d) the $t\bar{t}$ associated production ($t\bar{t}H$)

Figure 4.2.: Main production processes of the Higgs boson at the LHC.

Table 4.1.: Higgs production cross sections in pb for $m_H = 125\,\text{GeV}$ at different center-of-mass energies [68].

$\sqrt{s}$ [TeV]	ggF	VBF	WH	ZH	$t\bar{t}H$	total
7	$15.1^{+15\%}_{-15\%}$	$1.22^{+3\%}_{-2\%}$	$0.58^{+4\%}_{-4\%}$	$0.33^{+6\%}_{-6\%}$	$0.09^{+12\%}_{-18\%}$	17.4
8	$19.3^{+15\%}_{-15\%}$	$1.58^{+3\%}_{-2\%}$	$0.70^{+4\%}_{-5\%}$	$0.41^{+6\%}_{-6\%}$	$0.13^{+12\%}_{-18\%}$	22.1
14	$49.8^{+20\%}_{-15\%}$	$4.18^{+3\%}_{-3\%}$	$1.50^{+4\%}_{-4\%}$	$0.88^{+6\%}_{-5\%}$	$0.61^{+15\%}_{-28\%}$	57.0

4.2.2. The decay of the Higgs boson

In planning a search for a Higgs boson, the branching ratios of the different decay modes have to be considered. Figure 4.3 shows the Higgs branching ratio as a function of its

mass. As one can see, the dominant processes at a Higgs mass as $m_H = 125\,\text{GeV}$ are $H \to b\bar{b}$ and $H \to WW^*$, followed by $H \to gg$, $H \to \tau^+\tau^-$, $H \to c\bar{c}$, and $H \to ZZ^*$. The Higgs decays into $H \to \gamma\gamma$, $H \to Z\gamma$, and $H \to \mu^-\mu^+$ follow with much smaller rates. Since the Higgs boson couples only to massive particles, the decay into massless particles or $H \to \gamma Z$ has an intermediate loop of vector bosons or fermions which couples to the Higgs boson.

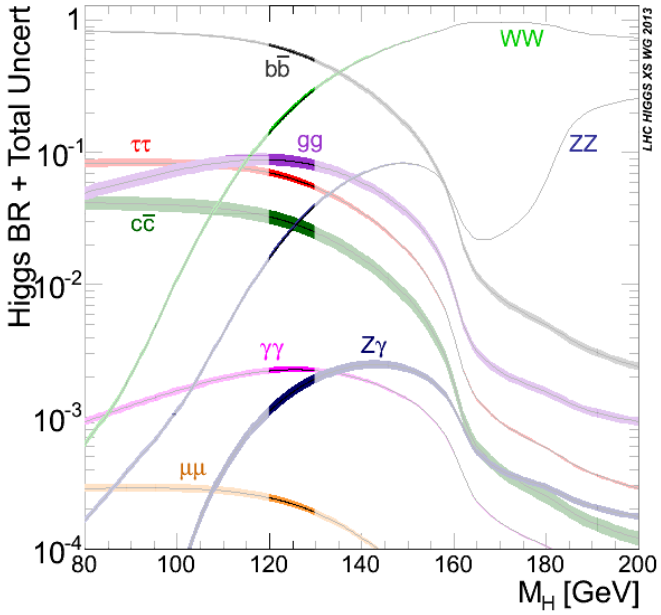

Figure 4.3.: Decay branching ratios of the Standard Model Higgs boson [69].

The Higgs discovery at the ATLAS experiment was based on the decay into $\gamma\gamma$, ZZ, and WW, since the fermionic decay channels were not yet sensitive [1]. In spite of low statistics, the decay channels $\gamma\gamma$ and ZZ offer the best way to extract the mass of the Higgs boson. Due to a very clear signature and the absence of any neutrinos in the final states, a very good resolution can be achieved.

Apparently, the Higgs decay modes leading to the Higgs discovery consist almost only of the coupling between the Higgs boson to other bosons. Indeed, the $H \to \gamma\gamma$ process is mainly based on W^+W^- and $t\bar{t}$ loops. Furthermore, there are contributions of loop diagrams of all other charged particles. Due to the Higgs coupling proportional to the particle's mass, the heaviest charged particles play the dominant role. Hence, this process is a good indicator for new physics beyond the Standard Model [70]. But this channel does not offer a way to directly detect the fermionic Higgs coupling.

4.2.3. Further Higgs studies

One of the unobserved properties of the Higgs boson, which is indeed predicted by the Standard Model, is the direct coupling of the Higgs boson to fermions. At the time of the Higgs discovery, the analyzed data of 4.8(5.1) fb^{-1} at 7 TeV and 5.9(5.3) fb^{-1} at 8 TeV by ATLAS (CMS) did not provide a significant contribution of the dominant fermionic Higgs decays $H \to b\bar{b}$ and $H \to \tau\tau$ [1, 2]. The Higgs decay into a b-quark pair has the largest branching ratio of 57.7 % [71], but the background of QCD multijet production is too high and it suffers from high theoretical uncertainties. The most promising decay channel to fermions is the decay into a τ-pair. It is the next dominant fermionic decay channel with a branching ratio of 6.32 % [71]. Meanwhile, both collaborations, ATLAS and CMS, announce first evidence of $h \to \tau\tau$ [3, 4].

> "The ATLAS experiment released preliminary results on 26 Nov 2013 that show evidence, with a significance of 4.1 standard deviations that the Higgs boson decays to two taus, which are fermions." from 'Evidence for Higgs Boson decays to the $\tau\tau$ Final State with the ATLAS Detector' [3]

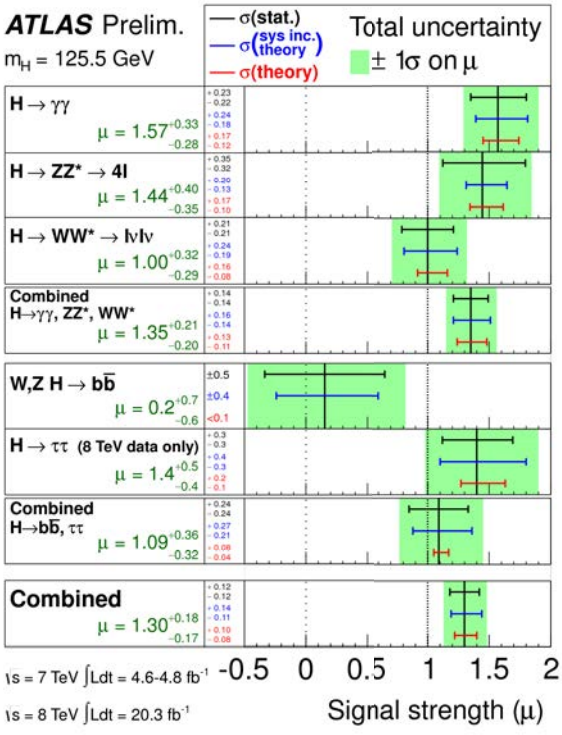

Figure 4.4.: The measured signal strengths for a Higgs boson of mass $m_H = 125.5\,\text{GeV}$, normalised to the SM expectations, for the individual final states and various combinations [72].

Figure 4.4 shows the signal strength of the different decay channels of the tau-pairs. The analysis is divided into the $\tau_{lep}\tau_{lep}$, $\tau_{lep}\tau_{had}$, and $\tau_{had}\tau_{had}$ channels. The subscript indicates, whether the tau decays leptonically or hadronically. The statistical uncertainty is a contribution to the total uncertainty and will be be reduced by the following run of the LHC. Additionally, the systematical error has the same order as the statistical error, such that even without further data-taking the precision of this measurement could be increased by reducing systematic uncertainties. One of the most significant systematic uncertainties comes from the normalization of the process $Z \to ll$ and the description of the final-state particles. Since $Z \to \tau\tau$ is an irreducible background, this process has to be well known. Therefore, the improvement of the description and understanding of this process is one way to enhance the significance of the result.

4.3. The Z boson

4.3.1. Prediction & observation of the Z boson

The Z boson played a significant role establishing the GWS-model. The model predicted the existence of neutral currents and even provided a precise estimation of the Z mass. The first evidence for the existence of the Z boson was provided by the observation of neutral currents at the Gargamelle experiment in 1974 [73]. At that time, only the indirect confirmation of the Z boson was possible, since there was no particle accelerator to reach a sufficiently large center-of-mass energy to produce a Z boson. Only the reconstruction of the Super Proton Synchrotron (SPS) at CERN into a proton-antiproton collider allowed the Z boson production. In 1983 the UA1 experiment confirmed the existence of the Z boson in the expected mass range [38]. Later, more detailed measurements were performed at the Z resonance by electron-positron colliders. The data taken at the colliders LEP and SLC consists of 17 million and 600 thousand decays [61]. Today's best fit of the Z mass m_Z and of the total width Γ_Z are [39]

$$m_Z = (91.1876 \pm 0.0021)\,\text{GeV} \tag{4.4}$$

$$\Gamma_Z = (2.4952 \pm 0.0023)\,\text{GeV}\,. \tag{4.5}$$

4.3.2. Production & decay of the Z boson

At hadron colliders, the main production process of Z bosons is at tree-level the Drell-Yan process as shown in Figure 4.5. Quark-antiquark pairs annihilate and produce Z/γ bosons which subsequently decay into fermion pairs. The final state is the same. Therefore, at

tree-level, the resulting cross section is the result of an interference of two Feynman diagrams.

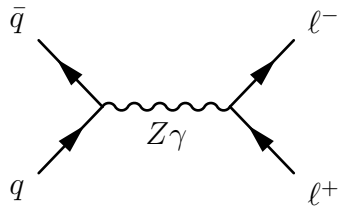

Figure 4.5.: Z boson production at tree-level.

The inclusive production channels of Z bosons at NLO and NNLO contain additionally radiated gluons or scattered quarks, such that the produced Z boson can be accompanied by a number of jets. Feynman diagrams of NLO QCD, shown in Figure 4.6, refer to Z production with one jet.

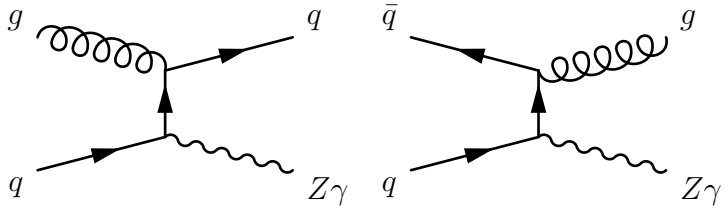

Figure 4.6.: Next-to-leading order Feynman graphs of Z boson production.

In case of hadron colliders, one cannot calculate the cross section of Z boson production only by evaluating the Feynman diagrams at the collider's center-of-mass energy. As described in Section 3.2.1, the partons within the hadron carry just a fraction of the momentum, parameterized by PDFs. Therefore, the cross section of Z production at hadron level $\sigma_{pp\to Z}$ is the result of the convolution of the cross section at parton level $\sigma_{ij\to Z}$ of the scattered partons ij and the PDFs $f(x,\mu)$, given as follows

$$\sigma_{pp\to Z} = \sum_{ij} \int dx_1 dx_2 f_i(x_1,\mu) f_j(x_2,\mu) \sigma_{ij\to Z}(x_1,x_2,s,\alpha_s(\mu),\mu)\,. \tag{4.6}$$

Figure 4.7 shows the measured cross section of the Drell-Yan process in comparison to the theoretical expectation of NNLO perturbative QCD calculations. The experimental results match within the error bands with the theoretical expectation.

The Z boson couples via a V-A structured vertex to all particles except for photons and gluons. Therefore, it decays in any fermion-antifermion pair which is energetically

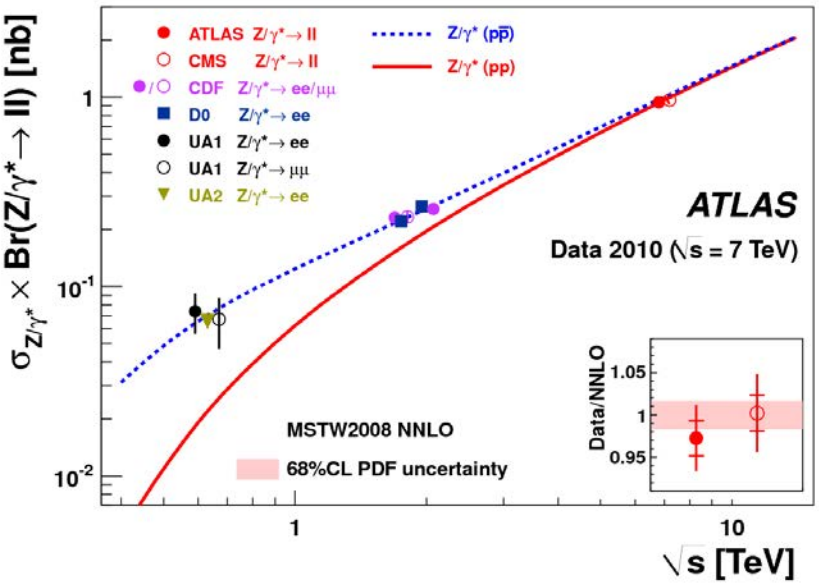

Figure 4.7.: Measured and calculated cross section of the Drell-Yan process [74].

possible. The total decay with of the Z boson is at tree-level

$$\Gamma = \frac{g_Z^2 m_Z c^2}{48\pi\hbar} \sum_f (|c_A^f|^2 + |c_V^f|^2)\,, \tag{4.7}$$

where the summation runs over all fermions f and c_A^f, c_V^f are the axial and vector coupling constants defined by

$$c_V = T_3 - 2Q \sin^2 \Theta_W \tag{4.8}$$

$$c_A = T_3\,. \tag{4.9}$$

The mean life time of the Z boson is of the order $\mathcal{O}(10^{-25})$ s. The branching ratios of the different decay modes are summarized in Table 4.2.

Table 4.2.: Branching ratios of Z boson decay [39].

Mode	**Theoretical fraction** Γ_i/Γ	**Experimental fraction**
e^-, μ^-, τ^-	3.44 %	(3.3658 ± 0.0023) %
ν_e, ν_μ, ν_τ	6.85 %	(20.00 ± 0.06) %
hadrons	69.13 %	(69.91 ± 0.06) %

4.4. The τ-lepton

As described above, the τ-lepton plays a major role in measuring the fermionic Higgs coupling. It is the third lepton of the Standard Model and it has the same quantum numbers as the two lighter charged leptons, electron and muon. Consequently, it is a spin-$\frac{1}{2}$-particle with weak isospin $I_3 = -\frac{1}{2}$ and the electric charge -1. Its mass m_τ and lifetime τ_τ are [39]

$$m_\tau = (1776.82 \pm 0.16)\,\text{MeV} \tag{4.10}$$

$$\tau_\tau = (290.6 \pm 1.0) \times 10^{-15}\,\text{s}\,. \tag{4.11}$$

Similar to the muon, the tau lepton is not a stable particle, since there are possible decay products, which are lighter than the mother particle. Nevertheless, the tau-lepton expands the range of the possible decay modes. In contrast to the muon mass of $m_\mu \approx 105.6\,\text{MeV}$ [39], the tau mass is greater than the mass of pions $m_\pi \approx 139.6\,\text{MeV}$ [39]. Therefore τ leptons can decay into several hadronic decay channels beside the leptonic channels.

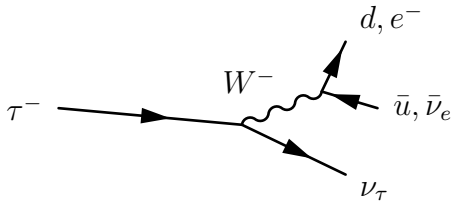

Figure 4.8.: The τ-decay mediated by the W boson into quarks or leptons.

The decay of the tau leptons occurs via a weak interaction and it is mediated by the W boson depicted in Figure 4.8. The decays are usually grouped into the lepton decay channels $\tau^- \to \ell^- \bar{\nu}_\ell \nu_\tau$ and the hadron decay channels $\tau^- \to \text{hadrons} + \nu_\tau$. The lepton channels consist of the two equal decays into an electron or a muon plus neutrinos. The hadron channel exhibits a wider multiplicity of processes. The conservation of electric charge leads to decays with an odd number of charged particles plus neutral particles. The hadronic decays of a tau into one negative charged particle with additional neutral particles is named *1 prong + X* and the decay into three charged particles (two negative and one positive) with neutral particles is named *3 prong + X*. Higher track multiplicities are highly suppressed. Table 4.3 offers an overview of the dominant decay channels and their branching ratios.

Table 4.3.: Branching ratios of dominant τ decay channels [75].

Decay	**Branching ratio** [%]
$e^-\bar{\nu}_e\nu_\tau$	17.85 ± 0.05
$\mu^-\bar{\nu}_\mu\nu_\tau$	17.36 ± 0.05
$\pi^-\nu_\tau$	10.91 ± 0.07
$\pi^-\pi^0\nu_\tau$	25.51 ± 0.09
$\pi^-2\pi^0\nu_\tau$	9.29 ± 0.11
$\pi^-\pi^+\pi^-\nu_\tau$	9.00 ± 0.06
$\pi^-\pi^+\pi^-\pi^0\nu_\tau$	2.70 ± 0.08

4.4.1. Discovery of the tau lepton

The first signs for a third member in the lepton family were detected by Martin Lewis Perl et al. at SLAC [76]. The LBL detector collaboration recorded events from the SPEAR collider.

The LBL detector recorded a significant number of $e^+e^- \to \mu^+e^-$ accompanied by at least two undetected particles. The interpretation of these events were inexplicable at that time in the scope of the known processes. Therefore, a new particle was postulated in 1975. The estimated mass range of this new particle was between 1.6 and 2.0 GeV.

This interpretation was not immediately accepted and other interpretation, such as pion decays were proposed or the measurement itself was mistrusted [77]. As opposed to the quark mixing, there was no theoretical need to impose a third lepton.

Finally, the measurement of the $\tau_{lep}\tau_{had}$ channel supported the theory of a heavy lepton. The measurement of the so-called anomalous muon production $e^+e^- \to \mu^- + hadrons$ consolidated the interpretation of these events as tau-decays in 1977 [78, 79]. Nevertheless, it took until the end of 1978 to establish the tau lepton [80].

The lifetime of taus is measured by the reconstruction of secondary vertices. Its value in Equation (4.11) leads to a decay length of $L = 87\,\mu m$. In the case of the LHC, taus decay already in the beam pipe, but high resolutions near to the intersection point allow the extrapolation of charged tracks to the secondary vertex of the tau decay.

5. Analysis

In this thesis, the measurement of the $Z \to \tau\tau$ cross section of the lepton-hadron channel is presented. The analysis is based on the data set of an integrated luminosity of $\int \mathcal{L}\,\mathrm{d}t = 20.3\,\mathrm{fb}^{-1}$ recorded at a proton-proton center-of-mass energy of $\sqrt{s} = 8\,\mathrm{TeV}$ with the ATLAS detector at the LHC.

5.1. Selection of $Z \to \tau_{\mathrm{lep}}\tau_{\mathrm{had}}$ events

$Z \to \tau\tau$ events in the semileptonic decay channel are typically characterized by the production of a highly collimated jet coming from the hadronically decaying tau and one isolated lepton arising from the leptonic tau decay. The tau jet of the former decay is almost always composed of the odd number of charged hadrons and neutral pions. In addition to the tau jet and the lepton of the tau decay, neutrinos are produced which are experimentally undetectable, giving rise to the missing transverse momentum in the event.

In summary, the measurement of the $Z \to \tau_{\mathrm{lep}}\tau_{\mathrm{had}}$ cross section is based upon the reconstruction of various objects: jets, τ candidates, muons, electrons, and the missing transverse momentum.

5.1.1. Object definitions

Muon candidate

The reconstruction of a muon candidate is based on the association of a muon spectrometer track with a track of the inner detector. The calculation of the transverse momentum of the muon candidate is a statistical combination of these two tracks taking the energy loss in the calorimeter into account [81, 82]. The transverse momentum of a *preselected muon candidate* has to be larger than 10 GeV and the tracks have to lie in the pseudorapity region of $|\eta| < 2.5$. Furthermore, the candidate has to pass the 'loose' identification criteria and additional quality requirements on the track quality. The number of hits in the pixel detector has to be greater than zero, the number of hits in the SCT has to be

greater than four and the sum of holes of the tracks in these detectors has to be smaller than three. If the track lies in the region $0.1 < |\eta| < 1.9$, the number of hits in the TRT has to be greater than 5 from which at most 90 % are allowed to be outliers. In addition, the longitudinal impact parameter D_0 of the candidate has to be smaller than 10 mm to differentiate it from cosmic muons.

The requirements of a *selected muon candidate* asks for a transverse momentum of $p_T > 17\,\text{GeV}$. Furthermore, the matching of tracks in the ID and the muon spectrometer is obligatory.

Electron candidate

Electron candidates are associated to clusters of deposited energy in the EM calorimeter matched to tracks of the inner detector. A *preselected electron candidate* has to have a transverse momentum of at least 15 GeV and it has to lie within $|\eta| < 2.47$. In addition, a candidate has to fullfill the 'loose' identification criteria [83]. Within the crack region of the $1.37 < |\eta| < 1.52$, the 'medium' identification criteria is asked for. Finally, a *selected electron candidate* has to fullfill the 'tight' identification criteria and the transverse momentum of the lepton has to be greater than 20 GeV.

Tau candidates

In the context of this analysis, tau refers to a hadronically decaying tau. The reconstruction of tau candidates is based on jets reconstructed with the anti-k_t algorithm [84] within a cone of $\Delta R = 0.4$ and $p_T > 15\,\text{GeV}$. Quality criteria to distinguish between jets from tau decay and other sources are the crucial ingredient of the tau candidate definition.

First of all, one asks for one or three tracks, referring to the odd number of charged decay products, named 1-/3-prong. Additionally, the electric charge of the reconstructed jet has to be plus or minus one, $p_T > 20\,\text{GeV}$ and $|\eta| < 2.47(2.5)$ in case of one (three) prong(s). Then, the *Boosted Decision Tree* (BDT), which is trained to distinguish between jets from taus and other sources as described in [85], has to rate this candidate at least with 'medium' tag. The tau identification criterion represents a signal efficiency of approximately 45 %. To reject electrons, which can fake tau candidates, an additional BDT discriminant is applied. For one and three tracks, a separately trained BDT for the identification is applied.

Missing transverse momentum

The missing transverse momentum is defined by the vectorial sum of the deposited energy clusters in the calorimeter and the reconstructed muon tracks [86], as follows

$$\not{E}_T = \not{E}_T^{\text{calorimeter}} + \not{E}_T^{\text{muon}} - \not{E}_T^{\text{energy loss}} . \tag{5.1}$$

The first term describes the energy deposits within the calorimeter and it is composed of a topological cluster. The second term is based on the momenta of the muons, since they deposit just a part of their energy. The last term is a correction term to take into account the energy loss of the muons in the detector.

Lepton isolation

The leptons arising from tau decays are typically isolated. The isolation of a lepton can be quantified by the ratio of the deposited energy around the lepton track and the transverse momentum of the related lepton. In the context of this analysis, two isolation parameters are used. One uses the energy of tracks around the lepton track within a cone of $\Delta R = 0.4$, which is constrained to 4% of its own transverse energy,

$$I_{p_T}^{0.4}/p_T < 0.04 . \tag{5.2}$$

Since this isolation criterion is based on track information, this cut is only sensitive for charged particles. Figure 5.1 shows the distribution of the isolation variable within the preselection (see Figure 5.9) just before the application of the cut on the isolation. The plot contains only the contribution of the available Monte Carlo samples, since the estimation of the QCD multijet background is based on a data driven method, which makes use of the inverse of the lepton isolation. Therefore, the discrepancy of the data and the simulation can mostly be traced back to the undescribed QCD multijet background. The track based isolation distribution shows already a clear isolation of the processes which produce charged leptons. Nevertheless, the cut of Equation 5.2 allows to get a higher purity of $Z \to \tau\tau$ signal events, since contributions of W+jets and QCD background can be rejected.

In contrast to the track based isolation, the isolation within the calorimeter defined as

$$I_{E_T}^{0.2}/p_T < 0.04 \tag{5.3}$$

takes neutral particles into account as well. Due to the shower shape of the particles in

the calorimeter, the detected particles have a much larger spread and hence a smaller isolation cone of $\Delta R = 0.2$ in contrast to the track isolation must be required. Figure 5.2 shows this isolation variable for electrons and muons. As one can see, the main contribution above the cut of Equation 5.3 is due to (unclassified) QCD multijet events.

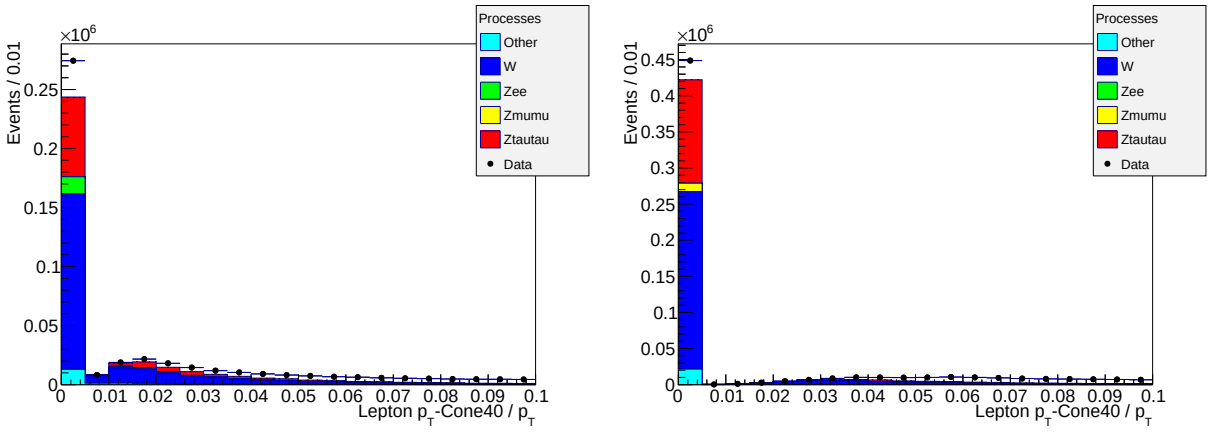

a) Electron channel b) Muon channel

Figure 5.1.: $I^{0.4}_{p_T}/p_T$: The summed track energy measured in a cone of $\Delta R = 0.4$ around the lepton track relative to the transverse momentum of the lepton $I^{0.4}_{p_T}/p_T$, used as an isolation variable to select electron and muon candidates. The coloured stacked histogram describes the expected composition of the signal region given by MC simulations at preselection stage before the isolation cut (see Figure 5.9). The black dots represent the number of events at this cut stage measured by the ATLAS detector for an integrated luminosity of $\int \mathcal{L}\,dt = 20.3\,\mathrm{fb}^{-1}$. Its vertical error bars describe the statistical uncertainties of the data.

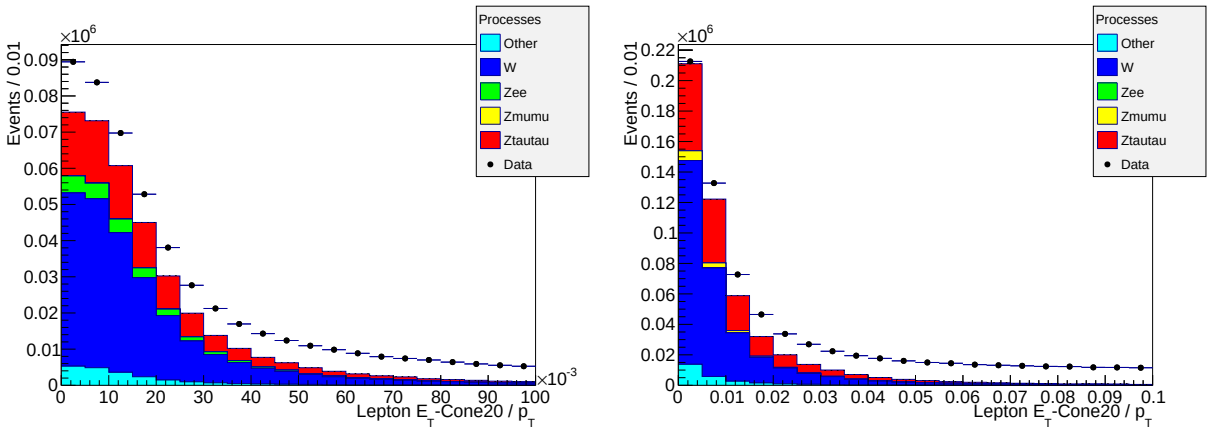

a) Electron channel b) Muon channel

Figure 5.2.: $I^{0.2}_{E_T}/p_T$: The deposited energy in the calorimeter in a cone of $\Delta R = 0.2$ around the lepton track relative to the transverse momentum of the lepton $I^{0.2}_{E_T}/p_T$. For more information, see Figure 5.1.

5.1.2. Background

To determine the purity of the $Z \to \tau_{\text{lep}}\tau_{\text{had}}$ events in the signal region, one has to estimate the background contributions to it. The major contributions to the signal comes from $Z \to \ell\ell$ decays ($\ell = e, \mu$), $W \to \ell\nu + jets$ and QCD multijet productions. Apart from the last contribution, all backgrounds are estimated with MC simulations. A detailed list of the used MC samples is in Appendix A. The estimation of the QCD jet background is calculated with a data-driven method.

Electroweak backgrounds

Z decays into charged leptons The decay of $Z \to \ell\ell$ with $\ell = e, \mu$ constitutes an important background of the $Z \to \tau\tau$ decay. Within the scope of the lepton-hadron decay channel, these background contributions are reducible. One can reject all completely measured and correctly reconstructed $Z \to \ell\ell$ by imposing a dilepton veto. Hence, only incomplete or misleading reconstructions can fake $Z \to \tau_{\text{lep}}\tau_{\text{had}}$ events. reconstruction and The identification of muons is rather unambiguous, so that $Z \to \mu\mu$ faking $Z \to \tau_{\text{lep}}\tau_{\text{had}}$ events are mostly due to a jet faking a hadronic tau and a muon, which is lost in the beam pipe. These events contribute only lightly to $Z \to \tau_{\text{lep}}\tau_{\text{had}}$. Indeed, the $Z \to ee$ decay has a larger impact. Electrons do not have such a clear signature and thus can be easily identified as a hadronic tau. Therefore, a dedicated BDT to distinguish between electrons and taus is commonly used (see Section 5.1.1).

W+jets The W+jets background is the major background after having applied the cuts based on the event topology. This process can mimic a $Z \to \tau_{\text{lep}}\tau_{\text{had}}$ event identified by the presence of exactly one lepton and one hadronic tau mostly in two different ways. Firstly, a leptonic W decay can provide the muon or the electron of the signal region and a jet can be misidentified as the hadronic tau. Secondly, the W decays into a hadronic tau and one of the accompanying jets fakes an electron. The suppression of these events stands on efficient object reconstruction, but also on kinematic cuts. The latter are based on the neutrinos, which show up as missing transverse energy. A more detailed description of these cuts is given in Section 5.1.3.

Other Besides the described electroweak background contributions, there are several other backgrounds which have only a slight impact on the signal region. Those processes

will be summarized as 'Other' in the figures. Events of these processes contribute only with particular decay channels in case of lost particles in the beam pipe or misidentified objects. These include the *top* quark production. In particular, the pair-production such as the single top production can bring up W as intermediate states which can contribute to the signal region as described in the previous paragraph. The cross section of $t\bar{t}$ at $\sqrt{s} = 8\,\text{TeV}$ is $241.4 \pm 8.5\,\text{pb}$ [87] and the associated production of single top quarks with W boson is $25.0 \pm 4.7\,\text{pb}$ [88]. Thus one does not expect a significant amount of background events faking signal events compared to the cross section of the inclusive W (Z) production of the (charged) lepton decay channel of ~11 nb (~1 nb) [89]. Likewise, one does not expect significant contributions of diboson production, WW, ZZ, ZW, whose total production cross section is of the order $\mathcal{O}(10)\,\text{pb}$ at $\sqrt{s} = 8\,\text{TeV}$ [90, 91]. The Higgs decay $H \to \tau\tau$ is an irreducible background. However, its cross section is of the order $\mathcal{O}(1)\,\text{pb}$ [68, 71] and thus cannot considerably affect the results. Nevertheless, these processes are included into the analysis for completeness and to improve the validity of the results.

QCD background

QCD multijet events can mimic $Z \to \tau_{\text{lep}}\tau_{\text{had}}$ decays only in case of incorrectly identified jets. Jets can be misleadingly identified as leptons as well as hadronic taus. Therefore, dedicated tuning of BDT algorithm is needed for tau identification, especially in hadronic environments. Additionally, the theoretical description of QCD suffers from big uncertainties [92]. Therefore, it is reasonable to use data-driven methods to estimate the contribution of this background. One data-driven approach to build the fake model is the template method, from which the shape and the normalization can be deduced using different control regions. The description and the results of further studies to validate this method are given in Section 5.2.

5.1.3. Event selection

The event topology of one semileptonic $Z \to \tau\tau$ decay offers selection criteria to create a signal region with high purity. The semileptonic channel is usually characterized by one isolated lepton. This lepton triggered a single lepton trigger (SLT) or a combined lepton tau trigger (LTT) and passed the isolation criteria. In addition, impacts of the dilepton channel of the $Z \to \tau\tau$ decay and the decays $Z \to \ell\ell$ with $\ell = \mu, e$ are reduced by imposing a dilepton-veto, the requirement of just one reconstructed lepton per event.

The identification of a hadronic tau is required. To respect the electric neutrality of

the Z boson, only events with different signs of the electric charge of leading τ_{had} and lepton are accepted. Since the aim is to measure the inclusive $Z \to \tau_{\text{lep}}\tau_{\text{had}}$ cross section, additional jets are allowed in the selected events.

Cuts of CommonNtuples

Apart from the mentioned constraints due to the event topology, one can apply several cuts to enhance the quality and purity of the signal region. For searches of the lepton-hadron channel of the $Z \to \tau\tau$ decay, the data format CommonNtuples is processed and provided by the Higgs working group. These are preskimmed derived physics data (D3PD) of the original tau D3PD. Aside from a preselection, the recommended corrections on the reconstructed 4-momenta are applied. The default selection of CommonNtuples is presented in the next paragraphs.

GoodRunList The selection of the CommonNtuple is intended to reject events due to different objectives. First, the general selection rejects events, which do not comply with the commonly used quality criteria of data. Then, a more particular selection is aimed to narrow down the data to the relevant parts. This filtering is given through the *GoodRunList* of the ATLAS Data Quality System. It offers a list in which luminosity blocks of the data are in accordance with the requirements on beam quality and data quality.

Trigger Data events are further filtered by using triggers. Respecting the data taking procedure, as described in Section 3.3.4, one has to consider well defined triggers. The signal region is determined by the presence of a lepton and a hadronic tau. So, two SLT, respectively one per lepton channel and two LTT are used:

- `EF_e24vhi_medium1`
  A single electron trigger with a threshold $E_T > 24\,\text{GeV}$ asking for medium selection criteria. The tag `vhi` describes certain selection criteria at the first trigger stage L1. It passed a variable η threshold (`v`), a hadronic leakage cut (`h`) and isolation criteria (`i`).

- `EF_tau20Ti_medium1_e18v_medium1`
  A combined tau-electron trigger: It comprises a triggered isolated (`i`) tau with $E_T > 20\,\text{GeV}$, passed an electromagnetic cluster threshold (`T`), which fulfills 'medium' selection criteria and an electron with $E_T > 18\,\text{GeV}$ as above without the isolation criterion.

- `EF_mu24i_tight`
  A muon trigger which tags isolated muons with $p_T > 24\,\text{GeV}$ passing further 'tight' selection criteria.

- `EF_tau20_medium1_mu15`
  A combined tau-muon trigger, which selects medium τ candidate with $p_T > 20\,\text{GeV}$ and muons with $p_T > 15\,\text{GeV}$.

Depending on the fired trigger, the event is categorized as an 'electron event' or a 'muon event'. If this classification is ambiguous, the event will be rejected.

Event cleaning After this first and rough selection of events, several additional selections are imposed. Since the Z+jets production is an inelastic scattering process, the recorded event has to describe a hard scattering event. An *event cleaning* is applied to reduce the impact of pile-up events and elastic scattering. It implies, that only events with at least one primary vertex are considered. To differentiate between vertices coming from hard scattering or elastic scattering, one uses the number of tracks belonging to the considered vertex. The event cleaning of the CommonNtuple asks for at least four tracks.

Overlap Removal To ensure the quality of reconstructed objects, an *overlap removal* of different selected objects is applied. An overlap of two objects o_1 and o_2 is given, if the distance $\Delta R(o_1, o_2)$ is smaller than 0.2. Preselected electrons will be unselected, if they overlap with selected muons. Hadronic taus are unselected in case of an overlap with a preselected lepton. The latter overlap removal uses a looser preselection of muons. These looser criteria comprehend a loose identification with $p_T > 2\,\text{GeV}$ without the described muon quality criteria in Section 5.1.1.

Dilepton veto In respect to the lepton-hadron channel, a *dilepton veto* is applied. This implies, that the electron (muon) channel allows only one preselected electron (muon). The CommonNtuple likewise provides a control region to the dilepton veto. It includes events with just two isolated[1] leptons of the same flavour of different charge and an invariant dilepton mass between 61 GeV and 121 GeV.

Final selection Finally to respect the event topology, only events with exact one selected lepton and one selected tau are dumped into the CommonNtuples. The flavour of the selected lepton offers the categorization of this events. The final classification of

[1] Analogue to the definition of the isolation criteria in Section 5.1.1 with an energy fraction below 0.6.

events into muon or electron and SLT or LTT by the CommonNtuple is based on further kinematic selections, which are described in the following paragraph.

The signal region

Differentiation of the lepton-hadron channel The semileptonic $Z \to \tau\tau$ decay can be split into the following four channels. The differentiation on truth level occurs based on the lepton flavour. The tau decay can yield an electron (el-channel) or a muon (mu-channel). On reconstruction level, there are respectively two possibilities for the two lepton channels to be identified: The SLT and the LTT. Since the event selection in respect of the triggers of the same flavour is not disjunct, one imposes further selection criteria to create orthogonal channels. This simplifies the combination of later results of different channels.

Table 5.1.: Cuts on the kinematics of tau and lepton to guarantee orthogonal signal regions for the SLT and LTT channel.

	electron	**muon**
SLT	$p_T^e > 25\,\text{GeV}$	$p_T^\mu > 22\,\text{GeV}$
	$p_T^\tau > 20\,\text{GeV}$	$p_T^\tau > 20\,\text{GeV}$
LTT	$17\,\text{GeV} < p_T^e < 25\,\text{GeV}$	$17\,\text{GeV} < p_T^\mu < 22\,\text{GeV}$
	$p_T^\tau > 25\,\text{GeV}$	$p_T^\tau > 25\,\text{GeV}$

One asks for unambiguousness of the lepton family by rejecting events with an overlap of the electron and muon trigger. To separate the LTT and SLT channel, the kinematic cuts of Table 5.1 are imposed. Figure 5.3 shows the distributions of the muon transverse momentum p_T^μ of the SLT and LTT channel right after the preselection. The Figure 5.4 presents the results of the electron channel. The last bin of the distribution of the SLT channels contains additionally the overflow events with $p_T^\ell > 110\,\text{GeV}$. Already after the preselection, the LTT channel is signal dominated. The most dominant background contributions are $W \to \ell\nu$ and QCD multijet events. Indeed, the SLT channels are in both cases dominated by the W+jets background, followed by the $Z \to \tau\tau$ signal and contributions of QCD and $Z \to \ell\ell$. Independent of the trigger channels, the muon channels are much purer than the electron ones due to better muon identification skills of the Atlas detector.

The discrimination of the SLT and LTT channel had been envisaged, such that all results were produced separately for the four channels. Finally, the analysis stopped before any particular dealing of the SLT and LLT channel. Therefore, the SLT and LTT

channel are merged from now on in this analysis. The further event selection is for all channels identical. It is mainly designed to reduce the dominant W+jets background to get a purer signal selection.

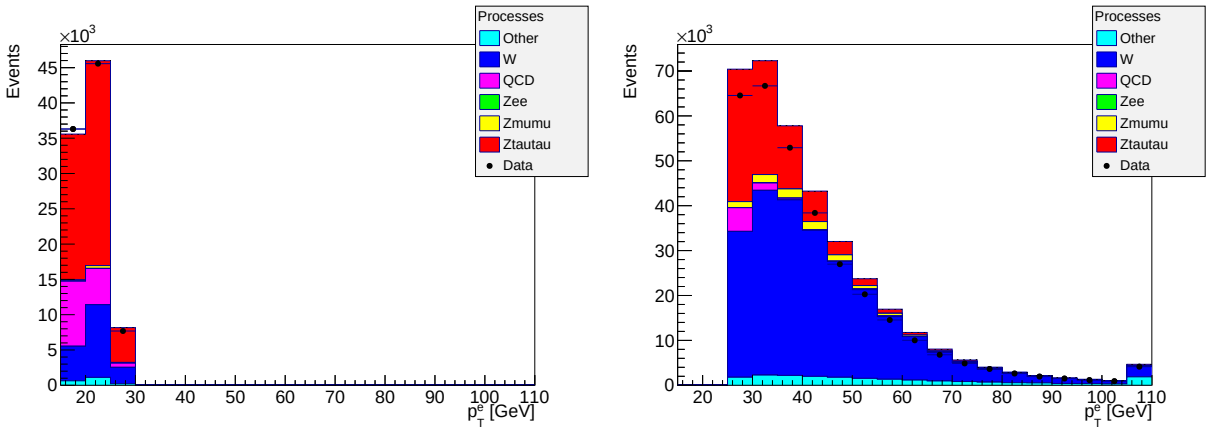

a) LTT channel
$17\,\text{GeV} < p_T^\mu < 22\,\text{GeV}$
$p_T^\tau > 25\,\text{GeV}$

b) SLT channel
$p_T^\mu > 22\,\text{GeV}$
$p_T^\tau > 20\,\text{GeV}$

Figure 5.3.: Lepton transverse momentum p_T of the muon channel: the classification into the SLT and LTT channel. These plots show the comparison of data and simulated background including QCD multijet after the preselection depicted in Figure 5.9. For more information, see Figure 5.1.

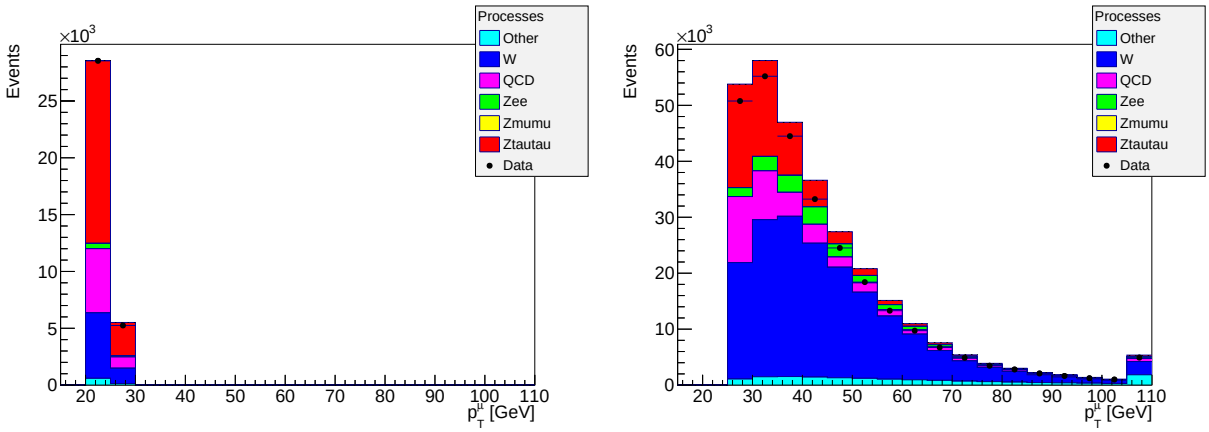

a) LTT channel
$17\,\text{GeV} < p_T^e < 25\,\text{GeV}$
$p_T^\tau > 25\,\text{GeV}$

b) SLT channel
$p_T^e > 25\,\text{GeV}$
$p_T^\tau > 20\,\text{GeV}$

Figure 5.4.: Lepton transverse momentum p_T of the electron channel: the classification into the SLT and LTT channel. For more information, see Figure 5.3.

$W \to \ell\nu$ background rejection The remaining dominant background after the preselection of the CommonNtuple (see Figure 5.9) is coming from the W+jets production. To reduce its contributions to the signal region, several additional cuts are applied.

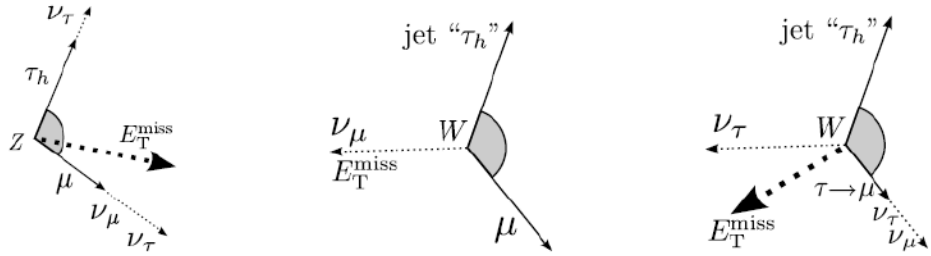

(a) $Z \to \tau\tau \to \mu\tau_h$ (b) $W \to \mu\nu$ (c) $W \to \tau\nu \to \mu\nu\nu\nu$

Figure 5.5.: a) For $Z \to \tau_{\text{lep}}\tau_{\text{had}}$, $\not{E}_T$ lies between the lepton and tau, since the tau decay lead to collimated daughter particles. b) and c) In case of W decay, the momenta of the daughter particles are balanced, so that $\not{E}_T$ lies outside of the angle [93, p. 86].

A powerful observable to distinguish between W+jets and $Z \to \tau_{\text{lep}}\tau_{\text{had}}$ events is based on the angular distance between the missing transverse energy and the reconstructed lepton $\Delta\phi(\not{E}_T, \ell)$ and tau $\Delta\phi(\not{E}_T, \tau)$. The Z boson is heavier than the two taus, so that the $Z \to \tau\tau$ process leads to boosted decay products. Therefore, the further decay of the tau leptons results in collimated daughter particles. The neutrinos coming from these decays are summed up experimentally within the missing transverse energy. For $Z \to \tau\tau$ events, the vector of $\not{E}_T$ lies generally in the angle between the reconstructed τ_{had} and τ_{lep} (see Figure 5.5). In contrast to that, the vector of $\not{E}_T$ of W+jets decays lies outside of the angle of the identified lepton and tau. This topological character of such events can be quantified by the following formula. 5.4.

$$\sum \cos\Delta\phi = \cos(\phi(\ell) - \phi(\not{E}_T)) + \cos(\phi(\tau_h) - \phi(\not{E}_T)) \tag{5.4}$$

Taking this definition, one expects events with $\sum \cos\Delta\phi \approx 0$ in case of back-to-back taus from non-boosted Z bosons and $0 < \sum \cos\Delta\phi < 2$ for boosted Z bosons. Figure 5.6 shows the distribution of described quantity. The first and the last bin in the plots imply respectively the underflow and overflow events beyond the plotted spectrum. The distributions agree with the expectations of a peak of signal events at zero. In contrast to the idealization of complete collimated daughter particles of the tau decays, there are signal events below the null value. Finally, a cut of $\sum \cos\Delta\phi > -0.15$ allows to reject many background events coming from the W production with jets.

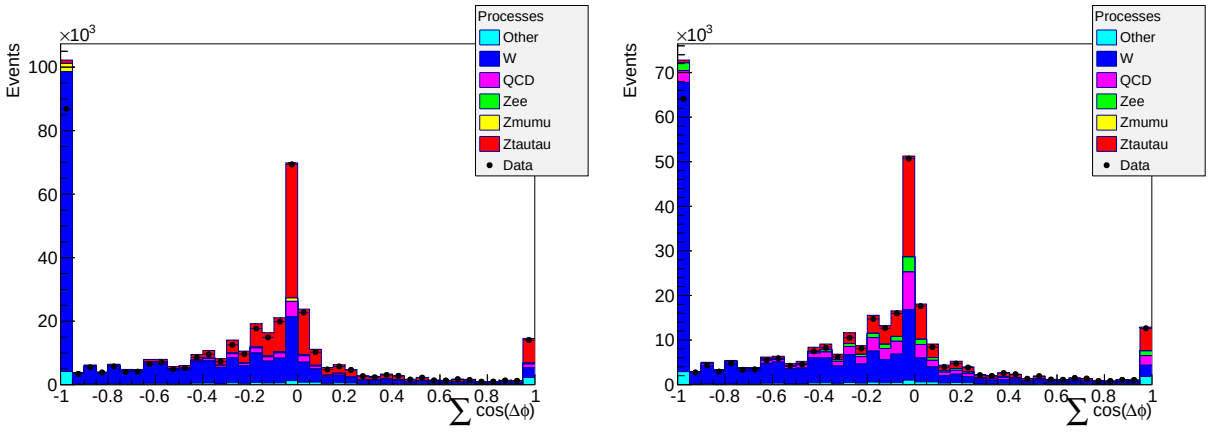

a) Muon channel b) Electron channel

Figure 5.6.: Distribution of $\sum \cos\Delta\phi$ before the cut on it (see Figure 5.10): this quantity returns values greater than zero, if the vector of $\not{E}_T$ lies inside of the angle of the reconstructed hadronic tau and lepton. Else, it returns negative values. It offers a good separation between $Z \to \tau\tau$ and W+jets. For more information, see Figure 5.3.

Another way to distinguish between $Z \to \tau\tau$ and W+jets events is a cut on the transverse mass m_T, defined as

$$m_T = \sqrt{2p_T^{\ell}\not{E}_T(1 - \cos\Delta\phi(\ell, \not{E}_T))}\,. \tag{5.5}$$

It is as commonly used variable to describe the mass of W bosons, since neutrinos are among the daughter particles. One of the advantages is that the m_T distribution is relatively insensitive to the production dynamics of W bosons [94].

The produced Z bosons have under the given experimental terms in general a small p_T. Therefore, the τ leptons coming from the Z decay are expected to be most of the time back-to-back resulting into a highly balanced missing transverse energy and consequently a small transverse mass m_T. Figure 5.7 shows the distribution of the transverse mass of the remaining events after the cut on $\sum \cos\Delta\phi$. One sees the agreement of these expectations with the distributions of the transverse mass of the two lepton channels. In contrast to the contribution of $Z \to \tau\tau$ events, the transverse mass of a W+jets sample peaks around 70 GeV. So, the cut of $m_T < 50\,\text{GeV}$ has a good background rejection of W+jets events with a high signal efficiency.

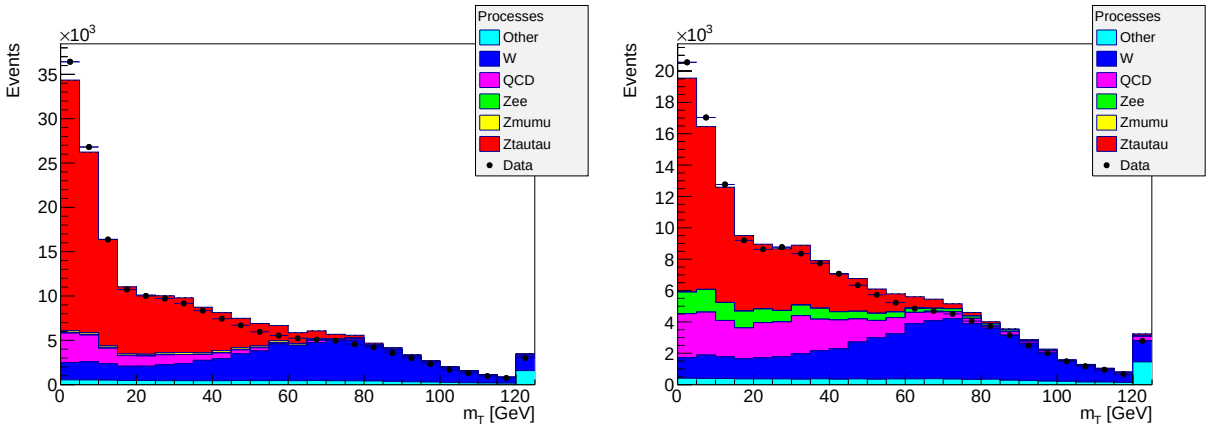

a) Muon channel b) Electron channel

Figure 5.7.: Distribution of the transverse mass m_T before the cut on it (see Figure 5.10): In contrast to $Z \to \tau\tau$ events, the distribution of W+jets production peaks at 70 GeV. Therefore, the signal region is limited to $m_T < 50$ GeV. For more information, see Figure 5.3.

The two previous cuts are based on the angular distribution between the measured particles and the missing transverse energy. Furthermore, one can use the angle between the hadronic tau and the lepton $\Delta\phi(\tau_{had}, \ell)$ to consider directly the back-to-back character of the $Z \to \tau\tau$ decay. The distributions of the angular distance $\Delta\phi$ is in Figure 5.8. At this stage of the cutflow, this observable does not offer a quantity with high separation power, but a cut of $\Delta\phi > \frac{\pi}{2}$ still allows to purify the signal region.

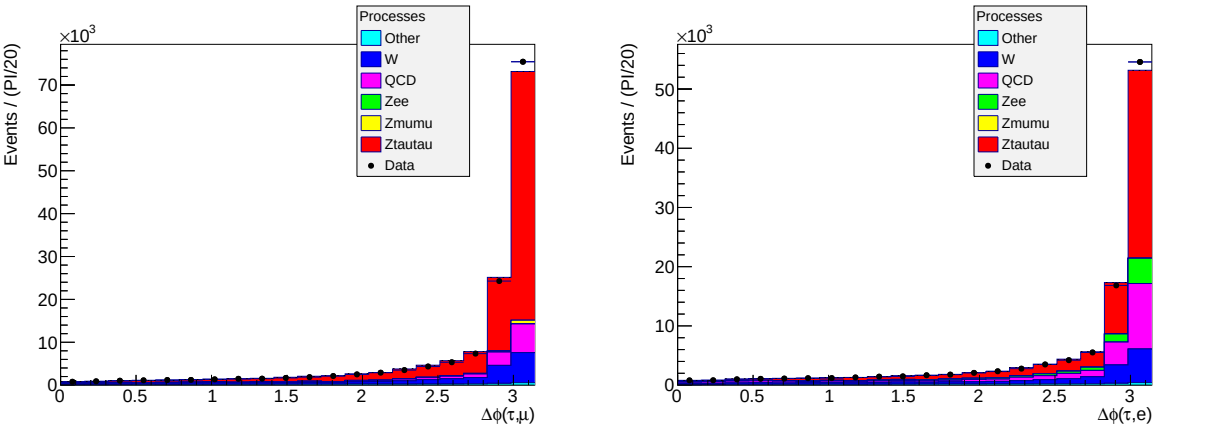

a) Muon channel b) Electron channel

Figure 5.8.: The distribution of $\Delta\phi(\tau_{had}, \ell)$ before the cut on it (see Figure 5.10): $Z \to \tau\tau$ events tend to be back-to-back. The event selection cuts on $\Delta\phi > \frac{\pi}{2}$. For more information, see Figure 5.3.

5.1.4. The cutflow

The following tables summarize the complete cutflow of the event selection. Table 5.2 and Table 5.3 show the signal efficiencies and background rejection efficiencies at each cut stage. An overview of the absolute numbers can be found in Appendix B.

The first cut 'CommonNtuple' describes the selection of the lepton-hadron CommonNtuples. The five subsequent cuts incorporate the preselection of the lepton hadron channel. It imposes the rough signal selection based on the event topology. So, the selection up to this point implies the choice of the lepton flavour channel and it rejects the events of the control regions offered by the selection of the CommonNtuple. The signal efficiency at this stage of the cutflow is 0.592% (0.322%) (137987 (75083) expected $Z \to \tau\tau$ events) with a background rejection of 99.961% (99.967%) (288522 (217326) expected background events excluding QCD multijet events) in the muon (electron) channel. The cutflow of this preselection is shown in Figure 5.9. Since the estimation of the QCD background is based on the inverted isolation, tau identification and opposite sign criteria, it is therefore not given at this stage of the cutflow.

The following cuts are set to reach a higher purity of the signal region and to reduce the W+jets background (Figure 5.10). These four (three) cuts have a signal efficiency of 68.5% (68.6%) and background rejection of 88.6% (83.4%). The overall selection including the preselection of the CommonNtuples leads to a signal efficiency of 0.406% (0.221%) (94555 (51527) expected $Z \to \tau\tau$ events) with a background rejection of 99.996% (99.995%) (35389 (43230) expected background events including QCD multijet events) in the muon (electron) channel. In case of the muon channel, an additional cut 'Tau-is-muon veto' is applied. As in the preselection of electron candidates, it comprises a BDT trained to reject muons faking taus. All distributions of the following cross section studies are constrained to these described signal regions.

Table 5.2.: Cutflow of the muon channel: signal efficiencies and background rejections. The first entry describes the preselection of the data type 'CommonNtuple' followed by cuts of the event topology of the muon-hadron channel of $Z \to \tau\tau$ events. 'Tau-is-muon veto' is a BDT trained to reject muons faking taus. The last three cuts are aimed to reject W+jets events.

Cuts	**Total eff.**	**Total backgr. rej.**	**Efficiency**	**Background rej.**
No Cuts	1.00000	0.00000	1.00000	0.00000
CommonNtuples	0.01182	0.99614	0.01182	0.99614
Muon	0.00738	0.99724	0.62433	0.28567
OppositeSign	0.00727	0.99844	0.98433	0.43571
dilepVeto	0.00726	0.99846	0.99989	0.01186
Isolated lepton	0.00592	0.99961	0.81522	0.74363
Tau	0.00592	0.99961	0.99933	0.01003
Tau-is-muon veto	0.00572	0.99963	0.96655	0.04915
$\sum \cos\Delta\phi > -0.15$	0.00464	0.99988	0.81127	0.68017
$m_T < 50\,\text{GeV}$	0.00430	0.99995	0.92758	0.55659
$\Delta\phi > \frac{\pi}{2}$	0.00406	0.99996	0.94211	0.15684

Table 5.3.: Cutflow of the electron channel: signal efficiencies and background rejection. The first entry describes the preselection of the data type 'CommonNtuple' followed by cuts of the event topology of the electron-hadron channel of $Z \to \tau\tau$ events. The last three cuts are aimed to reject W+jets events.

Cuts	**Total eff.**	**Total backgr. rej.**	**Efficiency**	**Background rej.**
No Cuts	1.00000	0.00000	1.00000	0.00000
CommonNtuples	0.01182	0.99614	0.01182	0.99614
Electron	0.00444	0.99890	0.37567	0.71433
OppositeSign	0.00435	0.99935	0.97909	0.41309
dilepVeto	0.00435	0.99936	0.99995	0.01321
Isolated lepton	0.00322	0.99967	0.74130	0.48195
Tau	0.00322	0.99967	0.99909	0.01182
$\sum \cos\Delta\phi > -0.15$	0.00260	0.99988	0.80768	0.62033
$m_T < 50\,\text{GeV}$	0.00239	0.99994	0.91721	0.48664
$\Delta\phi > \frac{\pi}{2}$	0.00221	0.99995	0.92637	0.14951

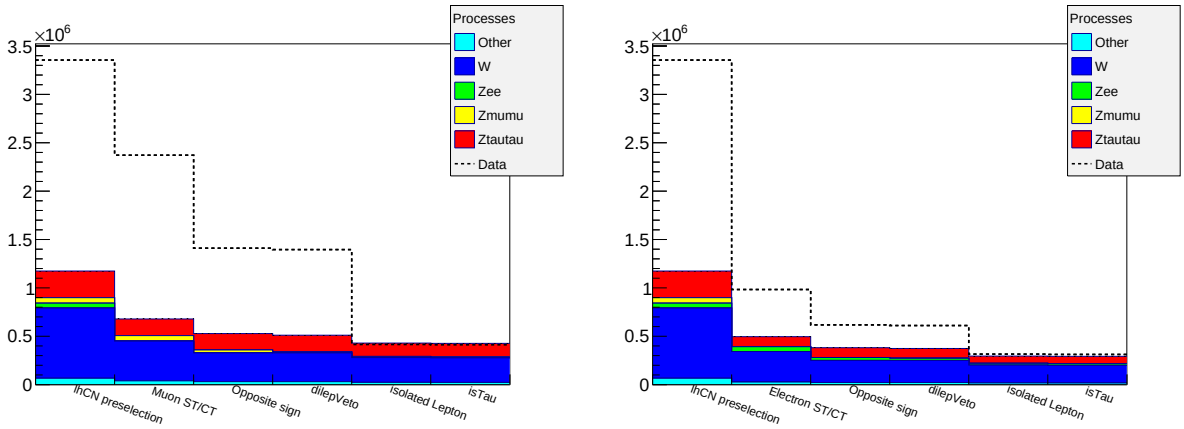

a) Muon channel a) Electron channel

Figure 5.9.: Cutflow of the preselection. The plot shows for every cut stage of the preselection the number of expected events given by MC simulations depicted by the coloured stacked histogram and the number of measured data events represented by the dashed line. The QCD jet background estimation can only be made after the preselection, since the template method works with inverting the isolation criteria.

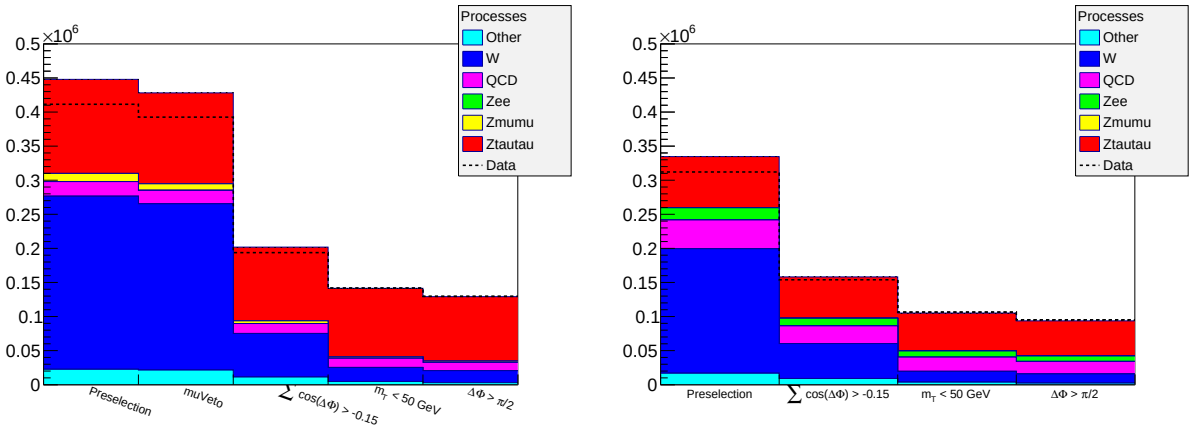

a) Muon channel a) Electron channel

Figure 5.10.: Cutflow of the selection. The plot shows the developments of the signal composition of the selection cuts applied to predominantly reject W+jets events. For more information, see Figure 5.9.

5.1.5. Distributions of the signal region

The differential cross section is studied for the distributions of the lepton transverse momentum p_T^ℓ, the tau transverse momentum E_T^τ, visible mass m_{Vis}, and the invariant Z mass m_Z, separately for the muon and electron channel. The tau transverse momentum is based on the identification of a tau jet. Hence, E_T^τ does not comprise the momentum of the neutrino of the tau decay. Likewise, the visible mass is the invariant mass of the reconstructed lepton and hadronic tau only. In contrast, the invariant mass m_Z describes the invariant mass of the $Z \to \tau\tau$ decay. The missing mass calculator reconstructs m_Z on the basis of the lepton and tau momenta, the missing transverse energy, and the resolution of the missing transverse energy [95].

The following plots describe the comparison of the full $\sqrt{s} = 8\,\text{TeV}$ dataset recorded by the ATLAS experiment and the stacked background simulation, taken from MC and data driven methods. Below the stacked plots, the ratio between the data and the expected simulation is shown. The yellow error bands include the systematic uncertainties from the simulation. These include the scaling uncertainties on the theoretical cross sections, the statistical uncertainties of the MC data and finally the uncertainties coming from the template method for the QCD multijet estimation. Further uncertainties, which will be described in Section 5.3.1 are not included at this point. The black error bars describe the statistical uncertainties of the data only.

In the main region of signal of $[20, 60]\,\text{GeV}$, simulation and data of the tau transverse momentum E_T^τ (Figure 5.11) match within the systematic uncertainties of $\pm 5\%$. The simulation of the first two bins results in an underestimation of the expected number of events and the following two tend to overestimate the expected number of events. In contrast, the distributions of the lepton transverse momentum in Figure 5.12 show an obvious trend from an overestimate to an underestimate of the data within the central region of $[15, 45]\,\text{GeV}$ to a deviation of ~10%. These are the most dominant discrepancies and are reflected in the distribution of the visible mass m_{Vis} (Figure 5.13), which consequently results also in an slight underestimate in low mass $m_{Vis} < 65\,\text{GeV}$ and an overestimate in higher mass region $65\,\text{GeV} < m_{Vis} < 100\,\text{GeV}$. Likewise, the Z mass distributions in Figure 5.14 show a good matching of the simulation and data within $\pm 5\%$. Finally, the trends of the muon and electron channel show similar behaviours.

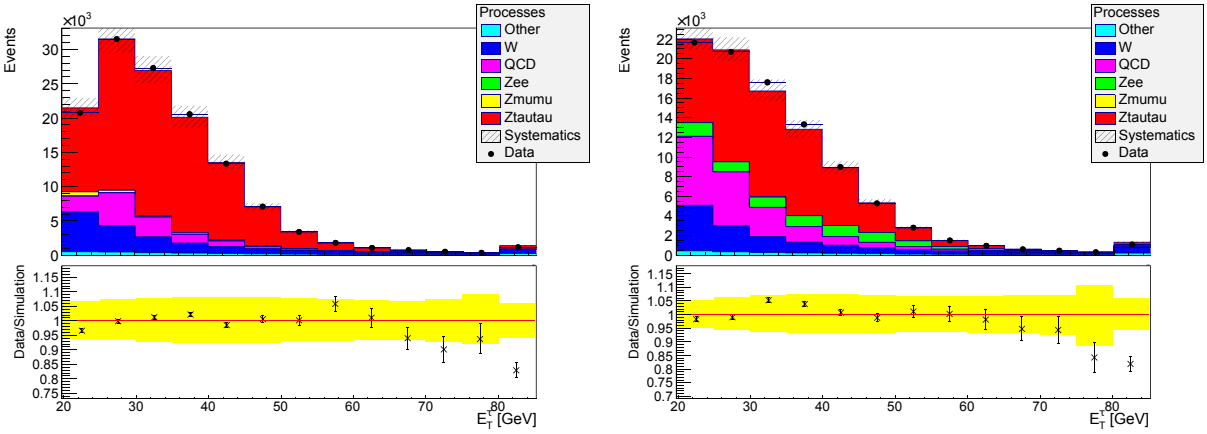

a) Muon channel b) Electron channel

Figure 5.11.: The tau transverse momentum E_T^τ distribution of the signal region after the final cut (see Figure 5.10). The coloured stacked histogram represents the simulation of the signal. The hatched area depicts the systematic uncertainties of the simulations. It comprises the theoretical uncertainties of the cross sections and uncertainties coming from the template method. The black dots are the measured data points. The black crosses in the ratio plot describe the matching of data and simulation. Its error bars comprise the statistical uncertainties from data. The yellow error band depicts the systematical uncertainties of the simulation.

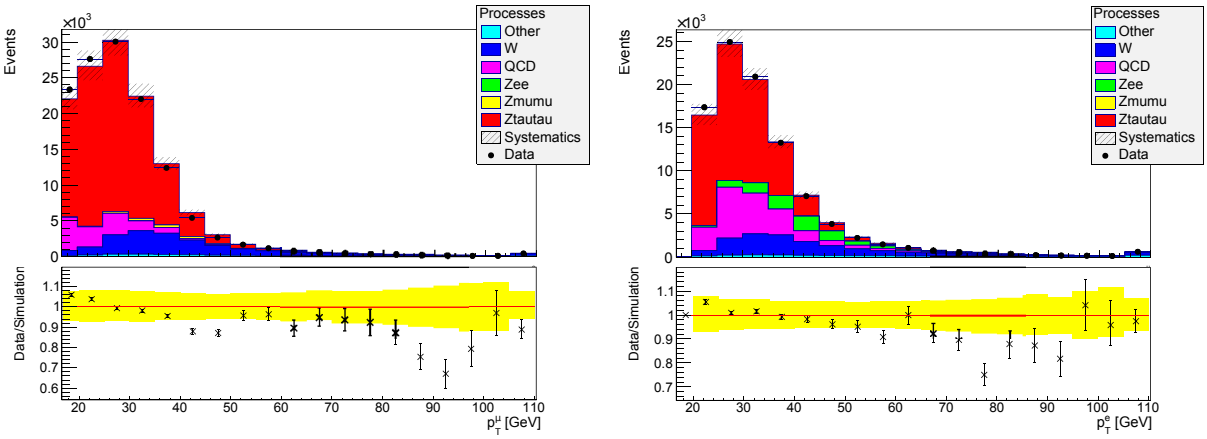

a) Muon channel b) Electron channel

Figure 5.12.: The lepton transverse momentum p_T^ℓ distribution of the signal region after the final cut. For more information, see Figure 5.11.

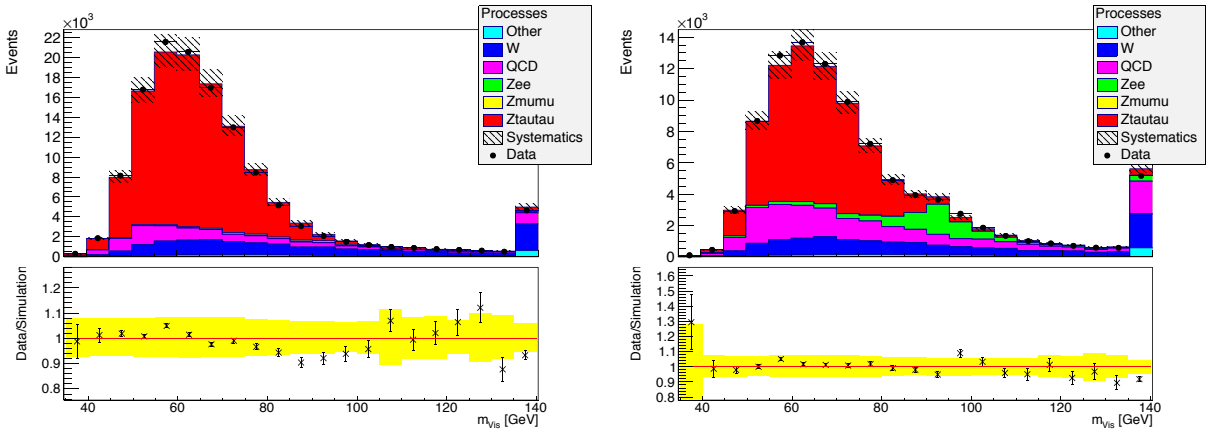

a) Muon channel b) Electron channel

Figure 5.13.: The visible mass m_{Vis} distribution of the signal region after the final cut. For more information, see Figure 5.11.

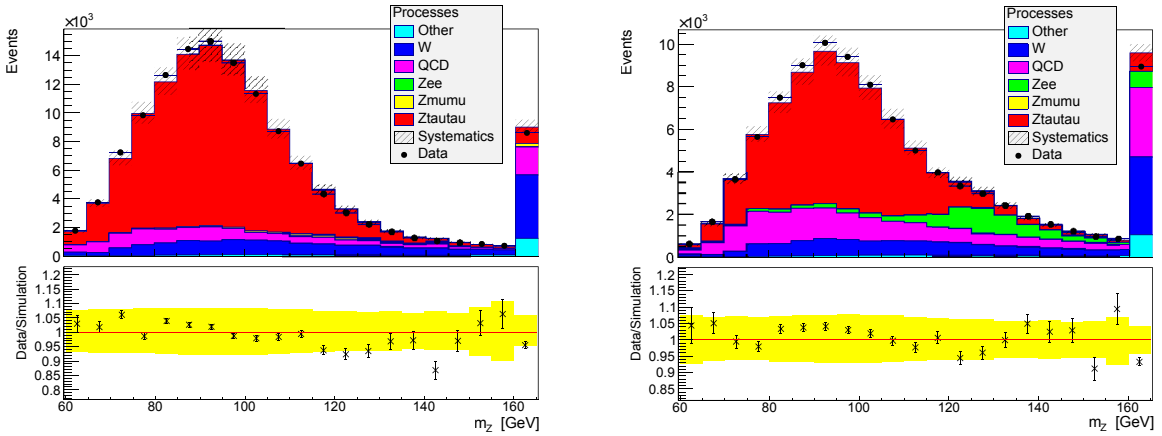

a) Muon channel b) Electron channel

Figure 5.14.: The invariant Z mass m_Z distribution of the signal region after the final cut. For more information, see Figure 5.11.

5.2. The template method

5.2.1. Concept

The basic concept of the template method to model the fake background is based on the extrapolation of the number of QCD multijet events from a background enriched control region to the signal region. Therefore, one defines a region B which is orthogonal to the signal region A and dominated by the unmodelled background. Commonly, one inverts the 'opposite sign' (OS) criterion to the 'same sign' (SS) to enrich the QCD multijet events of region B. Due to charge conservation, this region is orthogonal to any $Z \to \ell\ell$ with subsequent $\ell = e, \mu, \tau$ decay. One takes the distribution of the wanted observable in this region and subtracts the other background contributions known from MC simulations. By construction of region B the remaining events are the unmodelled background, which is identified as the QCD contribution. Afterwards, one has to scale the obtained distribution of this QCD multijet background to account for the transition from region B to region A. Either the scaling factor can be obtained by a fit of the background shape taken from region B to the data in region A (or another control region) or it is extracted from another pair of orthogonal control regions C and D. They must be also dominated by the background and describe the same transition as A and B (see Figure 5.15). Here, the construction of the region C and D is based on the inversion of the isolation criteria, which are dominated by a non-simulated process as is discussed in Section 5.1.1.

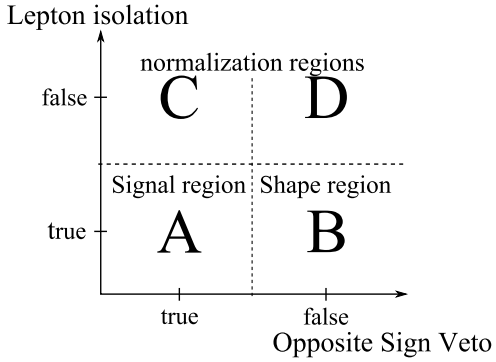

Figure 5.15.: The signal and control regions of the ABCD method.

In summary, the distribution $f_A(O)$ of the observable O of the QCD multijet background of the signal region A is calculated by

$$f_A^{\text{multijet}}(O) = f_B^{\text{multijet}}(O) \cdot \frac{N_C^{\text{multijet}}}{N_D^{\text{multijet}}} \tag{5.6}$$

with number of estimated QCD multijet events $N_{\{C,D\}}^{\text{multijet}}$ occurring in region C and D.

The template method is based on several assumptions. Firstly, the construction of the control regions B, C, and D subtracting the MC modelled background prevents any signal leakage. If that was not the case, signal events in region B would be treated as background. This would lead to an overestimate of the QCD multijet background. A signal leakage towards the control regions C and D could have a bias on the scale factor in both directions depending on the degree of signal contamination of the respective region. Secondly, the template method returns only reliable results in case of uncorrelated discriminative variables. Otherwise, one could not expect that the relation of the scaling factor

$$\frac{N_C^{\text{multijet}}}{N_D^{\text{multijet}}} = \frac{N_A^{\text{multijet}}}{N_B^{\text{multijet}}} \tag{5.7}$$

is correct. To be specific, the method would be valid in case of a correlation of the observable O to the discriminative variable of the regions, if one considered a scale factor depending on O. This approach is highly limited by the statistics, such that uncorrelated variables are desirable and a global scale factor can be used.

5.2.2. Studies of the assumptions

The above assumptions concerning the correlations between control regions have to be verified. Here, just the results of the muon channel are discussed in every step. The non-mentioned tables and plots of the electron channel are summarised in Appendix C.
The first assumption is that the SS/OS criterion and the cut on the lepton isolation are independent. Otherwise, Equation 5.7 would not be satisfied. The composition of region A, B, C, and D is summarised in Table 5.4. The entry 'Rest' is the difference of measured data events and the MC simulated events. The OS/SS-ratios of the 'Rest' events are

$$\frac{N_A^{multijet}}{N_B^{multijet}} = 1.11 \tag{5.8}$$

$$\frac{N_C^{multijet}}{N_D^{multijet}} = 1.141 \tag{5.9}$$

The deviation of these ratios is less than 3%, which is compatible with expected uncertainties coming from theoretical and statistical uncertainties. Equation 5.7 is fulfilled and it approves the validity of the control regions. Therefore, the construction of the control regions B, C, and D by inverting the OS/SS and isolation criteria can be used for the

template method.

Table 5.4.: Composition of the regions A, B, C, and D of the muon channel in case of 'lepton isolation' and 'OS/SS' inversion.

	A	B	C	D
Lepton isolation	✓	✓	✗	✗
Opposite Sign	✓	✗	✓	✗
Data	129541	20470	484757	403134
Ztautau	94554	918	22249	300
Zmumu	1891	1201	323	164
Zee	0	0	2	3
W	17607	6546	3721	1323
Other	2986	496	1095	555
Rest[1] / N^{multijet}	12500	11307	457366	400787

[1] Inconsistencies between the number of data events, MC events and rest come from rounded MC event numbers, since MC weights lead to non-integer results.

The choice of the control regions seems to be appropriate. Nevertheless, a cross check of the control region configuration is reasonable. The only other possibility of variable pairs of the preselection would be the inversion of the OS and the 'medium' BDT score of the tau identification. Since the skimming of the used CommonNtuples (see Section 5.1.3) has rejected these events, one can just use the inversion of a 'tight' BDT score. Hence, the control regions B', C', and D' are based on a hypothetical signal region with a 'tight' tau identification. To use the results of the adopted regions, it is scaled to the number of control region B.

$$f_A^{\text{multijet}}(\vec{x}) = f_{B'}^{\text{multijet}}(\vec{x}) \cdot \frac{N_{C'}^{\text{multijet}}}{N_{D'}^{\text{multijet}}} \cdot \frac{N_B^{\text{multijet}}}{N_{B'}^{\text{multijet}}} \tag{5.10}$$

The composition of the adopted control regions B', C', and D' are presented in Table 5.5. Here, the transition factor computed is

$$\frac{N_{C'}^{multijet}}{N_{D'}^{multijet}} = 1.30 \pm 0.03\,(\text{stat}) \pm 0.05\,(\text{sys}). \tag{5.11}$$

It differs significantly from the global extrapolation factor based on the isolation criterion of 1.141 and the reference value of 1.11 in Equation 5.8 and Equation 5.9. The change of the tau identification from 'medium' to 'tau' may be too strong, but offers a way to compare the following validity checks. Since the approach of inverting the isolation criterion

seems to be more appropriate, the template method based on the tau identification will be used as conservative estimation of the systematical error.

Table 5.5.: Composition of the control regions of the muon channel. The signal region A and the control region B are based on the standard selection. B', C', and D' relay on the 'tight' tau identification.

	A	B	B'	C'	D'
BDT score	'medium'	'medium'	'tight'	not 'tight'	not 'tight'
Opposite Sign	✓	✗	✗	✓	✗
Data	129541	20470	7372	53683	13407
Ztautau	94554	918	393	30620	532
Zmumu	1891	1201	402	1116	810
Zee	0	0	0	0	0
W	17607	6546	2066	11366	4689
Other	2986	496	166	1505	392
Rest / N^{multijet}	12500	11307	4342	9074	6982

The extrapolation factor

Moreover, the claimed independence between the OS/SS ratio $r_{OS/SS}$ and the distribution variable has to be verified. Figures 5.16 shows the extrapolation factor $r_{OS/SS}$ in dependence of the lepton and the tau transverse momentum. Additionally, the global extrapolation factor (Equation 5.9) is also indicated. Apart from slight trends around the global factor, the distribution depending on the lepton distribution seems to be consistent with the assumption of a constant extrapolation factor. Indeed, $r_{OS/SS}(E_T^\tau)$ shows a clearly increasing curve. This means, that for higher tau transverse momenta, there are more fake lepton tau pairs with opposite signs than pairs with same signs.

While muons exhibit a clear signature in the detector and thus are most likely originating from (heavy) quark decays, this is not the case for reconstructed tau decays. They can be easily misidentified from jets. Therefore, one can expect, that the detected muon comes from the decay from one of the particles of leading transverse momentum of the event.

A jet faking a hadronic tau decay is the counterpart of the detected muon. Since its transverse momentum is arbitrary, the ratio of 'opposite sign' and 'same sign' tau candidates should be constant concerning the lepton transverse momentum distribution. It could even lead to a decreasing ratio with the lepton momentum, since the phase space of underlying jets increases with increasing lepton momentum leading likewise to more SS

and OS tau candidates. This would limit the previous dominance of the 'opposite sign' events.

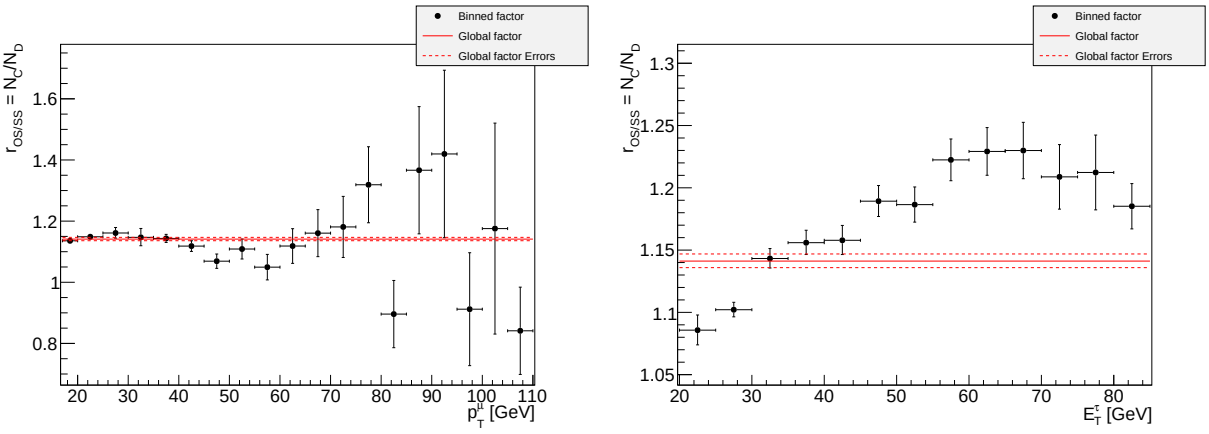

a) Lepton transverse momentum p_T^μ b) Tau transverse momentum E_T^τ

Figure 5.16.: The global and binned extrapolation factor $r_{\mathrm{OS/SS}}$ of the tau and lepton momenta based on the standard control regions of 'lepton isolation' inversion of the muon channel.

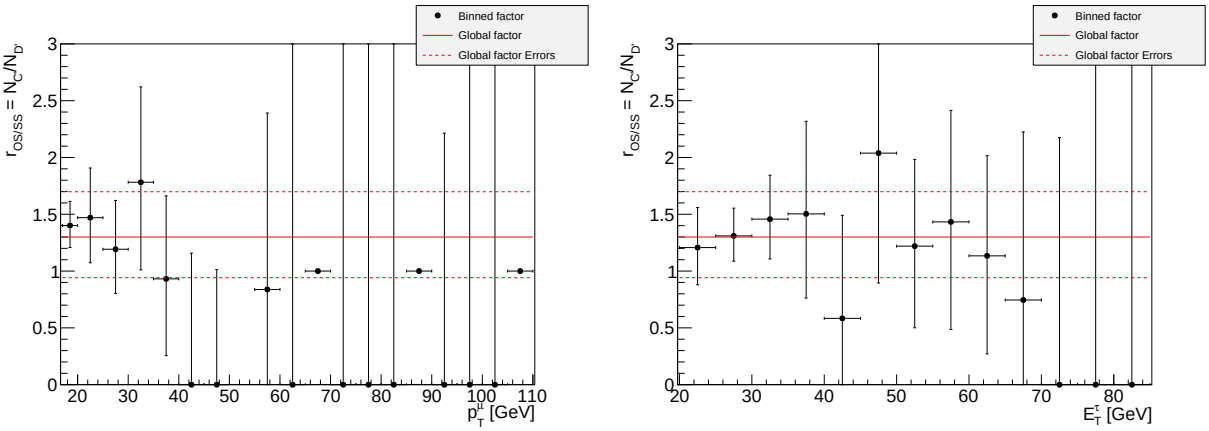

a) Lepton transverse momentum p_T^μ b) Tau transverse momentum E_T^τ

Figure 5.17.: The global and binned extrapolation factor $r_{\mathrm{OS/SS}}$ of the tau and lepton momenta based on the alternative control regions of inverted tau identification 'tight' of the muon channel. The ratio points of $r_{\mathrm{OS/SS}} = 1$ without error bars describe the ratio of two empty bins.

The increase of the ratio with increasing tau transverse momentum is due to the same effect. The higher the mass of the reconstructed hadronic tau, the higher the chance it is a high energy jet forming the electric counterpart of the muon.

The same trends can be observed in the control plots based on the inversion of the tau identification criterion in Figure 5.17. While the statistical uncertainties dominate, the

increasing trend is easily visible.

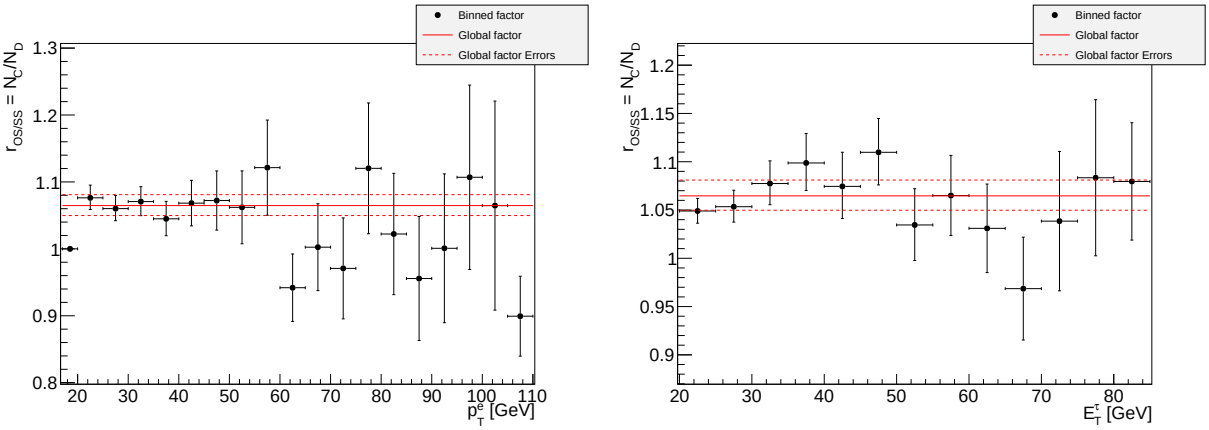

a) Lepton transverse momentum p_T^e b) Tau transverse momentum E_T^τ

Figure 5.18.: The global and binned extrapolation factor $r_{\mathrm{OS/SS}}$ of the tau and lepton momenta based on the standard control regions of 'lepton isolation' inversion of the electron channel.

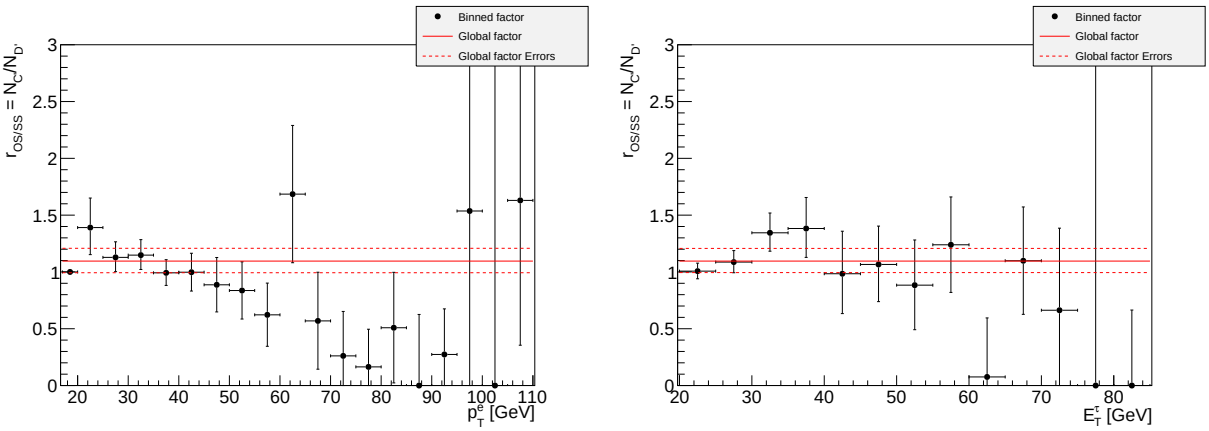

a) Lepton transverse momentum p_T^e b) Tau transverse momentum E_T^τ

Figure 5.19.: The global and binned extrapolation factor $r_{\mathrm{OS/SS}}$ of the tau and lepton momenta based on the alternative control regions of inverted tau identification 'tight' of the electron channel.

The plots for the electron channel in Figure 5.19 show a similar shape, which can be explained basically in the same way as the muon channel. The difference is the purity of electron candidates. Since the signature of electrons is not as clear as for muons, jets can also mimic electrons. Therefore, the described effect should be oppressed, as the jets fake 'same sign' and 'opposite sign' electrons too. The low amount of statistics does not allow to illustrate this difference. The cross check of the template method by inverting

the tau identification offers unexpected results in the electron channel. The $r_{OS/SS}$ curve in dependence of the lepton transverse momentum in Figure 5.19 drops even below 1, while a ratio greater than 1 is expected due to the expected favoured OS events. The dominance of the SS events over the OS in high momentum regions cannot be explained by this effect and this is an open question at this stage of the analysis.

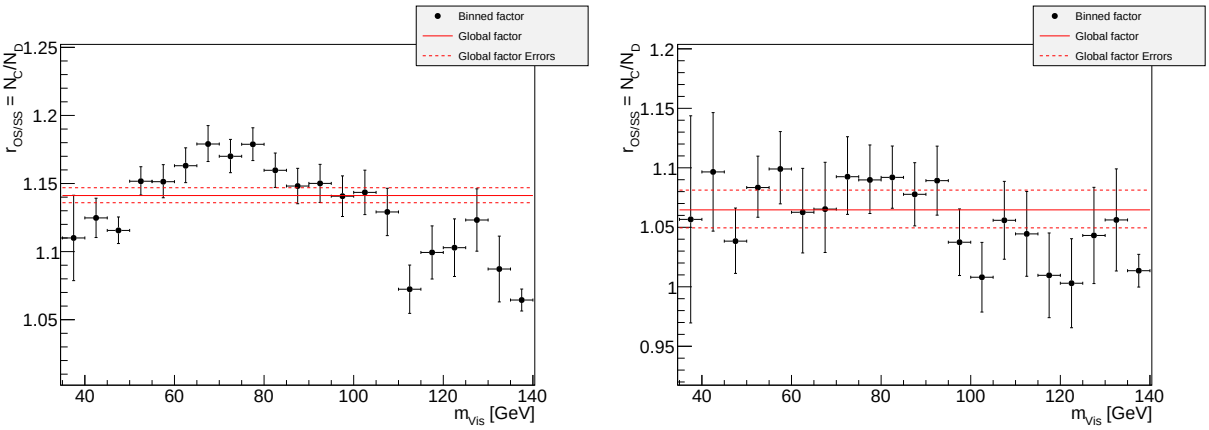

a) Muon channel b) Electron channel

Figure 5.20.: The global and binned extrapolation factor $r_{\mathrm{OS/SS}}$ of the visible mass distribution of the nominal choice of control regions.

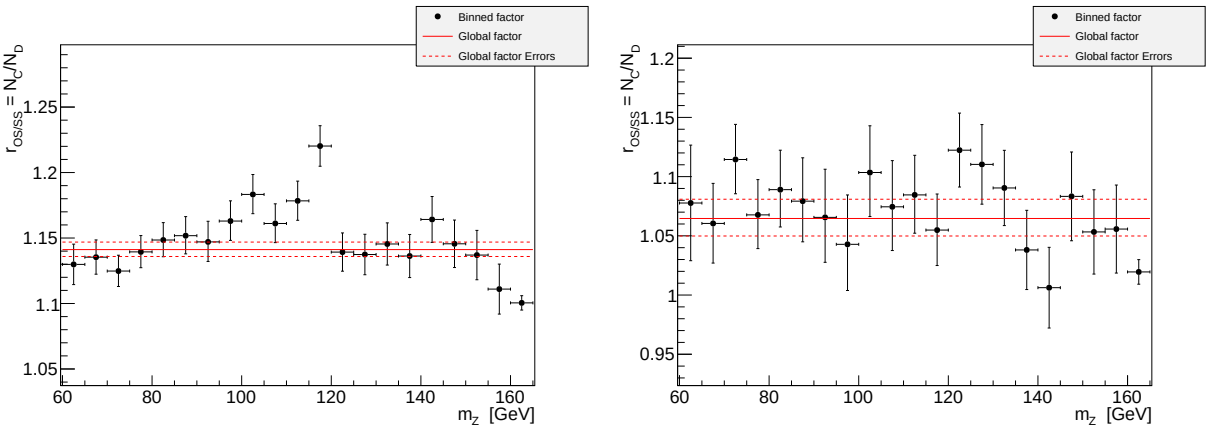

a) Muon channel b) Electron channel

Figure 5.21.: The global and binned extrapolation factor $r_{\mathrm{OS/SS}}$ of the invariant Z mass distribution of the nominal choice of control regions.

Consequently, the non-flat distributions shapes of the ratio plots of the lepton and tau transverse momentum have an impact on the shape of the visible mass and the invariant Z mass. The plots of $r_{OS/SS}$ depending on the visible mass and the Z invariant mass in Figure 5.20 and Figure 5.21 mirror the clear trends of the ratio plots of the lepton

and tau transverse momentum. Nevertheless, the peak of the shapes is suspicious. The distribution seems to reflect the shape of the signal, which could be a hint that there is a significant amount of signal leakage into the control regions. Indeed, the shapes of these ratios $r_{OS/SS}$ of the electron channel do not show such a clear similarity to the signal.

On the one hand, the assumption of a constant extrapolation factor $r_{OS/SS}$ over the whole distributions seems not to be valid in any case. On the other hand, the shape of the ratios is not fully understood. Both approaches have their motivations, such that the constant factor is used as the nominal method and the variable factor (of the isolation based template method) is used to derive the systematics of the method. In the peak regions, the statistical errors of the variable factors are sufficiently small, that the resulting systematic uncertainties of the template method remain reasonable.

Shape

The shape of the background estimation originates from region B, which is the same as the signal region aside of the inversion of the OS criterion. To extract the influence on the shape of the background processes, one takes the shape of the data (see Figure 5.22)

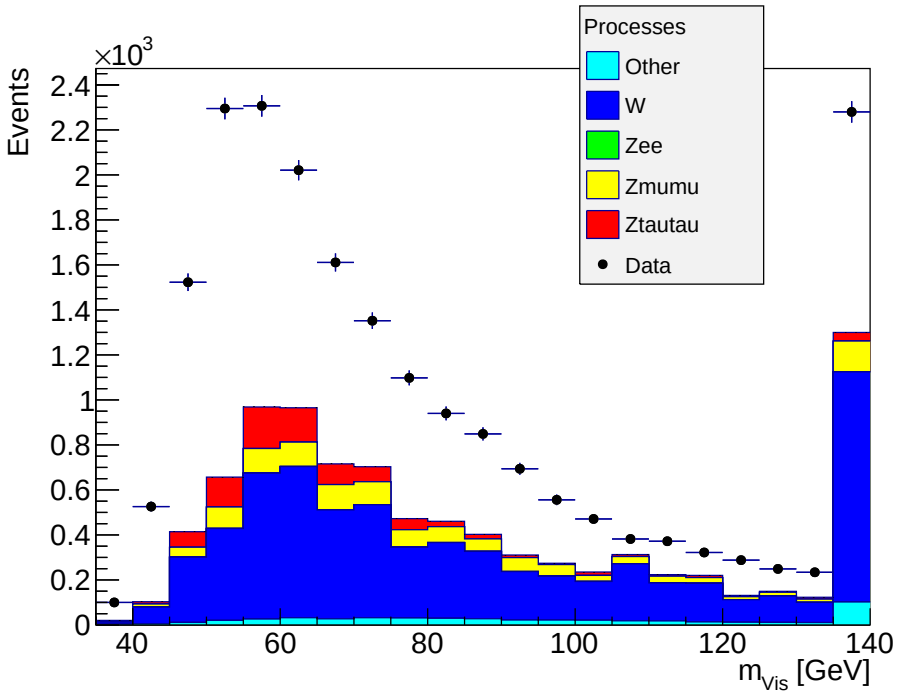

Figure 5.22.: The shape of the background estimation is the difference of the data distribution and the distribution of the stacked MC simulations. The gap between the data and the simulations is identified as the QCD multi-jet background distribution of region B of the visible mass of the muon channel.

and subtracts all known and simulated background contributions. Assuming a perfect and complete simulation of all other contributions, the isolation cut would not have any impact on the background estimation. As this assumption does not hold, the impact of the arbitrarily chosen isolation cut of 4% must be studied. For this purpose, one varies the isolation cut from the value of the signal to 5% and 3%. Following the construction of the control regions of the template method depicted in Figure 5.15, the variation of the signal region results in a change of region D. Likewise in Equation 5.10, the resulting background estimation of the varied signal regions is scaled with the number of estimated background events of the nominal signal region. The different shapes of region B scaled with the extrapolation factor $R_{OS/SS}$ and when it is necessary with $N_B/N_{B'}$ are shown in Figure 5.23 a). The background estimation is rather stable against a shift of the isolation cut. The variations of the extrapolation are included in the systematical error of the estimation. Figure 5.23 b) shows the nominal QCD multijet estimation based on the isolation criterion and the estimation based on the tau identification. The two different control regions lead to a similar shape with different normalizations.

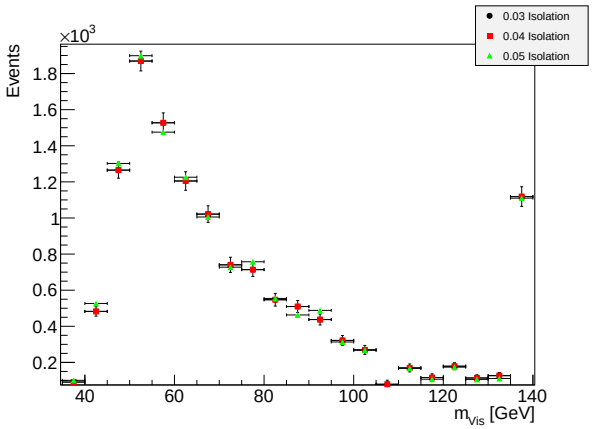

a) Extrapolated shapes based on different isolation cuts.

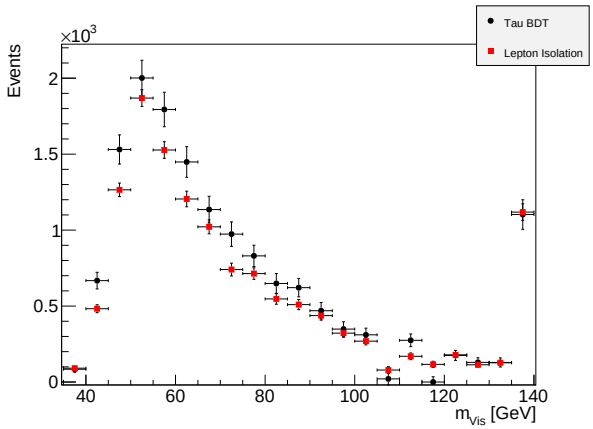

b) Extrapolated shapes based on the nominal isolation cut and the tau identification.

Figure 5.23.: Comparison of different extrapolated visible mass distribution shapes of the muon channel: a) shows the impact on the background estimation of varying the isolation cut, b) shows the difference of the cross check control regions based on the inversion of tau identification.

5.2.3. Findings

The template method offers an appropriate way to estimate the non-simulated QCD background. The different approaches of changing the control region from inverted isolation

to inverted tau identification and the variation of the isolation cut back up the stability of the method. However, the extrapolation ratios $r_{OS/SS}$ are not completely understood, which eventually insert larger systematic errors. The final QCD multijet background contribution including all systematics to the visible mass distribution is shown in Figure 5.24.

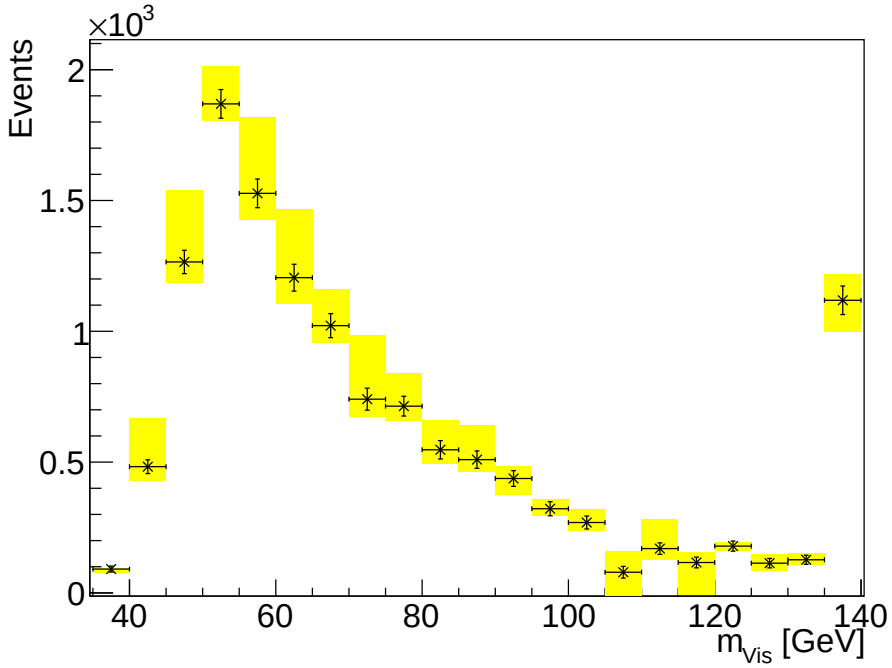

Figure 5.24.: The QCD multijet background estimation for the visible mass distribution of the signal region A of the muon channel including all systematics coming from varying the isolation cut, the bin-per-bin extrapolation and the alternative control regions based on the tau identification.

The template method returns the summed number of QCD multijet events of

$$N_A^{\text{multijet}} = 12903 \pm 163\,(\text{stat})\,^{+750}_{-434}\,(\text{syst}) \pm 141\,(\text{lumi}) \tag{5.12}$$

by integrating over the visible mass distribution. Table 5.6 summarises the uncertainties on this result. The shape and the normalization factor are based on data which is reflected in the statistical error. The theoretical uncertainties imply the uncertainty on the cross section (see Section 5.3.1). The entry 'Extrapolation factor' and 'Shape' contain the statistical errors of the MC samples. Thereby, the latter is the dominant uncertainty of the method itself. 'Alternative shapes' summarizes the effects of varying the isolation cut and 'Extrapolation bin per bin' comes from using the m_{Vis} depending extrapolation factor. The last and largest contribution comes from the alternative configuration of the template method, which is based on the inversion of the tau identification instead of the

isolation criterion.

Table 5.6.: Systematic uncertainties of the template method: the errors refer to the integrated number of estimated QCD multijet events of the visible mass distribution.

Uncertainty	**Absolute**		**Relative**	
Theoretical uncertainties	+88	-79	+0.68%	-0.61%
Extrapolation factor	+2	-2	+0.01%	-0.01%
Shape	+231	-231	+1.79%	-1.79%
Alternative shapes	+85	-100	+0.66%	-0.78%
Extrapolation bin per bin	+56	-49	+0.43%	-0.38%
Template Method based on tau idenfication	+607	-140	+4.71%	-1.08%

The QCD multijet estimation via the template method completes the estimation of another significant background. Figure 5.13 shows the visible mass distribution of the events passing the signal selection. The simulation of the background processes is good in a sense that the discrepancies between data and simulation is less than 5% in the region around the peak. A more detailed discussion about the agreement data and simulation is in Section 5.1.5.

5.3. Cross section

This section describes the results of the cross section measurements and the relevant systematic uncertainties. The four presented distributions lepton transverse momentum p_T^ℓ, tau transverse momentum E_T^τ, visible mass m_{Vis}, and invariant Z mass m_Z of Section 5.1.5 are used to calculate two differential cross sections for the muon and electron channel, respectively. Additionally, the resulting fiducial cross section of the constructed signal region and the total cross section are presented.

5.3.1. Systematics

The cross section measurement depends in many ways on the quality of modelling of the measurements. This section presents a list of the dominant systematics, which are considered within the results of the cross section. The summarized list of these systematical errors in regard to the fiducial cross section is shown in Table 5.8.

Integrated luminosity

The MC simulated background contributions are scaled with the integrated luminosity. Likewise, it enters in Equation 5.15. Therefore, its uncertainty has a decisive impact on every cross section measurement. The uncertainty is determined to ±2.8% from a calibration of the luminosity scale derived from beam-separation scans as described in [96]. The luminosity is the most dominant contribution to the relative errors of the fiducial cross section in the muon channel with 2.65%. The electron channel has an uncertainty of ±2.79%, which is not the most dominant one.

Theoretical uncertainties on the cross sections

On the theoretical part of the calculation, the calculated cross sections of the MC simulated background processes suffer from uncertainties, since they are calculated to a finite order in perturbative theory. Further uncertainties are added based on the choice of the PDFs. The cross section enters the analysis by scaling the number of simulated events with a factor to the integrated luminosity of the data, given by

$$\frac{\int \mathcal{L}\,\mathrm{d}t}{(\int \mathcal{L}\,\mathrm{d}t)_{\mathrm{MC}}} = \int \mathcal{L}\,\mathrm{d}t \cdot \frac{\sigma_{\mathrm{MC}}}{N_{\mathrm{MC}}}\,, \tag{5.13}$$

where N_{MC} is the number of simulated events and σ_{MC} is the theoretical cross section of this process. To estimate the impact on the fiducial cross section, the relative errors in

Table 5.7 are used.

Table 5.7.: Theoretical uncertainties of the cross sections of the MC simulated background processes.

Process	**cross section [pb]**	**Error up**	**Error down**
W+jets	36775.4	+4.7%	−4.7% [97]
$Z \to ee$	1149.8	+4.5%	−4.0% [97]
$Z \to \mu\mu$	1150.1	+4.5%	−4.0% [97]
$Z \to \tau\tau$	1149.8	+4.5%	−4.0% [97]
single top t-channel	28.4	+3.9%	−2.2% [98]
single top s-channel	1.81	+3.9%	−3.9% [99]
single top Wt	22.3	+6.8%	−6.8% [100]
ttbar	137.3	+6.1%	−6.4% [101]
WW	29.1	+5.5%	−4.5% [97]
ZZ	1.55	+5.0%	−4.1% [97]
WZ	6.79	+7.0%	−5.5% [97]
Higgs ggF	0.55	+10.3%	−10.4% [102]
Higgs VBF	0.045	+2.6%	−2.8% [102]
Higgs WH	0.020	+2.3%	−2.3% [102]
Higgs ZH	0.011	+4.0%	−4.0% [102]

The summarized errors resulting from the cross sections lead to a relative uncertainty of $^{+1.72\%}_{-1.52\%}$. It turns out to be the most dominant contribution to the theoretical systematic uncertainty.

Efficiencies

The efficiencies of the event triggering, the reconstruction, and the identification of electrons, muons, and hadronic taus play a decisive role within this analysis. The *trigger efficiencies* are obtained by tag-and-probe studies and correction factors for the MC are derived [103]. In case of combined triggers, the two components are treated independently and the efficiencies and correction factors are multiplied to get the combined factor. The uncertainties result from varying the correction factor upwards and downwards within their uncertainties. Likewise, the efficiencies of the isolation cuts are measured by using the tag-and-probe method. The lepton *reconstruction and identification efficiency* correction factors are derived from comparisons of MC and data [103].

The trigger uncertainties belong to the significant contributions to the total uncertainty.

In the muon (electron) channel, the impact of the tau trigger uncertainty is of $^{+0.77\%}_{-0.91\%}$ ($^{+1.25\%}_{-1.43\%}$), likewise the lepton trigger adds an uncertainty of $^{+0.74\%}_{-0.81\%}$.

The identification of hadronic taus and electrons insert further relevant uncertainties of the order $\pm 1.2\%$ and $\pm 0.1\%$ in the muon channel and $\pm 3\%$ and $\pm 1.5\%$ in the electron channel (see Table 5.8). Particularly, the electron channel suffers heavily from the identification uncertainty. Additionally, the distinction of electrons and taus brings up the uncertainty 'electron faking taus'.

Tau energy scale

The *tau energy scaling* (TES) is used to infer from the measured energy of a tau to the energy on hadron level. The TES is calculated by the Tau Working Group using an in-situ correction by fitting the visible mass for $Z \to \tau\tau$ events in data and a decomposition method [104]. The uncertainties consist of four uncorrelated parts:

- The in-situ interpolation on true taus.
- The particle decomposition component of the single tau interpolation on true taus.
- Modelling of true taus.
- Contribution of fake taus.

In this analysis, these uncertainties are summed up, which results into an error of $^{+1.35\%}_{-1.59\%}$.

Electron energy scale and resolution

Analogue to the TES, the *electron energy scale* (ElES) and the *electron energy resolution* (ElEnRes) have an impact especially on the differential cross sections. It is measured with $J/\psi \to ee$ and $Z \to ee$ processes. The result suffers from different uncorrelated uncertainties. These include among others the imperfect knowledge of the material in the ECAL, uncertainties for low p_T electrons, and the calibration of the presampler [83]. This quantity is well known, such that it has not a major impact on the result.

Jet Energy scales and resolution

In general, the *jet energy scaling* (JES) is a major source of uncertainties due to theoretical uncertainties of the description of the hadronisation [105]. Indeed, this analysis relies indirectly on JES by using the missing transverse energy. It contributes only with a relative error of $^{+0.12\%}_{-0.17\%}$.

Likewise, precise knowledge of the *jet energy resolution* (JER) is a determinant key for the measurement, since it has a direct impact on the missing transverse energy. It is measured by studying the transverse momentum balance of events with jets of large p_T [106]. The uncertainty of the JER is determined by smearing every jet with a factor, which takes into account the uncertainty of the measurement. The resulting effect is symmetrized and used in this analysis [107].

Jet vertex fraction

The *jet vertex fraction* (JVF) is defined by the fraction of the tracks of a jet which can be associated to the primary vertex over the tracks associated to any vertex [108],

$$\mathrm{JVF} = \frac{\sum\limits_{\text{track of PV}} p_T}{\sum\limits_{\text{any track}} p_T} \,. \tag{5.14}$$

For jets without tracks, one sets conventionally JVF $= -1$. This quantity is used to distinguish between jets from hard scattering processes and pile-up. The consideration of this uncertainty has no influence worth mentioning on the result.

Pile-up

The disadvantage of the high luminosity of the LHC is a high rate of *pile-up* (PU) events. There are studies to understand and subtract PU contributions [109], which leave an uncertainty on its description. Here, it results in a additional systematical error of $^{+0.33\%}_{-0.38\%}$.

Table 5.8.: Relative uncertainties on the fiducial cross section (see Section 5.3.2).

Uncertainty	**muon channel**		**electron channel**	
Data	+0.37%	-0.37%	+0.61%	-0.61%
Luminosity	+2.65%	-2.63%	+2.79%	-2.79%
Cross sections	+1.72%	-1.52%	+4.56%	-4.05%
MC Statistics	+0.27%	-0.27%	+0.60%	-0.60%
QCD	+0.68%	-0.25%	+1.15%	-0.39%
Efficiency of reco. passing	+0.20%	-0.20%	+0.27%	-0.27%
Efficiency of truth passing	+0.36%	-0.36%	+0.50%	-0.50%
Correction MC Statistics	+0.95%	-0.95%	+1.28%	-1.28%
tau trigger	+0.77%	-0.91%	+1.25%	-1.43%
tau identification	+1.19%	-1.25%	+3.09%	-3.25%
electrons faking taus	-	-	+2.14%	-2.14%
lepton trigger	+0.74%	-0.81%	-	-
lepton identification	+0.10%	-0.10%	+1.45%	-1.49%
lepton isolation	+0.46%	-0.47%	+0.99%	-1.00%
JES	+0.12%	-0.17%	+0.44%	-0.40%
JER	+0.03%	-0.21%	+0.01%	-0.20%
TES	+1.35%	-1.59%	+3.66%	-3.90%
ElES	+0.01%	-0.04%	+0.71%	-0.82%
ElEnRes	+0.01%	-0.01%	+0.03%	-0.08%
MuSys	+0.05%	-0.09%	+0.01%	-0.01%
JVF	+0.01%	-0.01%	+0.01%	-0.01%
PU	+0.33%	-0.38%	+0.94%	-1.11%

5.3.2. Fiducial cross section

The fiducial cross section refers to the cross section of $Z \to \tau\tau$ events constrained on the signal region. It is calculated by

$$\sigma_{fid} = \frac{N_{obs} - N_{bkg}}{\int \mathcal{L}\,\mathrm{d}t \cdot C} \tag{5.15}$$

with the observed number of events N_{obs}, the expected number of background events N_{bkg}, the integrated luminosity $\int \mathcal{L}\,\mathrm{d}t$ and the correction factor C. In this analysis, the fiducial region is defined by the following requirements:

- $Z \to \tau_{\mathrm{lep}}\tau_{\mathrm{had}}$ decay
- $(p_T^{\ell} > 25\,\mathrm{GeV} \wedge p_T^{\tau} > 20\,\mathrm{GeV}) \vee (17\,\mathrm{GeV} < p_T^{e} < 25\,\mathrm{GeV} \wedge p_T^{\tau} > 25\,\mathrm{GeV})$
- $m_T < 50\,\mathrm{GeV}$
- $\sum \cos\Delta\phi > -0.15$
- $\Delta\phi(\ell, \tau) > \frac{\pi}{2}$

At reconstruction level E_T^{τ} always refers to the visible transverse momentum of the hadronic tau in this analysis. At truth level, it is calculated by

$$p_{T,\mathrm{visible}}^{\tau,\mathrm{truth}} = p_T^{\tau,\mathrm{truth}} - p_T^{\nu,\mathrm{truth}}. \tag{5.16}$$

For better readability, the tag *visible* and *truth* is omitted in unambiguous plots for the remainder of this chapter.

The method to trace back from a distribution on reconstruction level to the corresponding one on truth level is explained only with the p_T^{ℓ} distribution. For the p_T^{τ} distribution, the plots of the presented intermediate steps are provided in the Appendix D.

The correction

The crucial ingredient to infer from the distribution on reconstruction level to the one on truth level is the correction factor C. It corrects for detector effects and it compensates further data quality selection effects.

The correction factor for a measured observable O is based on the assumption that the background corrected data distribution given by

$$f_{\text{bkg corr. data}}(O) = f_{signal}(O) - f_{exp.bkg}(O) \tag{5.17}$$

is free of any background contribution. Hence, the correction considers only effects on a pure signal sample.

The correction has to handle fake events, detector resolution and the reconstruction efficiency. Fakes refer to mis-reconstructed $Z \to \tau\tau$ events, which do not have a corresponding event in the signal region on truth level. This effect results in a number of signal events and thus has to be compensated. The detector effects lead to migrations of events from one bin to another within the defined histograms. It results from the finite resolution of the detector and systematical shifts. The last crucial impact on the correction is the reconstruction efficiency. It describes the fraction of reconstructed and subsequently identified $Z \to \tau_{\text{lep}}\tau_{\text{had}}$ events over all signal events at truth level.

The easiest approach to get the correction of these effects is a bin-per-bin scaling using a histogram which is calculated by dividing the MC simulated signal distribution at truth level with the MC simulated distribution at reconstruction level,

$$f_{\text{truth}}(O) = f_{\text{reco}}(O) \cdot \underbrace{\frac{f_{\text{MC, truth}}(O)}{f_{\text{MC, reco}}(O)}}_{C_f(O)} . \tag{5.18}$$

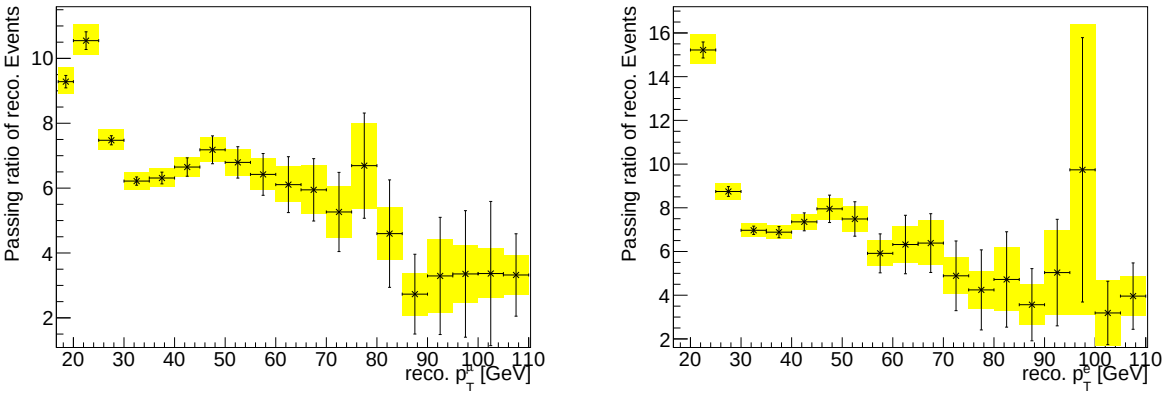

a) Muon channel a) Electron channel

Figure 5.25.: Correction histogram of p_T^{ℓ} to infer from the reconstructed distribution to the distribution on truth level. The yellow error band includes the errors of the efficiencies and the black error bars are statistical errors.

The correction of the p_T^{ℓ} distribution is shown in Figure 5.25. As mentioned before, the correction comprises several effects, such that this presentation does not allow to validate it. Therefore, the three described contributions of the correction histogram are separated

by splitting the correction into three corresponding factors, as follows

$$C_f(O) = \frac{f_{\text{reco, matched}}(O)}{f_{\text{reco}}(O)} \cdot \frac{f_{\text{truth, matched}}(O)}{f_{\text{reco, matched}}(O)} \cdot \frac{f_{\text{truth}}(O)}{f_{\text{truth, matched}}(O)} \,. \tag{5.19}$$

The correction factors are based on MC simulation. Thus, the label *MC*, used in Equation 5.18, is omitted for reasons of readability. The tag *matched* in Equation 5.19 means that the event belongs to the fiducial signal region at truth level and it passed the selection at reconstruction level, too. Hence, one assumes that the reconstructed objects of those events represent the objects on truth level, so that the kinematic differences (here p_T^ℓ) are due to the measurement errors.

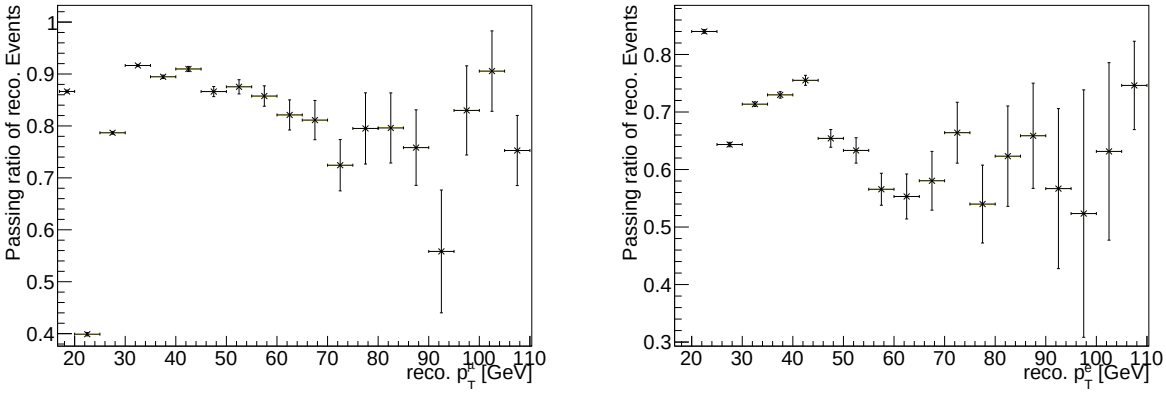

a) Muon channel a) Electron channel

Figure 5.26.: First factor of correction as appeared in Equation 5.19: Fraction of passed reconstructed events of all reconstructed events.

Figure 5.26 presents the first factor of the correction, $\frac{f_{\text{reco, matched}}(p_T^\ell)}{f_{\text{reco}}(p_T^\ell)}$, which describes the fraction of reconstructed events matching with the underlying $Z \to \tau_{\text{lep}}\tau_{\text{had}}$ truth event. As might be expected, the fraction of reconstructed events, which are correctly connected to the underlying truth event, results in a rather high value of $80 - 90\%$. The values of the first two bins are significantly smaller. This can explained by the smearing of the momentum of the lepton due to the reconstruction. Therefore, events in the border areas are mostly non-matched events. This effect is even enhanced by the initial treatment of four independent signal channels. The matching between the truth and reconstructed part of an event is given only if the truth and reconstructed events pass the same SLT or LTT channel. This treatment has an impact on the individual factors in C. Indeed, the sorting of an event as matched or non-matched event has no impact on the final correction factor, it affects only the error. Since the classification of an event as a matched one is simply

a counting experiment, the error can be estimated on basis of the Binomial distribution. The error variance is calculated by

$$\sigma^2 = \frac{\epsilon(1-\epsilon)}{N}, \tag{5.20}$$

when N denotes the number of events and the fraction of matched events is $\epsilon = \frac{N_{\text{matched}}}{N}$. In this situation, the smaller number of matched events leads to a larger error.

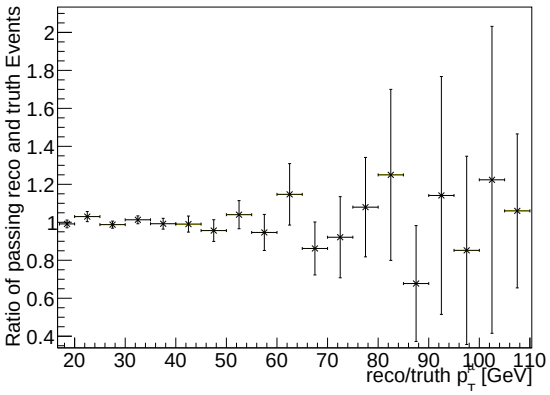

a) Muon channel

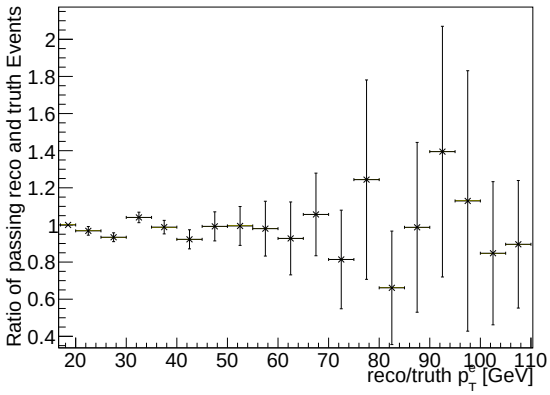

a) Electron channel

Figure 5.27.: Second factor of correction C as appeared in Equation 5.19: Unfolding of smearing effects.

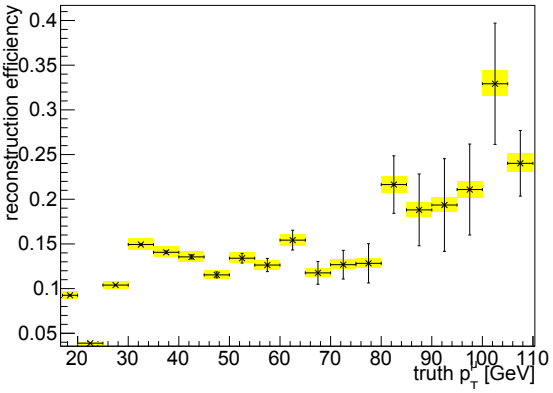

a) Muon channel

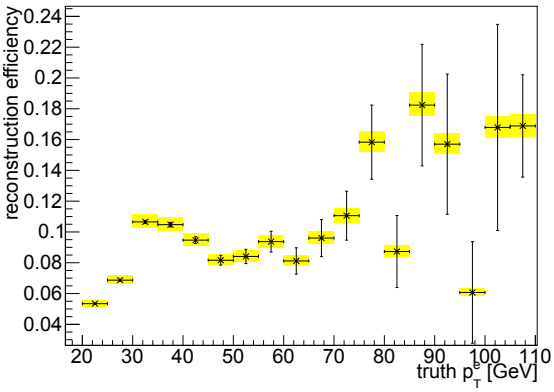

a) Electron channel

Figure 5.28.: Third (inversed) factor of correction C as appeared in Equation 5.19: the reconstruction efficiency.

The next factor of the correction in Equation 5.18 is the division of the distribution of the reconstructed p_T^{ℓ} and the distribution of the truth p_T^{ℓ} of the matched events (see

Figure 5.27). The distribution is flat at one and it supports the expectations that the reconstruction leads to the same shape of the distribution.

The last factor is the inverse reconstruction efficiency shown by Figure 5.28. It comprises several reconstruction efficiencies given by the event selection. These are the reconstruction efficiencies of the lepton and the hadronic tau, the trigger efficiencies, and further efficiencies based on the signal region. As in the first factor, the first bins are dominated by the channel dependent matching criteria. Furthermore, one sees a slightly increasing curve, as one expects for the reconstruction efficiency of muons. The error is calculated, as described for the first factor, by the formula in Equation 5.20.

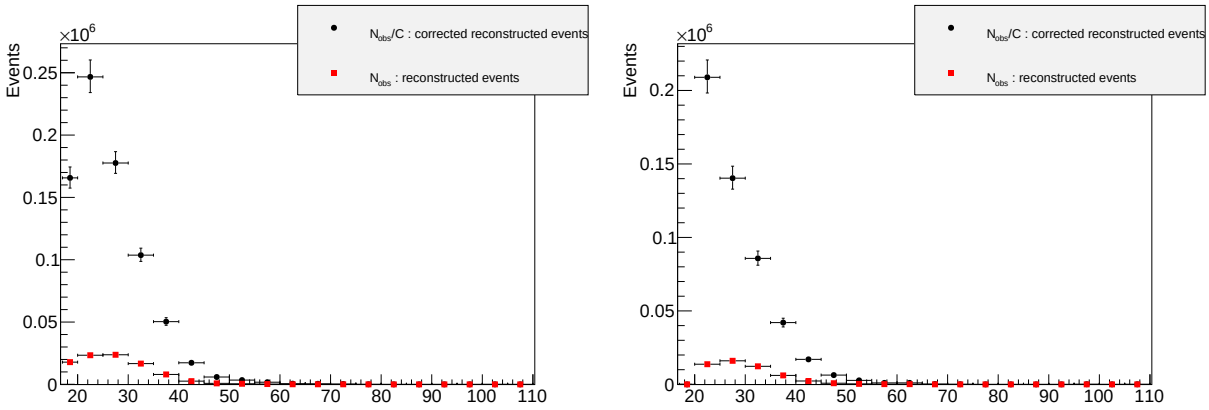

a) Muon channel a) Electron channel

Figure 5.29.: Number of reconstructed signal events and number of corrected reconstructed signal events of the lepton transverse momentum.

Summarized, all factors of the correction seem to be reasonable making the application of the correction factor valid. The final error estimation of the correction factor is the composition of the three components to respect the uncertainty of the method. The correction is used to unfold the background corrected data distribution. The uncorrected and the corrected distributions are assembled in Figure 5.29. Finally, the correction leads to an overall scaling by a factor of approximately 6 and a shape correction at the threshold of the cuts.

Differential cross section

Normalizing to the luminosity (see Equation 5.15) and dividing by the bin width of the corrected distributions, one obtains the differential fiducial cross section of the studied variable. The differential cross sections are calculated for the four presented distributions in Section 5.1.5. The results are summarized in Figures 5.30 - 5.33. Here, the yellow

error band include the systematic uncertainties which are described in Section 5.3.1. The vertical black error bars contain all statistical errors derived from the data.

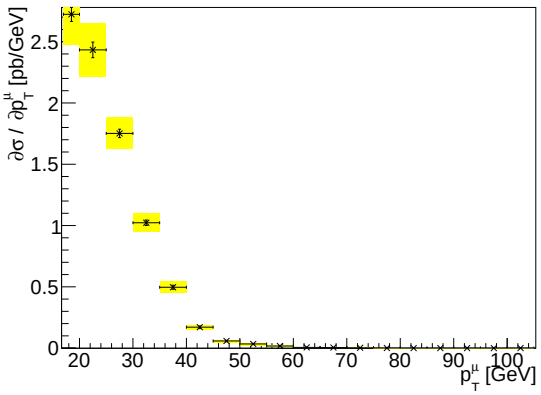

a) Muon channel

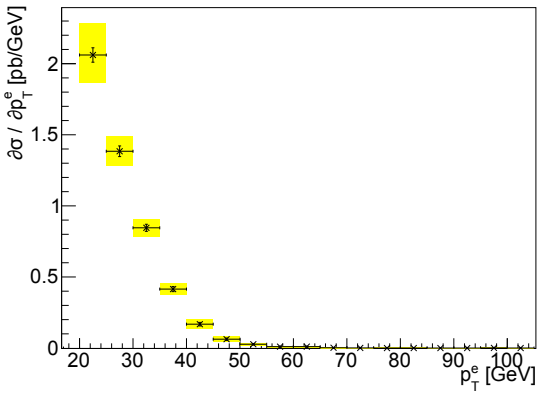

a) Electron channel

Figure 5.30.: Differential cross section as a function of the lepton transverse momentum p_T^ℓ on parton level based on the fiducial cross section calculation in Equation 5.15. The yellow error band comprised the mentioned theoretical uncertainties on the cross sections and systematical uncertainties of the template method. Additionally, it includes further systematic uncertainties described in Section 5.3.1.

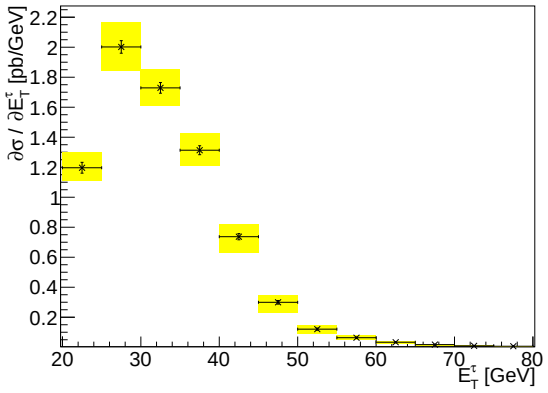

a) Muon channel

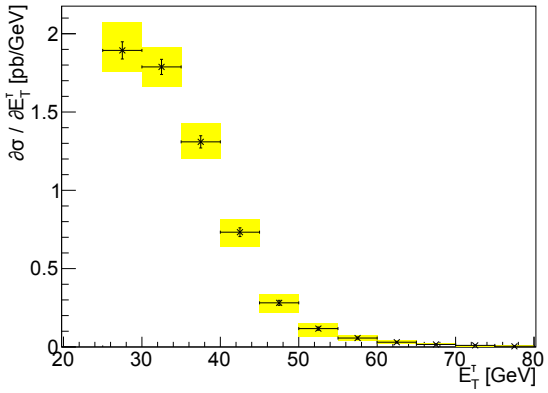

a) Electron channel

Figure 5.31.: Differential cross section as a function of the visible tau transverse momentum E_T^τ. For more information, see Figure 5.30.

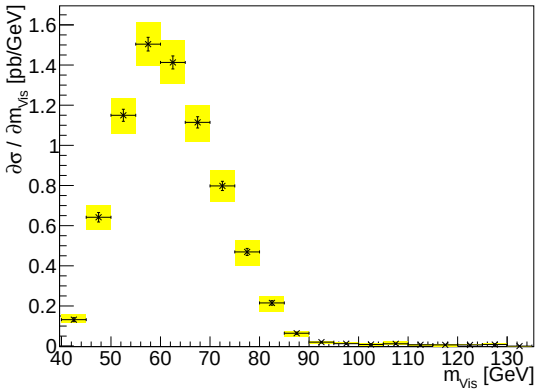

a) Muon channel

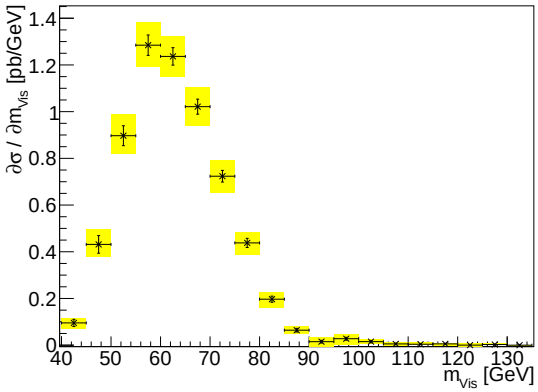

a) Electron channel

Figure 5.32.: Differential cross section as a function of the lepton-tau visible mass m_{Vis}. For more information, see Figure 5.30.

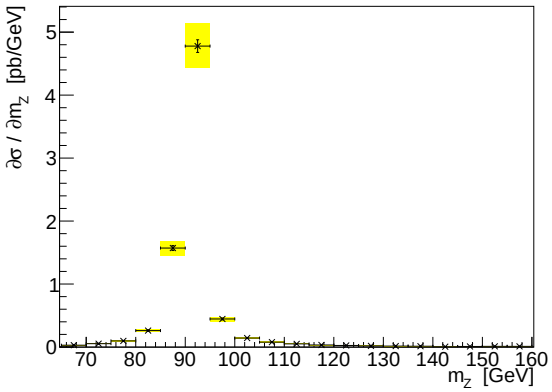

a) Muon channel

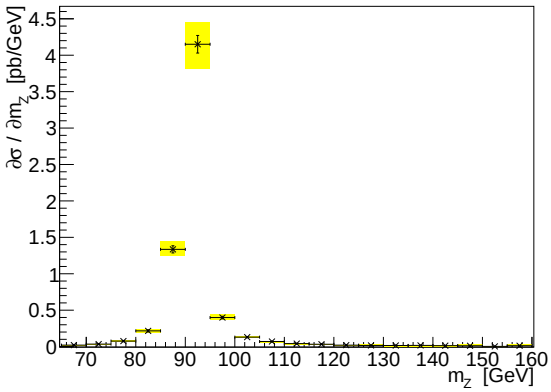

a) Electron channel

Figure 5.33.: Differential cross section as a function of the invariant Z mass m_Z. For more information, see Figure 5.30.

Fiducial cross section

The fiducial cross section can be obtained by the integration of one of the presented differential cross sections. This approach would lead to an overestimated systematical error, since these distributions contain several systematic errors coming from shape differences, which are not relevant for the fiducial cross section. To avoid extensive consideration of error correlation between the different bins, the above analysis is executed with a one-bin histogram. Therefore, the described unfolding procedure leads to a global correction factor C.

The number of expected background events, N_{bkg}, suffers from the systematic uncertainties and statistical uncertainties, too. This contribution comes from the data-driven

technique to estimate the QCD multijet background. The systematic errors on the number of expected background events N_{bkg}, the correction C, and the acceptance A consider only the statistical uncertainties of the MC simulation, the theoretical uncertainties and the mentioned systematics of the template method. Further systematic uncertainties are included in the cross sections only, since this quantity is calculated separately for every additional uncertainty and its deviations are taken into account as systematical errors.

The number of measured signal events N_{obs} subtracting the number of expected background events allows to calculate the fiducial cross section σ_{fid} with the correction C and the integrated luminosity $\int \mathcal{L}\,\mathrm{d}t$ (Equation 5.15). The calculation of the theoretical cross section replaces $N_{obs} - N_{bkg}$ in Equation 5.15 with the expected number of signal events N_{exp}, which is based on the MC simulation of the $Z \to \tau\tau$ process.

In the muon channel, the theoretical result of Equation 5.25 differs only by ~0.2% from the experimental value, whereby this result even brings up an overall uncertainty of ~4%. The theoretical expectations of the electron channel differ around 1% against a total uncertainty of ~8% of the experimental result. In both channels, the measurements are consistent with the theoretical expectations. Furthermore, given the deviations and the computed uncertainties in both channels, we assume, that the estimation of uncertainties is very conservative and the measurement could be further improved.

Muon channel

$$N_{\text{obs}} = 129541 \pm 359\,(\text{stat}) \tag{5.21}$$

$$N_{\text{bkg}} = 35389 \pm 165\,(\text{stat})\,^{+2181}_{-1124}\,(\text{syst}) \pm 770\,(\text{lumi}) \tag{5.22}$$

$$C = 0.00455 \pm 0.00036\,(\text{stat}) \tag{5.23}$$

$$\sigma_{\text{fid}} = 37.97 \pm 0.14\,(\text{stat})\,^{+1.16}_{-1.17}\,(\text{syst}) \pm 1.00\,(\text{lumi})\,\text{pb} \tag{5.24}$$

$$\sigma_{\text{fid}}^{\text{theo.}} = 37.89 \pm 0.06\,(\text{stat})\,\text{pb} \tag{5.25}$$

Electron channel

$$N_{\text{obs}} = 95204 \pm 308\,(\text{stat}) \tag{5.26}$$

$$N_{\text{bkg}} = 43229 \pm 198\,(\text{stat})\,^{+1273}_{-1031}\,(\text{syst}) \pm 758\,(\text{lumi}) \tag{5.27}$$

$$C = 0.0797 \pm 0.0037\,(\text{stat}) \tag{5.28}$$

$$\sigma_{fid} = 32.15 \pm 0.19\,(\text{stat})\,^{+2.45}_{-2.42}\,(\text{syst}) \pm 0.89\,(\text{lumi})\,\text{pb} \tag{5.29}$$

$$\sigma_{fid}^{theo.} = 31.87 \pm 0.05\,(\text{stat})\,\text{pb} \tag{5.30}$$

Total cross section

In this analysis, the total cross section refers to the inclusive $Z \to \tau\tau$ production. This includes the $Z \to \tau\tau$ decay with an invariant mass of $60\,\text{GeV} < M < 2000\,\text{GeV}$. The total cross section is calculated by scaling up the fiducial cross section with the inverse of the acceptance factor A, as follows

$$\sigma_{\text{total}} = \frac{N_{\text{obs}} - N_{\text{bkg}}}{\int \mathcal{L}\,\mathrm{d}t \cdot C \cdot A} = \frac{\sigma_{\text{fid}}}{A}\,. \tag{5.31}$$

The acceptance describes the selection efficiency from the total number of events to the fiducial signal region. It is calculated on the basis of MC simulations of the signal process. Here, the acceptance of the muon (electron) channel is $A = 0.0329^{+0.0014}_{-0.0013}$ ($0.0277^{+0.0012}_{-0.0011}$). Hence, the total cross section of the muon channel is

$$\sigma_{\text{total}} = 1151.7 \pm 4.2\,(\text{stat})\,^{+57.4}_{-50.9}\,(\text{syst}) \pm 30.4\,(\text{lumi})\,\text{pb} \tag{5.32}$$

and the result of the electron channel is

$$\sigma_{total} = 1159.79 \pm 7.1\,(\text{stat})\,^{+102.8}_{-98.9}\,(\text{syst}) \pm 32.4\,(\text{lumi})\,\text{pb}\,. \tag{5.33}$$

The theoretical total cross section based on the MC simulations including k-factors is [97]

$$\sigma^{\text{theo}}_{\text{total}} = 1150\,^{+52}_{-46}(\text{syst})\,\text{pb}\,. \tag{5.34}$$

6. Conclusion

6.1. Summary

In this thesis, a $Z \to \tau\tau$ cross section measurement of the lepton hadron channel in proton-proton collisions at $\sqrt{s} = 8\,\text{TeV}$ was presented. The results are based on the full data set of $\int \mathcal{L}\,\mathrm{d}t = 20.3\,\text{fb}^{-1}$ recorded by the ATLAS detector at the LHC.

In order to select $Z \to \tau_{\text{lep}}\tau_{\text{had}}$ events, a signal region was defined. It respects the signal event topology and includes background rejection cuts. Except from the QCD multijet contributions, all the rest of background events in the signal region was simulated with MC generators. For the QCD multijet background estimation, a data-driven template method was used. In order to validate this method of background estimation, its assumptions were studied and the choice of free parameter was cross checked with alternative cuts and control regions. At that point of the analysis, some questions remained open. The non-flat behaviour of the extrapolation factor $r_{OS/SS}$ was a cumbersome result. Furthermore, the method could be refined by relaxing the preselection of at least as 'medium' identified hadronic taus in the CommonNtuple to provide the use of larger control regions. These circumstances motivated a more conservative estimation of systematics than generally aimed for.

After validating the background estimation, the differential cross section in dependence of the lepton transverse momentum, the tau transverse momentum, the visible mass, and the invariant Z mass were calculated for the electron and muon channel, respectively. Furthermore, a fiducial cross section and the total cross section was determined to allow a comparison to the theoretical expectations. The total inclusive $Z \to \tau\tau$ cross section with the invariant Z mass in the interval of $60\,\text{GeV} < M < 2000\,\text{GeV}$ was calculated to be $1151.7 \pm 4.2\,(\text{stat})\,^{+57.4}_{-50.9}\,(\text{syst}) \pm 30.4\,(\text{lumi})\,\text{pb}$ for the muon channel and $1159.79 \pm 7.1\,(\text{stat})\,^{+102.8}_{-98.9}\,(\text{syst}) \pm 32.4\,(\text{lumi})\,\text{pb}$ for the electron channel. This measurement is in good agreement with the theoretical value of $1150\,\text{pb}\,^{+52}_{-46}(\text{syst})\,\text{pb}$.

This result is consistent with earlier studies. Both collaborations, ATLAS and CMS, have extracted the cross section of $Z \to \tau\tau$ at the center-of-mass energy of $\sqrt{s} = 7\,\text{TeV}$. CMS investigated the decay channels into the final states μ+hadrons, e+hadrons, e+μ, and μ+

μ. On the basis of an integrated luminosity of $\mathcal{L} = 36\,\text{pb}^{-1}$, they published a cross section for $\sigma(pp \to Z) \cdot B(Z \to \tau^+\tau^-)$ of $1.00 \pm 0.05\,(\text{stat.}) \pm 0.08\,(\text{syst.}) \pm 0.04(\text{lumi})\,\text{nb}$ [110]. The results for the same channels and integrated luminosity at $\sqrt{s} = 7\,\text{TeV}$ of the ATLAS collaboration are $0.97 \pm 0.07(\text{stat}) \pm 0.06(\text{syst}) \pm 0.03(\text{lumi})\,\text{nb}$ [111]. The results are consistent and they are in agreement with next-to-next-to-leading order QCD predictions.

6.2. Outlook

The next major step within the $Z \to \tau\tau$ cross section measurement is the analysis of the $\sqrt{s} = 13/14\,\text{TeV}$ data. Nevertheless, the potential of the 8 TeV data has not yet been fully exploited. The presented results are associated with sizeable systematic uncertainties, which can be reduced by further studies. One starting point could be the attempt to reduce the uncertainties coming from the QCD multijet background estimation. But its impact on the signal region is not so high. A part of the analysis that can undergo further improvement is the method chosen for the calculation of the cross sections. Since the calculation of the correction factor depends on the shape of the simulated signal sample, the implementation of e.g. a bayesian unfolding would lead to a more valid correction [112, 113].

Independent of the center-of-mass energy, $\sqrt{s}$, $Z \to \tau\tau$ studies will become very important. As an irreducible background of the most promising fermionic Higgs decay, further $Z \to \tau\tau$ studies will be a crucial field of research for prospective Standard Model measurements.

Appendix

A. MC samples

Z+jets

mc12_8TeV.147105.AlpgenPythia_Auto_P2011C_ZeeNp0.merge.NTUP_TAU.e1879_s1581_s1586_r3658_r3549_p1344/
mc12_8TeV.147106.AlpgenPythia_Auto_P2011C_ZeeNp1.merge.NTUP_TAU.e1879_s1581_s1586_r3658_r3549_p1344/
mc12_8TeV.147107.AlpgenPythia_Auto_P2011C_ZeeNp2.merge.NTUP_TAU.e1879_s1581_s1586_r3658_r3549_p1344/
mc12_8TeV.147108.AlpgenPythia_Auto_P2011C_ZeeNp3.merge.NTUP_TAU.e1879_s1581_s1586_r3658_r3549_p1344/
mc12_8TeV.147109.AlpgenPythia_Auto_P2011C_ZeeNp4.merge.NTUP_TAU.e1879_s1581_s1586_r3658_r3549_p1344/
mc12_8TeV.147110.AlpgenPythia_Auto_P2011C_ZeeNp5incl.merge.NTUP_TAU.e1879_s1581_s1586_r3658_r3549_p1344/
mc12_8TeV.147113.AlpgenPythia_Auto_P2011C_ZmumuNp0.merge.NTUP_TAU.e1880_s1581_s1586_r3658_r3549_p1344/
mc12_8TeV.147114.AlpgenPythia_Auto_P2011C_ZmumuNp1.merge.NTUP_TAU.e1880_s1581_s1586_r3658_r3549_p1344/
mc12_8TeV.147115.AlpgenPythia_Auto_P2011C_ZmumuNp2.merge.NTUP_TAU.e1880_s1581_s1586_r3658_r3549_p1344/
mc12_8TeV.147116.AlpgenPythia_Auto_P2011C_ZmumuNp3.merge.NTUP_TAU.e1880_s1581_s1586_r3658_r3549_p1344/
mc12_8TeV.147117.AlpgenPythia_Auto_P2011C_ZmumuNp4.merge.NTUP_TAU.e1880_s1581_s1586_r3658_r3549_p1344/
mc12_8TeV.147118.AlpgenPythia_Auto_P2011C_ZmumuNp5incl.merge.NTUP_TAU.e1880_s1581_s1586_r3658_r3549_p1344/
mc12_8TeV.147121.AlpgenPythia_Auto_P2011C_ZtautauNp0.merge.NTUP_TAU.e1881_s1581_s1586_r3658_r3549_p1344/
mc12_8TeV.147122.AlpgenPythia_Auto_P2011C_ZtautauNp1.merge.NTUP_TAU.e1881_s1581_s1586_r3658_r3549_p1344/
mc12_8TeV.147123.AlpgenPythia_Auto_P2011C_ZtautauNp2.merge.NTUP_TAU.e1881_s1581_s1586_r3658_r3549_p1344/
mc12_8TeV.147124.AlpgenPythia_Auto_P2011C_ZtautauNp3.merge.NTUP_TAU.e1881_s1581_s1586_r3658_r3549_p1344/
mc12_8TeV.147125.AlpgenPythia_Auto_P2011C_ZtautauNp4.merge.NTUP_TAU.e1881_s1581_s1586_r3658_r3549_p1344/
mc12_8TeV.147126.AlpgenPythia_Auto_P2011C_ZtautauNp5incl.merge.NTUP_TAU.e1881_s1581_s1586_r3658_r3549_p1344/

W+**jets**

mc12_8TeV.147025.AlpgenPythia_Auto_P2011C_WenuNp0.merge.NTUP_TAU.e1879_s1581_s1586_r3658_r3549_p1344/
mc12_8TeV.147026.AlpgenPythia_Auto_P2011C_WenuNp1.merge.NTUP_TAU.e1879_s1581_s1586_r3658_r3549_p1344/
mc12_8TeV.147027.AlpgenPythia_Auto_P2011C_WenuNp2.merge.NTUP_TAU.e1879_s1581_s1586_r3658_r3549_p1344/
mc12_8TeV.147028.AlpgenPythia_Auto_P2011C_WenuNp3.merge.NTUP_TAU.e1879_s1581_s1586_r3658_r3549_p1344/
mc12_8TeV.147029.AlpgenPythia_Auto_P2011C_WenuNp4.merge.NTUP_TAU.e1879_s1581_s1586_r3658_r3549_p1344/
mc12_8TeV.147030.AlpgenPythia_Auto_P2011C_WenuNp5incl.merge.NTUP_TAU.e1879_s1581_s1586_r3658_r3549_p1344/
mc12_8TeV.147033.AlpgenPythia_Auto_P2011C_WmunuNp0.merge.NTUP_TAU.e1880_s1581_s1586_r3658_r3549_p1344/
mc12_8TeV.147034.AlpgenPythia_Auto_P2011C_WmunuNp1.merge.NTUP_TAU.e1880_s1581_s1586_r3658_r3549_p1344/
mc12_8TeV.147035.AlpgenPythia_Auto_P2011C_WmunuNp2.merge.NTUP_TAU.e1880_s1581_s1586_r3658_r3549_p1344/
mc12_8TeV.147036.AlpgenPythia_Auto_P2011C_WmunuNp3.merge.NTUP_TAU.e1880_s1581_s1586_r3658_r3549_p1344/
mc12_8TeV.147037.AlpgenPythia_Auto_P2011C_WmunuNp4.merge.NTUP_TAU.e1880_s1581_s1586_r3658_r3549_p1344/
mc12_8TeV.147038.AlpgenPythia_Auto_P2011C_WmunuNp5incl.merge.NTUP_TAU.e1880_s1581_s1586_r3658_r3549_p1344/
mc12_8TeV.147041.AlpgenPythia_Auto_P2011C_WtaunuNp0.merge.NTUP_TAU.e1881_s1581_s1586_r3658_r3549_p1344/
mc12_8TeV.147042.AlpgenPythia_Auto_P2011C_WtaunuNp1.merge.NTUP_TAU.e1881_s1581_s1586_r3658_r3549_p1344/
mc12_8TeV.147043.AlpgenPythia_Auto_P2011C_WtaunuNp2.merge.NTUP_TAU.e1881_s1581_s1586_r3658_r3549_p1344/
mc12_8TeV.147044.AlpgenPythia_Auto_P2011C_WtaunuNp3.merge.NTUP_TAU.e1881_s1581_s1586_r3658_r3549_p1344/
mc12_8TeV.147045.AlpgenPythia_Auto_P2011C_WtaunuNp4.merge.NTUP_TAU.e1881_s1581_s1586_r3658_r3549_p1344/
mc12_8TeV.147046.AlpgenPythia_Auto_P2011C_WtaunuNp5incl.merge.NTUP_TAU.e1881_s1581_s1586_r3658_r3549_p1344/

ttbar
mc12_8TeV.117050.Powheg_ttbar.e1728_s1581_s1586_r3658_r3549_p1443/

Single top
mc12_8TeV.108343.McAtNloJimmy_AUET2CT10_SingleTopSChanWenu.merge.AOD.e1525_s1499_s1504_r3658_r3549/
mc12_8TeV.108344.McAtNloJimmy_AUET2CT10_SingleTopSChanWmunu.merge.AOD.e1525_s1499_s1504_r3658_r3549/
mc12_8TeV.108345.McAtNloJimmy_AUET2CT10_SingleTopSChanWtaunu.merge.AOD.e1525_s1499_s1504_r3658_r3549/
mc12_8TeV.108346.McAtNloJimmy_AUET2CT10_SingleTopWtChanIncl.merge.AOD.e1525_s1499_s1504_r3658_r3549/
mc12_8TeV.117360.AcerMCPythia_AUET2BCTEQ6L1_singletop_tchan_e.merge.AOD.e1346_s1499_s1504_r3658_r3549/
mc12_8TeV.117361.AcerMCPythia_AUET2BCTEQ6L1_singletop_tchan_mu.merge.AOD.e1346_s1499_s1504_r3658_r3549/
mc12_8TeV.117362.AcerMCPythia_AUET2BCTEQ6L1_singletop_tchan_tau.merge.AOD.e1346_s1499_s1504_r3658_r3549/

Higgs
mc12_8TeV.161566.PowHegPythia8_AU2CT10_ggH125_tautaulh.merge.AOD.e1217_s1469_s1470_r3542_r3549/
mc12_8TeV.161606.PowHegPythia8_AU2CT10_VBFH125_tautaulh.merge.AOD.e1217_s1469_s1470_r3542_r3549/
mc12_8TeV.161646.Pythia8_AU2CTEQ6L1_WH125_tautaulh.merge.AOD.e1217_s1469_s1470_r3542_r3549/
mc12_8TeV.161686.Pythia8_AU2CTEQ6L1_ZH125_tautaulh.merge.AOD.e1217_s1469_s1470_r3542_r3549/

Diboson
mc12_8TeV.105986.Herwig_AUET2CTEQ6L1_ZZ.merge.AOD.e1576_s1499_s1504_r3658_r3549/
mc12_8TeV.105987.Herwig_AUET2CTEQ6L1_WZ.merge.AOD.e1576_s1499_s1504_r3658_r3549/
mc12_8TeV.107100.AlpgenJimmy_AUET2CTEQ6L1_WWlnulnuNp0.merge.AOD.e1596_s1499_s1504_r3658_r3549/
mc12_8TeV.107101.AlpgenJimmy_AUET2CTEQ6L1_WWlnulnuNp1.merge.AOD.e1596_s1499_s1504_r3658_r3549/
mc12_8TeV.107102.AlpgenJimmy_AUET2CTEQ6L1_WWlnulnuNp2.merge.AOD.e1596_s1499_s1504_r3658_r3549/
mc12_8TeV.107103.AlpgenJimmy_AUET2CTEQ6L1_WWlnulnuNp3.merge.AOD.e1596_s1499_s1504_r3658_r3549/
mc12_8TeV.110829.AlpgenJimmy_AUET2CTEQ6L1_WWqqlnuNp0.merge.AOD.e1596_s1499_s1504_r3658_r3549/
mc12_8TeV.110830.AlpgenJimmy_AUET2CTEQ6L1_WWqqlnuNp1.merge.AOD.e1596_s1499_s1504_r3658_r3549/
mc12_8TeV.110831.AlpgenJimmy_AUET2CTEQ6L1_WWqqlnuNp2.merge.AOD.e1596_s1499_s1504_r3658_r3549/
mc12_8TeV.110832.AlpgenJimmy_AUET2CTEQ6L1_WWqqlnuNp3.merge.AOD.e1596_s1499_s1504_r3658_r3549/

B. Event selection

Cuts	Data	Ztautau	Zmumu	Zee	W	QCD	ttbar	Diboson	Higgs	singletop
No Cuts	176861577444	23314722	23321757	23315457	745690532	-[1]	2784409	760943	12842	1067133
CommonNtuples	3354716	275642	56645	49738	726397	-	44874	13039	1137	6810
Muon	2371558	172093	56643	14	410940	-	26801	7470	660	4087
OppositeSign	1410530	169397	30289	8	296936	-	21345	5948	649	3102
dilepVeto	1395791	169377	13820	8	296936	-	21273	5744	648	3098
Isolated lepton	414663	138080	12089	0	256134	-	15517	4946	528	2300
Tau	411421	137987	11993	0	253935	-	14965	4876	527	2226
Tau-is-muon veto	392542	133372	9637	0	243975	20890	14211	4634	498	2120
$\sum \cos \Delta\phi > -0.15$	193750	108200	3904	0	63927	15591	7899	1900	401	1036
$m_T < 50\,\text{GeV}$	141689	100364	2247	0	20557	14421	3202	788	347	411
$\Delta\phi > \frac{\pi}{2}$	129541	94555	1891	0	17608	12904	1851	568	309	258

Table B.1.: Cutflow: Absolute numbers of muon channel

Cuts	Data	Ztautau	Zmumu	Zee	W	QCD	ttbar	Dibosom	Higgs	singletop
No Cuts	176861577444	23314722	23321757	23315457	745690532	-[1]	2784409	760943	12842	1067133
CommonNtuples	3354716	275642	56645	49738	726397	-	44874	13039	1137	6810
Electron	983157	103549	2	49724	315457	-	18073	5569	477	2723
OppositeSign	617638	101384	1	29993	228199	-	15073	4398	469	2163
dilepVeto	610811	101379	1	22139	228199	-	15040	4299	468	2160
Isolated lepton	315310	75152	0	18088	184478	-	11776	3536	355	1764
Tau	312076	75083	0	17879	182639	-	11283	3475	354	1696
$\sum \cos \Delta\phi > -0.15$	153938	60643	0	11174	51238	27491	6487	1474	284	866
$m_T < 50\,\text{GeV}$	106451	55623	0	9009	15890	22213	2535	594	241	347
$\Delta\phi > \frac{\pi}{2}$	95204	51527	0	7915	13500	19461	1482	430	210	232

Table B.2.: Cutflow: Absolute numbers of electron channel

[1] The QCD background can only be made after the preselection, since the template method works with its inverting.

C. Template Method

Control regions

Table C.1.: Electron channel: Composition of the regions A, B, C, and D in case of 'lepton isolation' and 'OS' inverting.

	A	B	C	D
Lepton isolation	✓	✓	✗	✗
Opposite Sign	✓	✗	✓	✗
Data	95204	27880	140649	111082
Ztautau	51527	767	18854	422
Zmumu	0	0	0	0
Zee	7915	3377	1945	844
W	13499	4991	4113	1616
Other	2354	464	712	159
Rest	19907	18279	115024	108039

Table C.2.: Electron channel: Composition of the control regions. The signal region A and the control region B base on the standard selection. B', C', and D' work with the 'tight' tau identification.

	A	B	B'	C'	D'
BDT score	'medium'	'medium'	'tight'	not 'tight'	not 'tight'
Opposite Sign	✓	✗	✗	✓	✗
Data	95204	27880	9336	45114.9	18880.5
Ztautau	51527	767	349	16761	424
Zmumu	0	0	0	0	0
Zee	7915	3377	1043	4835	2363
W	13499	4991	1546	9036	3621
Other	2354	464	164	1210	358
Rest	19907	18279	6231	13269	12112

Extrapolation factors

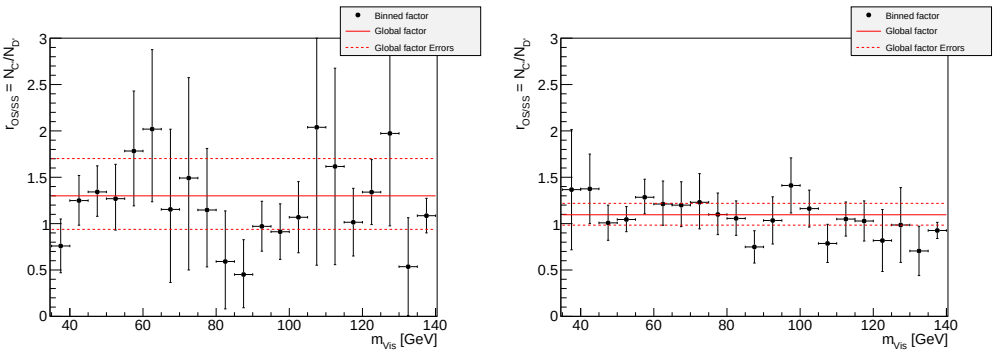

a) Muon channel b) Electron channel

Figure C.1.: The global and binned extrapolation factor $r_{\mathrm{OS/SS}}$ of the visible mass distribution of the nominal choice of control regions based on the alternative control regions of inverted tau identification 'tight'.

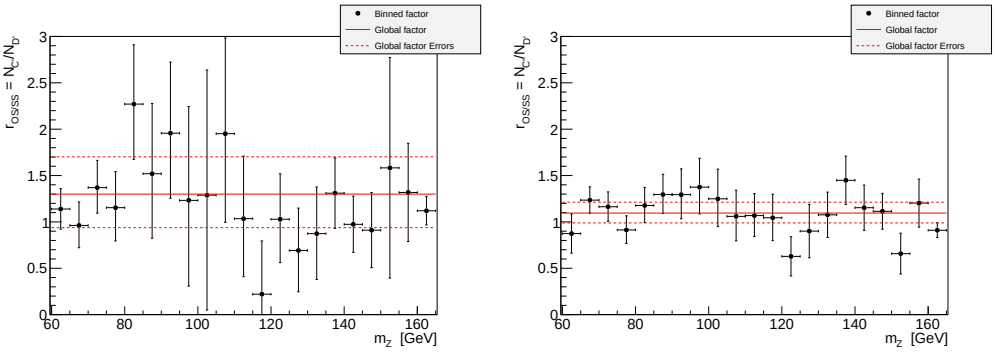

a) Muon channel b) Electron channel

Figure C.2.: The global and binned extrapolation factor $r_{\mathrm{OS/SS}}$ of the invariant Z mass distribution of the nominal choice of control regions based on the alternative control regions of inverted tau identification 'tight'.

Shape

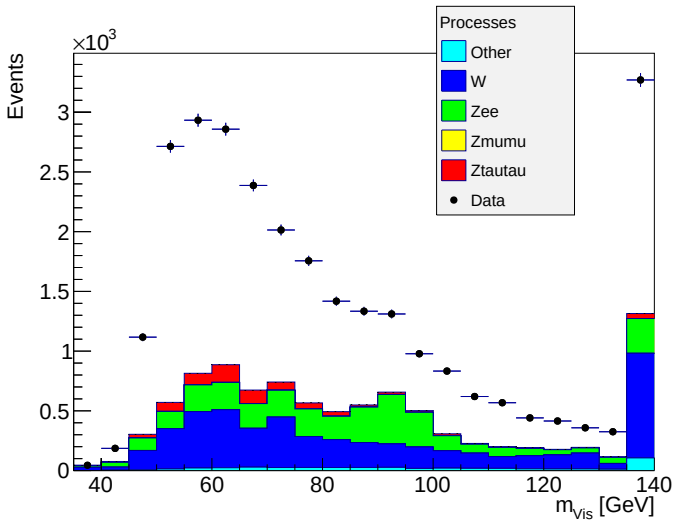

Figure C.3.: The shape of the background estimation is the subtraction of the data distribution and the distribution of the stacked MC simulations. The gap between the data and the simulations is identified as the QCD multijet background distribution of region B of the visible mass of the electron channel.

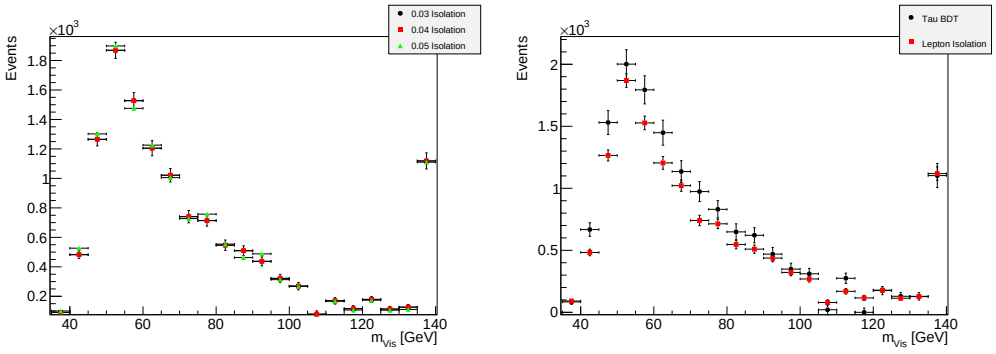

a) Extrapolated shapes based on different isolation cuts.

b) Extrapolated shapes based on the nominal isolation cut and the tau identification.

Figure C.4.: Comparison of different extrapolated visible mass distribution shapes of the electron channel. a) shows the impact on the background estimation of varying the isolation cut. b) show the difference of the cross check control regions based on the inversion of tau identification.

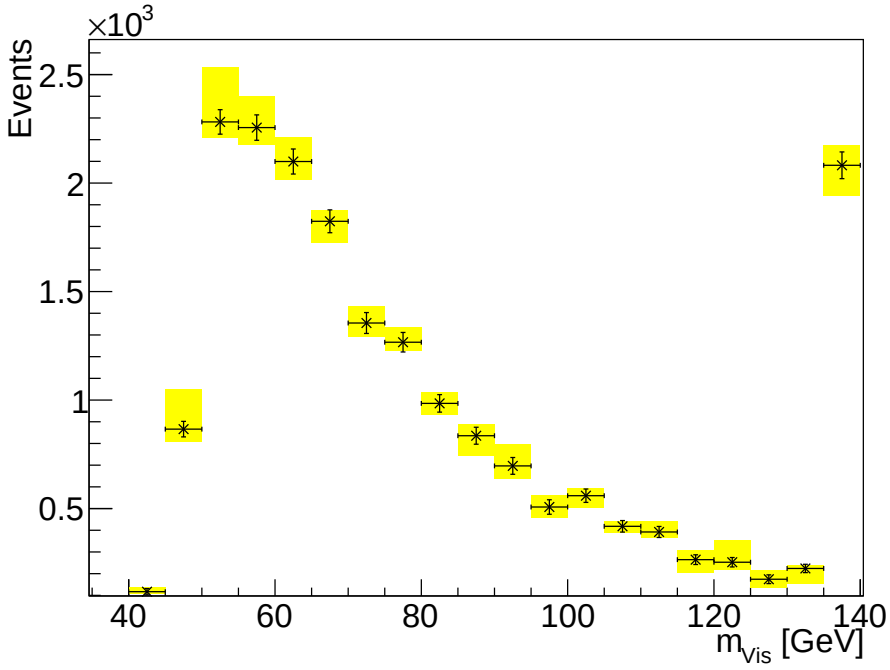

Figure C.5.: The QCD multijet background estimation for the visible mass distribution of the signal region A of the electron channel including all systematics coming from varying the isolation cut, the bin-per-bin extrapolation and the alternative control regions based on the tau identification.

D. Cross section

Correction of the tau momentum distributions

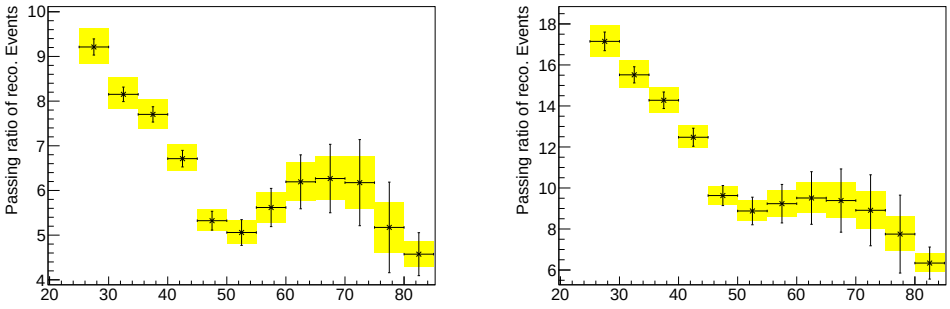

a) Muon channel a) Electron channel

Figure D.1.: Correction histogram of E_T^τ to infer from the reconstructed distribution to the distribution on truth level.

Factors of the correction

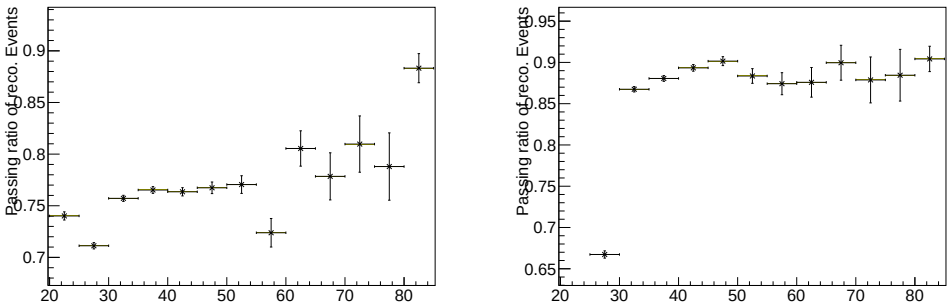

a) Muon channel a) Electron channel

Figure D.2.: First factor of correction C: Fraction of passed reconstructed events of all reconstructed events.

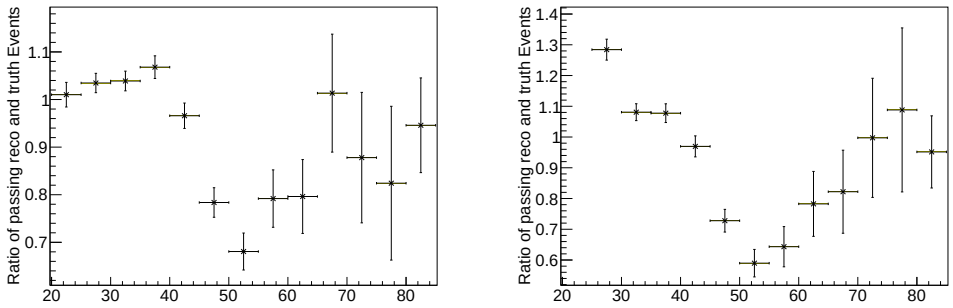

a) Muon channel a) Electron channel

Figure D.3.: Second factor of correction C: Unfolding of smearing effects.

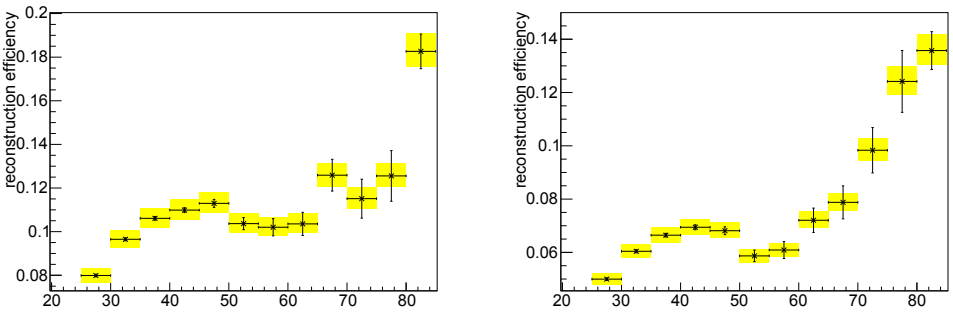

a) Muon channel a) Electron channel

Figure D.4.: Third (inversed) factor of correction C: The reconstruction efficiency.

Corrected signal

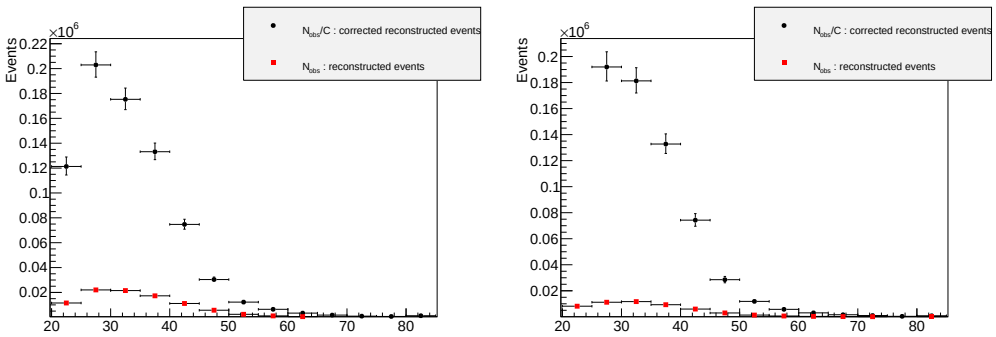

a) Muon channel a) Electron channel

Figure D.5.: Reconstructed signal events and corrected reconstructed signal events of the tau transverse momentum.

List of Figures

2.1. Fundamental particles of the Standard Model. 4
2.2. Effective propagator of a gluon. 7
2.3. The Higgs potential. 11

3.1. An overview of the LHC experiments. 15
3.2. Luminosity-weighted distribution of the mean number of interactions per crossing. 16
3.3. The peak instantaneous luminosity delivered to ATLAS per day versus time. 17
3.4. Cumulative integrated luminosity versus time. 17
3.5. Parton Distribution Functions. 19
3.6. Production cross sections with proton (anti)-proton collisions. 20
3.7. The full ATLAS detector. 21
3.8. The ATLAS Inner Detector. 22
3.9. The ATLAS calorimeter. 23
3.10. The muon detection subsystem. 24
3.11. Basic steps in simulation and data analysis. 26

4.1. Fit results of electroweak precision measurements as a function of the Higgs-boson mass. 30
4.2. Main production processes of the Higgs boson at the LHC. 31
4.3. Decay branching ratios of the Standard Model Higgs boson. 32
4.4. The measured signal strengths for a Higgs boson of mass $m_H = 125.5\,\text{GeV}$. 33
4.5. Z boson production at tree-level. 35
4.6. Next-to-leading order Feynman graphs of Z boson production. 35
4.7. Measured and calculated cross section of the Drell-Yan process. 36
4.8. The τ-decay mediated by the W boson into quarks or leptons. 37

5.1. Lepton isolation based on tracks 42
5.2. Lepton isolation based on energy cluster in the calorimeter 42

5.3. Lepton transverse momentum p_T of the muon channel: the classification into the SLT and LTT channel. These plots show the comparison of data and simulated background including QCD multijet after the preselection depicted in Figure 5.9. For more information, see Figure 5.1. 48
5.4. Lepton transverse momentum p_T of the electron channel: the classification into the SLT and LTT channel. For more information, see Figure 5.3. . . . 48
5.5. $\not{E}_T$ in case of Z and W decay. 49
5.6. Distribution of $\sum \cos \Delta\phi$. 50
5.7. Distribution of m_T. 51
5.8. Distribution of $\Delta\phi(\tau_{had}, \ell)$. 51
5.9. Cutflow of the preselection. The plot shows for every cut stage of the preselection the number of expected events given by MC simulations depicted by the coloured stacked histogram and the number of measured data events represented by the dashed line. The QCD jet background estimation can only be made after the preselection, since the template method works with inverting the isolation criteria. 54
5.10. Cutflow of the selection. The plot shows the developments of the signal composition of the selection cuts applied to predominantly reject W+jets events. For more information, see Figure 5.9. 54
5.11. Distribution of the tau transverse momentum. 56
5.12. Distribution of the lepton transverse momentum. 56
5.13. Distribution of the visible mass. 57
5.14. Distribution of the invariant Z mass. 57
5.15. The signal and control regions of the ABCD method. 58
5.16. The global and binned extrapolation factor of the tau and lepton momentum distribution of the muon channel. 62
5.17. The global and binned extrapolation factor of the tau and lepton momentum distribution based on the alternative control regions of the muon channel. 62
5.18. The global and binned extrapolation factor of the tau and lepton momentum distribution of the electron channel. 63
5.19. The global and binned extrapolation factor of the tau and lepton momentum distribution based on the alternative control regions of the electron channel. 63
5.20. The global and binned extrapolation factor of the visible mass distribution. 64
5.21. The global and binned extrapolation factor of the invariant Z mass distribution. 64

5.22. Region B of the template method: Stacked background in comparison to the data of the muon channel. 65
5.23. Comparison of different extrapolated shapes of the muon channel. 66
5.24. The QCD multijet background estimation for the signal region of the muon channel. 67
5.25. Correction of the lepton momentum distribution. 75
5.26. First factor of correction as appeared in Equation 5.19: Fraction of passed reconstructed events of all reconstructed events. 76
5.27. Second factor of correction C as appeared in Equation 5.19: Unfolding of smearing effects. 77
5.28. Reconstruction efficiency of the lepton transverse momentum. 77
5.29. Comparison of reconstructed and corrected signal of the lepton transverse momentum. 78
5.30. Differential cross section of the lepton transverse momentum. 79
5.31. Differential cross section of the tau transverse momentum. 79
5.32. Differential cross section of the visible mass. 80
5.33. Differential cross section of the invariant Z mass. 80

C.1. The global and binned extrapolation factor of the visible mass distribution based on the alternative control regions. 92
C.2. The global and binned extrapolation factor of the invariant Z mass distribution based on the alternative control regions. 92
C.3. Region B of the template method: Stacked background in comparison to the data of the electron channel. 93
C.4. Comparison of different extrapolated shapes of the electron channel. 93
C.5. The QCD multijet background estimation for the signal region of the electron channel. 94

D.1. Correction of the tau momentum distribution. 95
D.2. First factor of correction C: Fraction of passed reconstructed events of all reconstructed events. 95
D.3. Second factor of correction C: Unfolding of smearing effects. 96
D.4. Reconstruction efficiency of the tau transverse momentum. 96
D.5. Comparison of reconstructed and corrected signal of the tau transverse momentum. 96

List of Tables

2.1. Quantum numbers of the matter-particles. 9

4.1. Higgs production cross sections. 31
4.2. Branching ratios of Z boson decay. 36
4.3. Branching ratios of dominant τ decay channels 38

5.1. Kinematic definition of SLT and CTT channel 47
5.2. Cutflow of the muon channel: signal efficiencies and background rejection. 53
5.3. Cutflow of the electron channel: signal efficiencies and background rejection. 53
5.4. Composition of the regions A, B, C, and D of the muon channel in case of 'lepton isolation' and 'OS/SS' inversion. 60
5.5. Composition of the control regions of the muon channel. The signal region A and the control region B are based on the standard selection. B', C', and D' relay on the 'tight' tau identification. 61
5.6. Systematic uncertainties of the template method. 68
5.7. Theoretical uncertainties of the cross sections. 70
5.8. Systematics of the fiducial cross section 73

B.1. Cutflow: Absolute numbers of muon channel 89
B.2. Cutflow: Absolute numbers of electron channel 89

C.1. Electron channel: Composition of the regions A, B, C, and D in case of 'lepton isolation' and 'OS' inverting. 91
C.2. Electron channel: Composition of the control regions. The signal region A and the control region B base on the standard selection. B', C', and D' work with the 'tight' tau identification. 91

Bibliography

[1] G. Aad, et al. (The ATLAS Collaboration), *Observation of a new particle in the search for the Standard Model Higgs boson with the ATLAS detector at the LHC*, Phys. Lett. B **716**, 1 (2012)

[2] S. Chatrchyan, et al. (The CMS Collaboration), *Observation of a new boson at a mass of 125 GeV with the CMS experiment at the LHC*, Phys. Lett. B **716**, 30 (2012)

[3] G. Aad, et al. (The ATLAS Collaboration), *Evidence for the Higgs-boson Yukawa coupling to tau leptons with the ATLAS detector* (2015)

[4] S. Chatrchyan, et al. (The CMS Collaboration), *Evidence for the 125 GeV Higgs boson decaying to a pair of τ leptons* (2014), `arXiv:1401.5041[hep-ex]`

[5] G. Aad, et al. (The ATLAS Collaboration), *Evidence for the spin-0 nature of the Higgs boson using ATLAS data*, Phys. Lett. B **726(1-3)**, 120 (2013)

[6] S. Chatrchyan, et al. (The CMS Collaboration), *Study of the Mass and Spin-Parity of the Higgs Boson Candidate via Its Decays to Z Boson Pairs*, Phys. Rev. Lett. **110**, 081803 (2013)

[7] *Search for flavor-changing neutral currents in $t \to cH$, with $H \to \gamma\gamma$, and limit on the tcH coupling*, Technical Report ATLAS-CONF-2013-081, CERN, Geneva (2013)

[8] *Search for ttH production in the $H \to yy$ channel at $\sqrt{s} = 8\,\text{TeV}$ with the ATLAS detector*, Technical Report ATLAS-CONF-2013-080, CERN, Geneva (2013)

[9] *Search for the bb decay of the Standard Model Higgs boson in associated W/ZH production with the ATLAS detector*, Technical Report ATLAS-CONF-2013-079, CERN, Geneva (2013)

[10] *Search for associated production of the Higgs boson in the $WH \to WWW^* \to l\nu l\nu l\nu$ and $ZH \to lll\nu l\nu$ channels with the ATLAS detector at the LHC*, Technical Report ATLAS-CONF-2013-075, CERN, Geneva (2013)

[11] *Differential cross sections of the Higgs boson measured in the diphoton decay channel using 8 TeV pp collisions*, Technical Report ATLAS-CONF-2013-072, CERN, Geneva (2013)

[12] *Search for a high-mass Higgs boson in the $H \to WW \to l\nu l\nu$ decay channel with the ATLAS detector using 21 fb^{-1} of proton-proton collision data*, Technical Report ATLAS-CONF-2013-067, CERN, Geneva (2013)

[13] *Search for charged Higgs bosons in the τ+jets final state with pp collision data recorded at $\sqrt{s} = 8$ TeV with the ATLAS experiment*, Technical Report ATLAS-CONF-2013-090, CERN, Geneva (2013)

[14] J. L. Feng, *Dark Matter Candidates from Particle Physics and Methods of Detection*, Ann. Rev. Astron. Ap. **48(1)**, 495 (2010)

[15] D. Griffiths, *Introduction to Elementary Particles*, Wiley-VCH, 2nd edition edition (2008)

[16] Y. Fukuda, et al. (The Super-Kamiokande Collaboration), *Evidence for Oscillation of Atmospheric Neutrinos*, Phys. Rev. Lett. **81**, 1562 (1998)

[17] F. An, et al. (The DAYA-BAY Collaboration), *Observation of electron-antineutrino disappearance at Daya Bay*, Phys. Rev. Lett. **108**, 171803 (2012)

[18] N. Agafonova, et al., *Observation of a first candidate event in the OPERA experiment in the CNGS beam*, Phys. Lett. B **691(3)**, 138 (2010)

[19] J. Beringer, et al. (The Particle Data Group), *Neutrino Mass, Mixing and oscillations*, Phys. Rev. D **86** (2012)

[20] *Standard model of elementary particles* `http://en.wikipedia.org/wiki/File:Standard_Model_of_Elementary_Particles.svg`

[21] E. Noether, *Invariante Variationsprobleme*, Nachr. v. d. Ges. d. Wiss. zu Göttingen pages 235–257 (1918)

[22] D. H. Perkins, *Introduction to High Energy Physics*, Cambridge University Press, 4th edition edition (2000)

[23] J. Beringer, et al. (The Particle Data Group), *Quantum chromodynamics*, Phys. Rev. D **86** (2012)

[24] J. D. Bjorken, E. A. Passos, *Inelastic Electron-Proton and γ-Proton Scattering and the Structure of the Nucleon*, Phys. Rev. Lett. **185.5** (1969)

[25] E. D. Bloom, et al., *High-Energy Inelastic e p Scattering at 6-Degrees and 10-Degrees*, Phys. Rev. Lett. **23**, 930 (1969)

[26] H. Becquerel, *Sur les Radiations Invisibles Emises par les Corps Phosphorescents*, Compt. Ren. **122**, 501 (1896)

[27] H. Becquerel, *Sur les Proprietes Differentes de Radiations Invisibles Emises par les Sels d'Uranium, et du Rayonnement de la Paroi Anticathodique d'un Tube de Crookes*, Compt. Ren. **122**, 762 (1896)

[28] F. L. Wilson, *Fermi's Theory of Beta-Decay*, Am. J. Phys. **36(12)** (1968)

[29] E. Fermi, *Versuch einer Theorie der Betastrahlen*, Z. Phys. **88** (1934)

[30] P. Langacker, *The Standard Model and Beyond*, Taylor and Francis Group, Boca Raton (2010)

[31] S. L. Glashow, *Partial-symmetries of weak interactions*, Nucl. Phys. **22**, 579 (1961)

[32] S. Weinberg, *A Model of Leptons*, Phys. Rev. Lett. **19**, 1264 (1967)

[33] A. Salam, *Elementary Particle Theory*, N. Svartholm, Stockholm (1968)

[34] P. W. Higgs, *Broken symmetries, massless particles and gauge fields*, Phys. Lett. **12(2)**, 132 (1964)

[35] P. W. Higgs, *Broken Symmetries and the Masses of Gauge Bosons*, Phys. Rev. Lett. **13**, 508 (1964)

[36] F. Englert, R. Brout, *Broken Symmetry and the Mass of Gauge Vector Mesons*, Phys. Rev. Lett. **13**, 321 (1964)

[37] L. Alvarez-Gaume, J. Ellis, *Eyes on a prize particle*, Nat. Phys. **7**, 2 (2011)

[38] G. Arnison, et al. (The UA1 Collaboration), *Experimental observation of lepton pairs of invariant mass around* 95 GeV/c^2 *at the CERN SPS collider*, Phys. Lett. B **126(5)**, 398 (1983)

[39] J. Beringer, et al. (The Particle Data Group), *Particle Listings*, Phys. Rev. D **86** (2012)

[40] L. Evans, P. Bryant, *LHC Machine*, J. Instrum. **3**, S08001

[41] *The four main LHC experiments* (1999), `https://cds.cern.ch/record/40525`

[42] *LEP design report*, CERN, Geneva (1984)

[43] D. d'Enterria, *Physics at the LHC: a short overview*, JPCS **270** (2011)

[44] S. Chatrchyan, et al. (The CMS Collaboration), *The CMS experiment at the CERN LHC*, J. Instrum. **3**, S08004

[45] K. Aamodt, et al. (The ALICE Collaboration), *The ALICE experiment at the CERN LHC*, J. Instrum. **3**, S08002

[46] A. Alves, et al. (The LHCb Collaboration), *The LHCb Detector at the LHC*, J. Instrum. **3**, S08005

[47] G. Aad, et al. (The ATLAS Collaboration), *The ATLAS Experiment at the CERN Large Hadron Collider*, J. Instrum. **3**, S08003

[48] M. Bajko, et al., *Report of the task force on the incident of 19 september 2008 at the LHC*, LHC-PROJECT-REPORT-1168 (2009)

[49] `https://twiki.cern.ch/twiki/bin/view/AtlasPublic/LuminosityPublicResults`

[50] A. D. Martin, W. J. Stirling, G. W. R. S. Thorne, *Parton distributions for the LHC*, Eur. Phys. J. C **63**, 189 (2009)

[51] *ATLAS detector and physics performance: Technical Design Report, 1* (1999)

[52] *ATLAS detector and physics performance: Technical Design Report, 2* (1999)

[53] G. Aad, et al. (The ATLAS Collaboration), *The ATLAS Experiment at the CERN Large Hadron Collider*, J. Instrum. **3(8)** (2008)

[54] A. Binguel, *The ATLAS TRT and its Performance at LHC*, JPCS **347(1)**, 012025 (2012)

[55] *ATLAS trigger and data acquisition posters* `http://atlas.web.cern.ch/Atlas/documentation/poster/HTML/triggerdaq.html`

[56] P. Jenni, et al. (The ATLAS Collaboration), *ATLAS high-level trigger, data-acquisition and controls*, Technical Design Report (2003)

[57] R. Brun, F. Carminati, S. Giani, *GEANT Detector Description and Simulation Tool* (1994)

[58] M. L. Mangano, M. Moretti, F. Piccinini, R. Pittau, A. D. Polosa, *ALPGEN, a generator for hard multiparton processes in hadronic collisions*, J. High Energ. Phys. **0307** (2003)

[59] T. Sjostrand, S. Mrenna, P. Z. Skands, *PYTHIA 6.4 Physics and Manual*, J. High Energ. Phys. **0605**, 026 (2006)

[60] A. Buckley, J. Butterworth, S. Gieseke, D. Grellscheid, S. Hoche, et al., *General-purpose event generators for LHC physics*, Phys. Rept. **504**, 145 (2011)

[61] J. A. Bagger, et al. (The ALEPH Collaboration and The DELPHI Collaboration and The L3 Collaboration and The OPAL Collaborationand The SLD Collaboration and The LEP Electroweak Working Group and The SLD Electroweak and Heavy Flavour Groups), *Precision electroweak measurements on the Z resonance*, Phys. Rept. **427(5-6)**, 257 (2006)

[62] B. Lee, C. Quigg, H. Thacker, *Weak Interactions at Very High-Energies: The Role of the Higgs Boson Mass*, Phys. Rev. D **16**, 1519 (1977)

[63] D. Dicus, V. Mathur, *Upper bounds on the values of masses in unified gauge theories*, Phys. Rev. D **7**, 3111 (1973)

[64] S. Cortese, E. Pallante, R. Petronzio, *Higgs mass dependence of electroweak radiative corrections and the triviality bound*, Phys. Lett. B **301(2-3)**, 203 (1993)

[65] G. Bernardi, et al. (The Tevatron New Phenomena Higgs Working Group and CDF and D0 Collaboration), *Combined CDF and D0 Upper Limits on Standard Model Higgs Boson Production at High Mass* ($155-200\ GeV/c^2$) *with 3* fb^{-1} *of data* (2008), `arXiv:0808.0534[hep-ex]`

[66] P. Langacker, J. Erler, *Electroweak model and constraints on new physics*, Eur. Phys. J. C **15(1-4)**, 95 (2000)

[67] *Search for the Standard Model Higgs boson at LEP*, Phys. Lett. B **565**, 61 (2003)

[68] J. Beringer, et al. (The Particle Data Group), *Status of higgs boson physics*, Phys. Rev. D **86** (2012)

[69] S. Dittmaier, et al. (LHC Higgs Cross Section Working Group), *Handbook of LHC Higgs Cross Sections: 2. Differential Distributions*, Technical Report CERN-2012-002, Geneva (2012)

[70] G. Cacciapaglia, A. Deandrea, J. Llodra-Perez, $H \to \gamma\gamma$ *beyond the Standard Model*, J. High Energ. Phys. **(06)**, 054 (2009)

[71] S. Dittmaier, et al. (The LHC Higgs Cross Section Working Group), *Handbook of LHC Higgs Cross Sections: 1. Inclusive Observables* (2011), `arXiv:1101.0593[hep-ph]`

[72] *Updated coupling measurements of the Higgs boson with the ATLAS detector using up to 25 fb*$^{-1}$ *of proton-proton collision data*, Technical Report ATLAS-CONF-2014-009, CERN, Geneva (2014)

[73] F. J. Hasert, et al. (The Gargamelle Neutrino Collaboration), *Observation of Neutrino Like Interactions Without Muon Or Electron in the Gargamelle Neutrino Experiment*, Phys. Lett. B **46**, 138 (1973)

[74] G. Aad, et al. (The ATLAS Collaboration), *Measurement of the inclusive* $W^{\pm}$ *and Z/gamma cross sections in the electron and muon decay channels in pp collisions at* $\sqrt{s} = 7$ *TeV with the ATLAS detector*, Phys. Rev. **D85**, 072004 (2012)

[75] K. Nakamura, et al. (The Particle Data Group), τ *branching fractions*, J. Phys. G **37**, 075021 (2010)

[76] M. L. Perl, et al., *Evidence for Anomalous Lepton Production in* e^+e^- *Annihilation*, Phys. Rev. Lett. **35**, 1489 (1975)

[77] M. L. Pearl, *The discovery of the tau lepton*, SLAC-PUB-5937, C92-06-24 (1992)

[78] G. F. et al., *Inclusive Anomalous Muon Procution in* e^+e^- *Annihilation*, Phys. Rev. Lett. **38**, 1313 (1977)

[79] J. Burmester, et al. (The PLUTO Collaboration), *Anomalous muon production in* e^+e^- *annihilations as evidence for heavy leptons*, Phys. Lett. B **68(3)**, 297 (1977)

[80] A. Barbaro-Galtieri, et al., *Electron-Muon and Electron-Hadron Production in* e^+e^- *Collisions*, Phys. Rev. Lett. **39(17)**, 1058 (1977)

[81] G. Aad, et al. (The ATLAS Collaboration), *Commissioning of the ATLAS Muon Spectrometer with cosmic rays*, Eur. Phys. J. C **70(3)**, 875 (2010)

[82] G. Aad, et al. (The ATLAS Collaboration), *Measurement of the $W \to \ell\nu$ and $Z/\gamma^* \to \ell\ell$ production cross sections in proton-proton collisions at $\sqrt{s} = 7$ TeV with the ATLAS detector*, J. High Energ. Phys. **60** (2010)

[83] G. Aad, et al. (The ATLAS Collaboration), *Electron performance measurements with the ATLAS detector using the 2010 LHC proton-proton collision data*, Eur. Phys. J. C **72**, 1909 (2012)

[84] M. Cacciari, G. P. Salam, G. Soyez, *The anti-k_t jet clustering algorithm*, J. High Energ. Phys. **(04)**, 063 (2008)

[85] *Performance of the Reconstruction and Identification of Hadronic Tau Decays with ATLAS*, Technical Report ATLAS-CONF-2011-152, CERN, Geneva (2011)

[86] G. Aad, et al. (The ATLAS Collaboration), *Measurement of inclusive jet and dijet cross sections in proton-proton collisions at 7 TeV centre-of-mass energy with the ATLAS detector*, Eur. Phys. J. C **51**, 1512 (2011)

[87] *Combination of ATLAS and CMS top-quark pair cross-section measurements using proton-proton collisions at $\sqrt{s} = 8$ TeV*, Technical Report ATLAS-CONF-2014-054, CERN, Geneva (2014)

[88] *Combination of cross-section measurements for associated production of a single top-quark and a W boson at $\sqrt{s} = 8$ TeV with the ATLAS and CMS experiments*, Technical Report ATLAS-CONF-2014-052, CERN, Geneva (2014)

[89] *Inclusive W/Z cross section at 8 TeV*, Technical Report CMS-PAS-SMP-12-011, CERN, Geneva (2012)

[90] *Measurement of the W^+W^- production cross section in proton-proton collisions at $\sqrt{s} = 8$ TeV with the ATLAS detector*, Technical Report ATLAS-CONF-2014-033, CERN, Geneva (2014)

[91] *Measurement of the total ZZ production cross section in proton-proton collisions at $\sqrt{s} = 8$ TeV in $20\,fb^{-1}$ with the ATLAS detector*, Technical Report ATLAS-CONF-2013-020, CERN, Geneva (2013)

[92] A. Datta, B. Mukhopadhyaya, A. Raychaudhuri, *Physics at the Large Hadron Collider*, Springer, Heidelberg (2011)

[93] D. Evangelakou, *$Z \to \tau_h\tau_l$ Cross Section Measurement and $\tau\tau$ Mass Reconstruction with the ATLAS Detector at the LHC*, Ph.D. thesis, Georg-August-Universität Göttingen, Göttingen (2012)

[94] B. Abbott, et al. (The D0 Collaboration), *Measurement of the W boson mass*, Phys. Rev. D **58**, 092003 (1998)

[95] A. Elagin, P. Murat, A. Pranko, A. Safonov, *A New Mass Reconstruction Technique for Resonances Decaying to di-tau*, Nucl. Instrum. Meth. A **654**, 481 (2011)

[96] G. Aad, et al. (The ATLAS Collaboration), *Improved luminosity determination in pp collisions at $\sqrt{s}$ = 7 TeV using the ATLAS detector at the LHC*, Eur. Phys. J. C **73**, 2518 (2013)

[97] J. Butterworth, et al., *Single Boson and Diboson Production Cross Sections in pp Collisions at $\sqrt{s}$ = 7 TeV*, ATL-COM-PHYS-2010-695 (2010)

[98] N. Kidonakis, *Next-to-next-to-leading-order collinear and soft gluon corrections for t-channel single top quark production*, Phys. Rev. D **83** (2011)

[99] N. Kidonakis, *Next-to-next-to-leading logarithm resummation for s-channel single top quark production*, Phys. Rev. D **81** (2010)

[100] N. Kidonakis, *Two-loop soft anomalous dimensions for single top quark associated production with a W^- or H^-*, Phys. Rev. D **82** (2010)

[101] M. Cacciari, M. Czakon, M. Mangano, A. Mitov, P. Nason, *Top-pair production at hadron colliders with next-to-next-to-leading logarithmic soft-gluon resummation*, Physics Letters B **710(4-5)**, 612 (2012)

[102] S. Dittmaier, et al. (The LHC Higgs Cross Section Working Group), *Handbook of LHC Higgs Cross Sections: 1. Inclusive Observables*, CERN, Geneva (2011)

[103] G. Aad, et al. (The ATLAS Collaboration), *Electron reconstruction and identification efficiency measurements with the ATLAS detector using the 2011 LHC proton-proton collision data*, Eur. Phys. J. C **74**, 2941 (2014), 1404.2240

[104] *Determination of the tau energy scale and the associated systematic uncertainty in proton-proton collisions at $\sqrt{s}$ = 8 TeV with the ATLAS detector at the LHC in 2012*, Technical Report ATLAS-CONF-2013-044, CERN, Geneva (2013)

[105] T. Barillari (on behalf of the ATLAS Collaboration), *Jet Energy Scale Uncertainties in ATLAS*, Journal of Physics: Conference Series **404(1)**, 012012 (2012), URL `http://stacks.iop.org/1742-6596/404/i=1/a=012012`

[106] G. Aad, et al. (The ATLAS Collaboration), *Jet energy resolution in proton-proton collisions at* $\sqrt{s} = 7$ *TeV recorded in 2010 with the ATLAS detector*, The European Physical Journal C **73(3)**, 2306 (2013)

[107] D. Alvarez Piqueras, et al., *Measurement of the Higgs boson couplings in the* $\tau\tau$ *final state with the ATLAS detector - Supporting Note*, Technical Report ATL-COM-PHYS-2014-170, CERN, Geneva (2014)

[108] D. W. Miller, A. Schwartzman, D. Su, *Jet-Vertex Association Algorithm*, Technical Report ATL-COM-PHYS-2008-008, CERN, Geneva (2008)

[109] *Pile-up subtraction and suppression for jets in ATLAS*, Technical Report ATLAS-CONF-2013-083, CERN, Geneva (2013)

[110] S. Chatrchyan, et al. (The CMS Collaboration), *Measurement of the Inclusive Z Cross Section via Decays to Tau Pairs in pp Collisions at* $\sqrt{s} = 7$ *TeV*, J. High Energ. Phys. **1108**, 117 (2011)

[111] *Observation of* $Z \to \tau_h\tau_l$ *Decays with the ATLAS detector*, Technical Report ATLAS-CONF-2011-010, CERN, Geneva (2011)

[112] G. Aad, et al. (The ATLAS Collaboration), *Measurement of dijet cross sections in pp collisions at 7 TeV centre-of-mass energy using the ATLAS detector*, J. High Energ. Phys. **1405**, 059 (2014)

[113] A. Höcker, V. Kartvelishvili, *SVD approach to data unfolding*, Nucl. Instr. Meth. Phys. Res. A **372(3)**, 469 (1996)

Acknowledgements

First and foremost I would like to thank my supervisor Prof. Dr. Arnulf Quadt. Thank you for giving me the opportunity to write this master thesis in the group. Furthermore, I would like to express my gratitude for giving me the possibility to enter the scientific world. I gained much enriching experience in the foregoing internship in Paris and in the master thesis in Göttingen. I also want to thank Prof. Dr. Ariane Frey for her willing to be the second referee.

Moreover, I'm thankful for the help of Zinonas Zinonos and Ulla Blumenschein. Beside the physics, we had a really nice atmosphere in our office. Many thanks for the tea and the discussions. $\epsilon\upsilon\chi\alpha\rho\iota\sigma\tau\omega \quad \pi o\lambda\upsilon$! Et merci beaucoup à Eric Drechsler pour les bons conseils autour du master.

The master thesis has been corrected at different stages from different people with different foci. Thanks for that to Tobias Bisanz, Eva Hill, Mehran Seyed Hosseini, Paul Kirchgessner, and Nils Schulte.

Die mir entgegengebrachte Hilfe begrenzt sich jedoch nicht allein auf das Fachliche. Anhand der Arbeit nicht direkt ersichtlich, aber umso bedeutender für mich war und ist die mentale Unterstützung meiner Eltern, meiner Geschwister Nils, Svenja und Jonas sowie meiner Freundin Katharina. Vielen Dank an Euch.

Erklärung nach §18(8) der Prüfungsordnung für den Bachelor-Studiengang Physik und den Master-Studiengang Physik an der Universität Göttingen:

Hiermit erkläre ich, dass ich diese Abschlussarbeit selbständig verfasst habe, keine anderen als die angegebenen Quellen und Hilfsmittel benutzt habe und alle Stellen, die wörtlich oder sinngemäß aus veröffentlichten Schriften entnommen wurden, als solche kenntlich gemacht habe.
Darüberhinaus erkläre ich, dass diese Abschlussarbeit nicht, auch nicht auszugsweise, im Rahmen einer nichtbestandenen Prüfung an dieser oder einer anderen Hochschule eingereicht wurde.

Göttingen, den August 27, 2015

(Simon Schulte)